MEASUREMENTS OF FEL DYNAMICS

Allan M. MacLeod

A thesis submitted in partial fulfilment of
the requirements of the University of
Abertay Dundee for the degree of
Doctor of Philosophy

February 1999

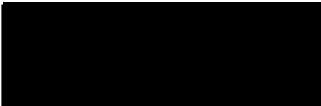# MEASUREMENTS OF FEL DYNAMICS

Allan M. MacLeod

A thesis submitted in partial fulfilment of the requirements of
the University of Abertay Dundee for the degree of
Doctor of Philosophy

This research programme was carried out in collaboration with
the FOM Instituut voor Plasmafysica "Rijnhuizen",
3430 BE Nieuwegein, The Netherlands.

February 1999

I certify that this thesis is a true and accurate version of the thesis approved by the external examiners.

Signed .... ███████████ .... Date ..$30/04/99$

Declaration

I hereby declare that while registered as a candidate for the degree for which this thesis is presented I have not been a candidate for any other award. I further declare that, except where stated, the work in this thesis is original and was performed by myself.

Signed.. ████████████ ......(Allan Myron MacLeod) Date....$30/4/99$.

Acknowledgements

Measurements of FEL dynamics

Allan M. MacLeod

Abstract

The design, implementation and commissioning of a time-resolved electron energy spectrometer system are discussed. Since its installation at the FELIX free-electron laser user facility in Nieuwegein, The Netherlands, the spectrometer system has been in regular use as a diagnostic and investigative tool. The system provides 0.2% energy resolution with 32 channels, and time resolution of 50 ns. The spectrometer is positioned immediately following the undulator so that the gain medium—the relativistic electron beam—can be probed immediately following its interaction with the optical field in the laser cavity. The system permits real-time calculation and graphical display of key beam parameters as well as the archiving of raw data, and has been used to provide insight into the operation of an FEL in the high slippage, short pulse regime. In particular, direct measurement of the extraction efficiency is possible from macropulse to macropulse. A systematic study of efficiency as a function of wavelength and cavity desynchronisation has been undertaken. At low values of cavity desynchronisation the efficiencies measured exceed the conventional $1/2N$ estimate by between 50% and 100% and these results are shown to be consistent with the formation of ultrashort optical pulses—approximately of 6 optical cycles in length. An investigation into the way in which the electron beam energy can be swept on a microsecond time scale has made it possible to produce given sweeps in wavelength—of up to 2%, limited only by the constraints of the electron beam transport system—which have been used by molecular spectroscopists to excite target molecules through an anharmonic ladder of states. Further evidence for the recent observation of superradiance in an FEL oscillator has been provided by an investigation which shows that the efficiency and intracavity power of the radiation scale respectively as the inverse square root and the inverse square of the cavity losses, verifying the superradiant scaling laws predicted by the supermode theory. An important consequence of this observation is that it indicates that shorter and more intense optical pulses may be produced by increasing the bunch charge and reducing optical cavity losses.

Contents

Chapter 1 General Introduction

1.1 Introduction

This chapter provides an introduction to the basic principles of operation of a free-electron laser (FEL) in sufficient depth to serve as a background for the material in the remainder of the thesis. Section 1.2 describes the amplification mechanism. Since the thesis is concerned in the main with results taken at the Free-Electron Laser for Infrared eXperiments (FELIX) at Nieuwegein in The Netherlands, an FEL that operates in the large slippage regime, section 1.3 covers the short pulse effects that are so important in FELs operating with large slippage. In section 1.4 a brief description of the FELIX facility is presented, including the layout, the general performance and the principal diagnostics. The design, construction and use of one of these—a time resolved electron energy spectrometer system—is central to this thesis. A brief outline of the work covered in the remainder of the thesis is given in section 1.5.

The operation of a free-electron laser (FEL) was first demonstrated at Stanford University in 1975 by Madey and his co-workers [1,2]. In the following twenty or so years, FELs have proved to be valuable and versatile scientific tools, by virtue of their continuous and easily accessible wavelength tuning range, high optical power and short pulses. This flexibility is a consequence of the use of a relativistic pulsed electron beam as the gain medium. The electron beam from an appropriate accelerator (usually a radio-frequency linear accelerator, or RF-linac) is guided into a region of spatially periodic magnetic field, called an undulator or wiggler. The electrons are constrained to move along an undulating path by the spatially alternating magnetic field, and consequently emit electromagnetic radiation with a relativistic frequency upshift that can be adjusted to span the wavelength region of interest. This radiation is captured in an optical cavity and amplified on successive passes through the undulator in the presence of the gain medium of freshly injected electrons [3].

Early FELs were built almost exclusively around existing accelerators which had been designed for other purposes and which, in general, did not have the necessary beam quality in terms of emittance, brightness and energy spectrum for use in a FEL. Improvements in accelerator technology led to the design of accelerators specifically for FELs. Increased reliability allowed the creation of user facilities where FEL beam time was shared between different scientific users and, in some cases, was available round-the clock. The first FEL user facility in Europe was the Free-Electron Laser for Infra-red eXperiments, FELIX, at Nieuwegein in The Netherlands, followed closely by the Collaboration pour un Laser Infrarouge à Orsay, CLIO, at the Université de Paris Sud. User facilities in the USA include the Advanced Free Electron Laser (AFEL) at Los Alamos National laboratory and the Stanford Picosecond FEL Center. A comprehensive survey of present-day facilities is given in [4] and [5] and Figure 1.1 summarises these data showing operational FEL user facilities with the wavelength ranges accessible at each at the time of writing.

The combination of rapid tunability (in a spectral region where other sources are scarce), high power, and short pulses makes the RF-linac-driven free-electron laser especially suitable for a wide range of experiments involving non-linear phenomena: for example the study of fast relaxations in atomic and molecular systems [6], medical applications [7] and multiphoton absorption in fullerenes resulting in almost fragmentation-free ion spectra [8]. However, FELs operating in the infrared at wavelengths shorter than about 20 μm now face competition from relatively inexpensive table-top laser systems based on optical parametric oscillators in the near-infrared and subsequent down-conversion in non-linear crystals [9-11]. This competition has shifted the optimum operating regime of FELs to longer infrared wavelengths. Consequently, operation at wavelengths beyond 20 μm has been implemented or proposed at several FEL user facilities [12-16].
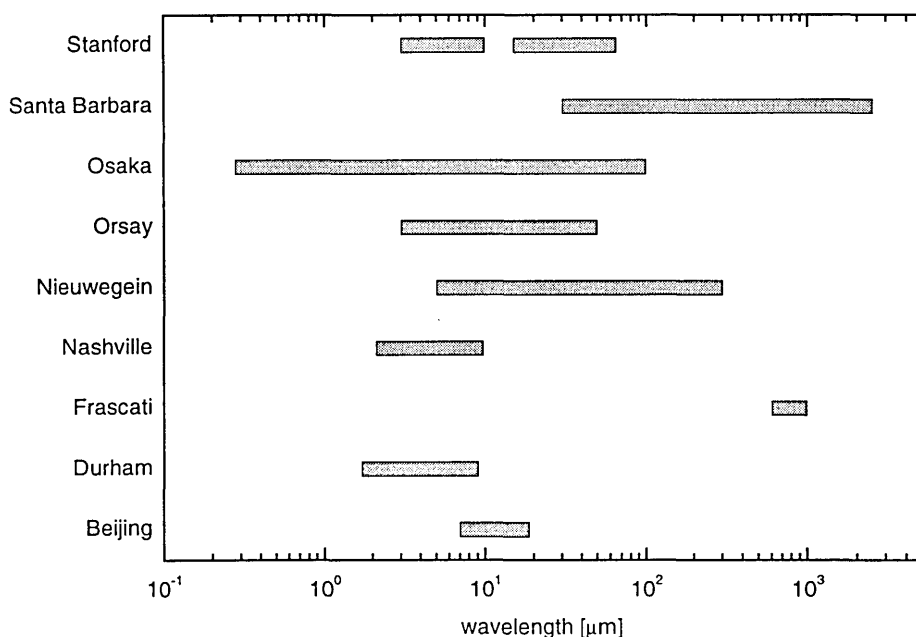
Figure 1.1 *Overview of operational FEL user facilities in 1999, using data from references [4] and [5]*

1.2 FEL principles

The free-electron laser produces radiation not, as in the case of conventional lasers, as a result of transitions of electrons that are constrained to move between atomic or molecular energy levels, but as a result of the oscillations of free – i.e. unbound – electrons [17-19]. The interaction in a free-electron laser is between a relativistic electron beam and a spatially periodic magnetic field. The spatially periodic magnetic field is produced by an *undulator*, which may comprise an array of permanent magnets of alternating polarity – a planar undulator – or may, as is frequently the case in a helical undulator, be provided by currents in suitably constructed coils.

A typical planar undulator configuration is shown in Figure 1.2. In the undulator, the electrons perform a transverse wiggling motion in one plane due to the Lorentz force and, from basic electromagnetic theory, radiate dipole radiation. The relativistic 'headlight' effect ensures that this radiation is confined to small angles around the forward direction. The presence of the spatially periodic magnetic field of the undulator significantly narrows the spectrum of the radiation compared to synchrotron radiation, which is produced by essentially the same mechanism, by enforcing a resonance condition: the electrons, travelling at just below the speed of light, must slip behind the light by exactly one wavelength in the time they take to traverse one undulator period. The resonance condition may be expressed in terms of the radiation wavelength, λ_0, the electron energy, γmc^2, and the undulator parameters as

$$\lambda_0 = \frac{\lambda_u}{2\gamma^2}(1 + K^2),$$

(1.2.1)

where λ_u is the period of the undulator field and K is a dimensionless parameter proportional to the magnetic field amplitude. Typically K is of the order of unity and $\gamma^2 \gg 1$ for the highly relativistic electron beam. This is spontaneous emission and it is incoherent and weak compared to the laser radiation, although it is produced by the same fundamental mechanism.
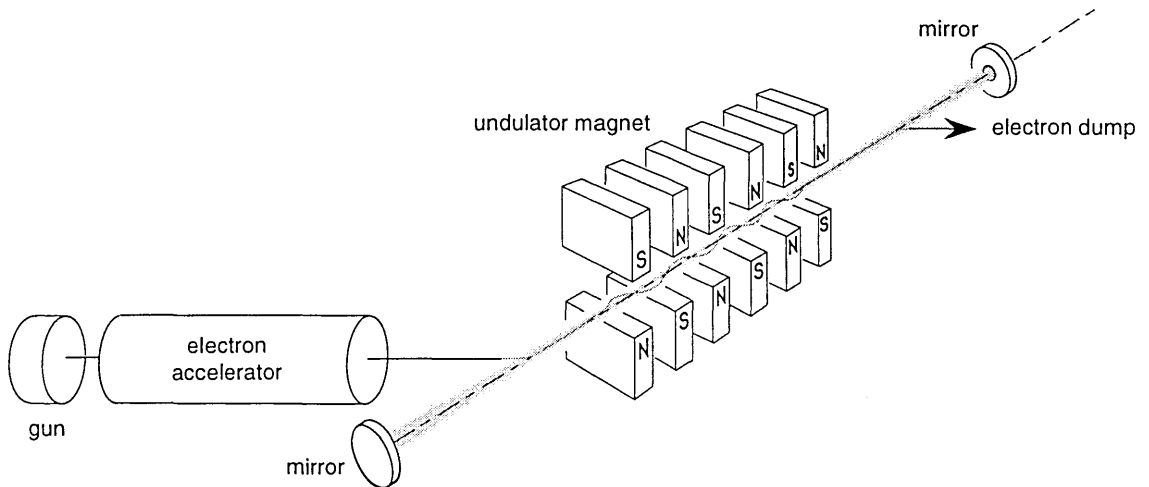
Figure 1.2 *Schematic layout of the FEL oscillator. A relativistic electron beam is injected into a spatially periodic magnetic field produced in the undulator. The magnetic field forces the electrons to perform a 'wiggling' motion that causes the electrons to radiate. The radiation is stored in the cavity formed by two the mirrors and amplified, on successive round trips, by freshly injected electrons.*

The presence of the radiation field means that electrons now interact with the combined fields from the undulator and the radiation in such a way that the electrons form short bunches which can then radiate coherently. Bunching arises because the electromagnetic wave characterised by an angular frequency ω and wavenumber k_0 and the magnetostatic field from the undulator characterised by a wavenumber k_u produce a beat wave with the same frequency as the electromagnetic wave but with a wavenumber

given by the sum of the wavenumbers of the electromagnetic wave and undulator field – i.e. $k_0 + k_u$. This beat wave, also known as a ponderomotive wave, has a velocity $v < c$ given by $v = \omega/(k_0 + k_u)$ and matching this to the axial electron velocity yields precisely the resonance condition (1.2.1). It is the interaction between transverse oscillations of the electrons and the transverse magnetic field of the ponderomotive wave that gives rise to an axial force, normal to both, which causes the electrons to bunch around certain phases of the ponderomotive wave. In this condition electrons with energies slightly higher than that required for resonance lose energy to the radiation field while those with energies slightly below that of resonance gain energy at the expense of the radiation field.

Several important observations can be made even from this simplified picture. Bunching of the electrons on an optical-wavelength scale leads to the possibility of the bunches radiating coherently. However, if all electrons have precisely the resonant energy, $\gamma = \gamma_R$, bunching occurs but, on average as many electrons lose energy to the radiation field as absorb energy from it and there is no net gain. When the energy of the electrons is slightly greater than the resonance energy, $\gamma > \gamma_R$, bunching occurs – with the bunches radiating coherently – and in addition the electrons can lose energy to the radiation field thereby producing gain. Conversely, electrons with energies slightly less than resonance, $\gamma < \gamma_R$, will gain energy by absorbing it from the radiation field. The gain curve shown in Figure 1.3 is therefore asymmetric, showing positive gain at energies just higher than resonance (i.e. wavelengths just shorter than λ_0) and negative gain for wavelengths just longer than λ_0. The precise mathematical form of the gain curve is derived in numerous works e.g. [17,18,19].
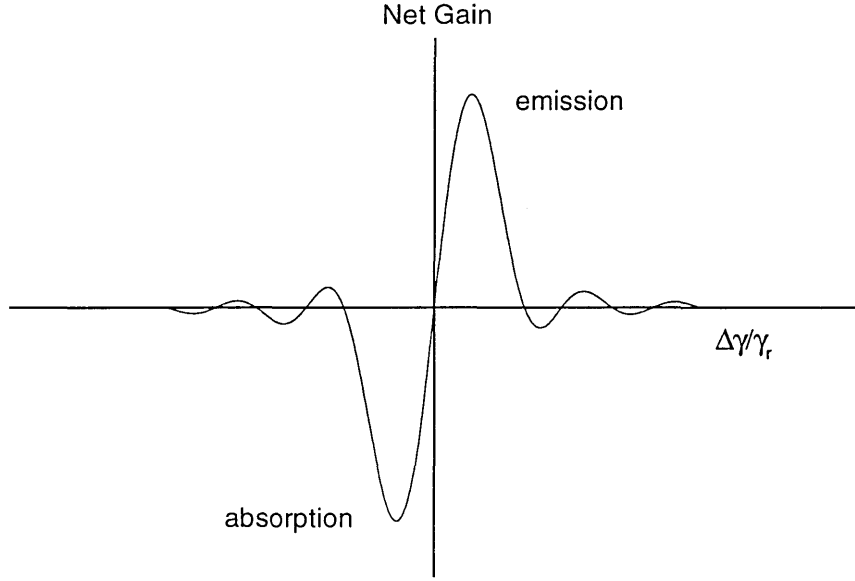
Figure 1.3 *The asymmetric small-signal gain curve of an FEL. Gain is shown as a function of relative energy difference from the resonance energy,* γ_R. *Derivations of this expression may be found in [17,18,19].*

These ideas can be represented very elegantly using the concept of phase space. A fuller 1-dimensional mathematical treatment, e.g. [20], shows that the electron motion can be represented in terms of the variables $\eta = (\gamma - \gamma_R)/\gamma_R$, the relative electron energy detuning from the resonant energy $mc\gamma_R$, and $\theta = (k_u + k_0)z - k_0 ct$, the phase of the electron in the ponderomotive wave (z and t are the space and time co-ordinates of the electrons in the lab frame) as follows.

$$\dot{\eta} = -\Omega^2 \sin\theta \qquad (1.2.2)$$

$$\dot{\theta} = 2ck_u\eta \qquad (1.2.3)$$

where $\Omega^2 = \dfrac{eKE_r}{mc\gamma_R}$, e is the charge of an electron, E_r is the amplitude of the radiated electric field, a dot represents differentiation with respect to time and the other symbols have their usual meanings. Note that equations (1.2.2) and (1.2.3) can be reduced to one second-order equation, which is identical in form to the equation describing the motion of a pendulum:

$$\ddot{\theta} + 2ck_u\Omega^2 \sin\theta = 0 . \qquad (1.2.4)$$

The equation (1.2.4) has an exact mathematical solution in terms of Jacobi elliptic functions, but it is more instructive to look at qualitative results deduced from the (θ, η) phase space for the pendulum equation. Recall that η is a measure of the electron energy and θ is the co-ordinate of the electron in a frame moving with the phase velocity of the ponderomotive wave, $v_{ph} = \omega/(k_u + k_0)$.
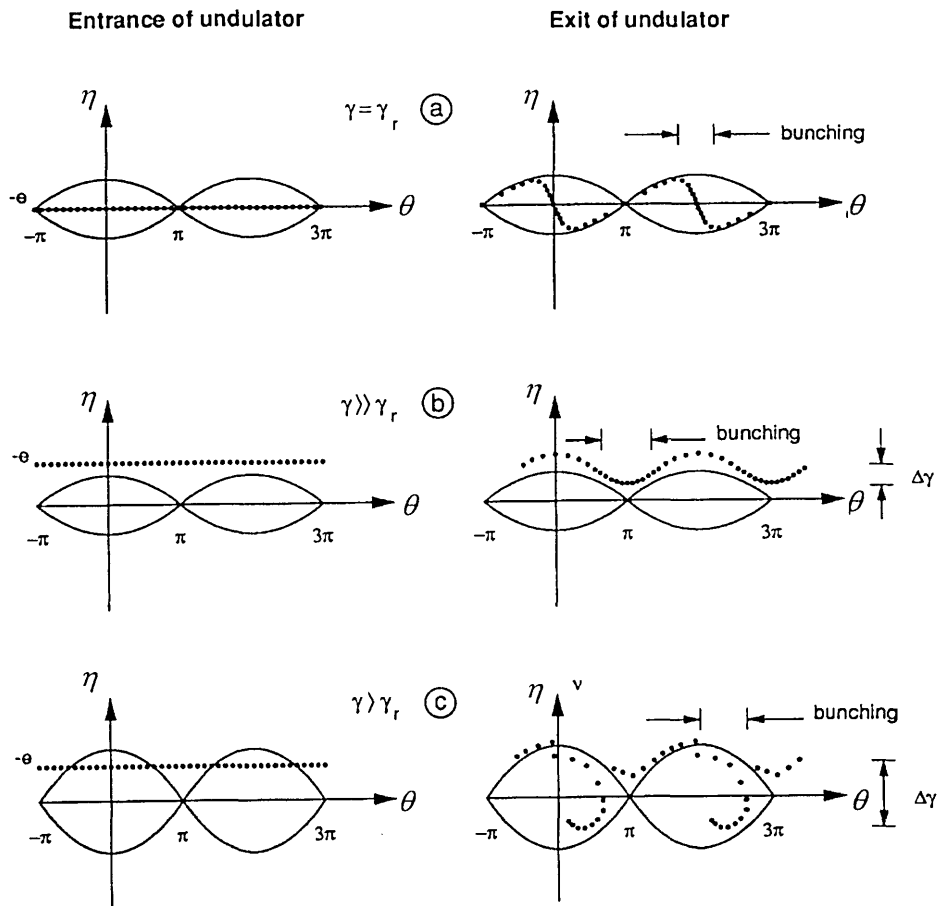
5

Entrance of undulator   **Exit of undulator**

Figure 1.4 *These plots represent the evolution of electrons, initially uniformly distributed in phase and injected at three energies: (a) at resonance, (b) far from resonance, and (c) just above resonance. The left-hand figures show the distribution of the electrons in phase space at the entrance of the undulator. The corresponding distribution at the end of the undulator is shown in the right hand figures.*

Figure 1.4 shows the trajectories of various typical electrons in this representation. Electrons that have energies near resonance follow closed trajectories in phase space as in (a). Such electrons are trapped by the ponderomotive potential and can either lose energy, corresponding to downward movement in the diagram, or gain energy, corresponding to upward movement. Electrons far from the resonant energy follow non-closed trajectories, as in (b) and have little interaction with the field. The unique trajectory that separates these two classes is known as the separatrix, whose importance will become apparent when saturation is considered.

Bunching of electrons is also apparent in this representation and is shown in the diagrams on the right of Figure 1.4. These plots represent the evolution of electrons, initially uniformly distributed in phase and injected at three energies: (a) at resonance, (b) far from resonance, and (c) just above resonance. The left-hand figures show the distribution of the electrons in phase space at the entrance of the undulator. The corresponding distribution at the end of the undulator is shown in the right hand figures. It can be seen that for electrons at the resonance energy there is no net energy lost or gained by the

electrons since the distribution is symmetrical about the horizontal axis. Figure 1.4 (b) illustrates the case of electrons which are far above resonance energy. When the optical field strength is weak the size of the ponderomotive potential is small and most electrons fall into this category. In this situation, little energy is lost but considerable bunching takes place. This results in a greater intensity of *coherent* emission and increases the optical field intensity. Figure 1.4 (c) shows the situation where the ponderomotive potential is large or the electrons are close to resonance. Most electrons are trapped by the ponderomotive potential and lose energy as they evolve in phase space. The maximum energy is extracted from an electron if it moves from the top separatrix to the bottom as illustrated by the amount $\Delta\gamma$ in Figure 1.4 (c). It can be shown that under these circumstances the extraction efficiency of the FEL is given by $\eta \approx 1/2N_w$ [18].

The basic mechanisms for the production of spontaneous and coherent spontaneous emission have been described in the preceding paragraphs and it has been seen that the optical field intensity can grow due to the interaction of electrons with the ponderomotive field produced by the combined magnetostatic and electromagnetic fields. This is *stimulated* emission because it does not occur until the electrons have been bunched by the ponderomotive field. Furthermore, the phase space description shows that saturation takes place because the electrons evolve in phase space in such a way that they eventually start to absorb energy from the ponderomotive potential. If, for example, the electrons shown at the end of the undulator in Figure 1.4(c) continued in a further section of undulator, their distribution would sweep upwards again as they absorb energy. This is reduces gain and causes the laser to saturate (see section 1.3.4).

The description so far is of a single-pass laser amplifier. In most practical FELs the single-pass gain is too small to provide useful radiation and it is necessary to trap the radiation in an optical cavity enclosing the undulator so that the radiation can be amplified by fresh electrons on each subsequent pass down the undulator.

1.3 Short pulse effects

This section summarises concepts and mechanisms that are especially important for FELs such as FELIX that operate with a combination of short electron bunch lengths and long optical wavelengths. FELIX was the first FEL to be operated under these conditions and two new modes of operation have been observed as a consequence: the so-called limit-cycle regime [21] and the superradiant regime [23].

Most FELs that operate in the infrared part of the spectrum use an RF-linac to provide the electron beam. An RF-linac produces a pulsed electron beam, consisting of electron bunches with a typical duration of a few picoseconds. These bunches are produced at the frequency of the accelerating potential which may typically be in the range from 10 MHz to several GHz. Furthermore, few RF-linacs can operate continuously so that the electron bunches are produced in bursts lasting for a few tens of microseconds. The resulting optical radiation exhibits the same structure: the picosecond-long optical

pulses are called *micropulses* and the train of micropulses is called a *macropulse* (see Figure 1.5).
Superconducting RF-linacs can, however, provide an almost continuous train of micropulses – i.e. CW operation.

MACROPULSE
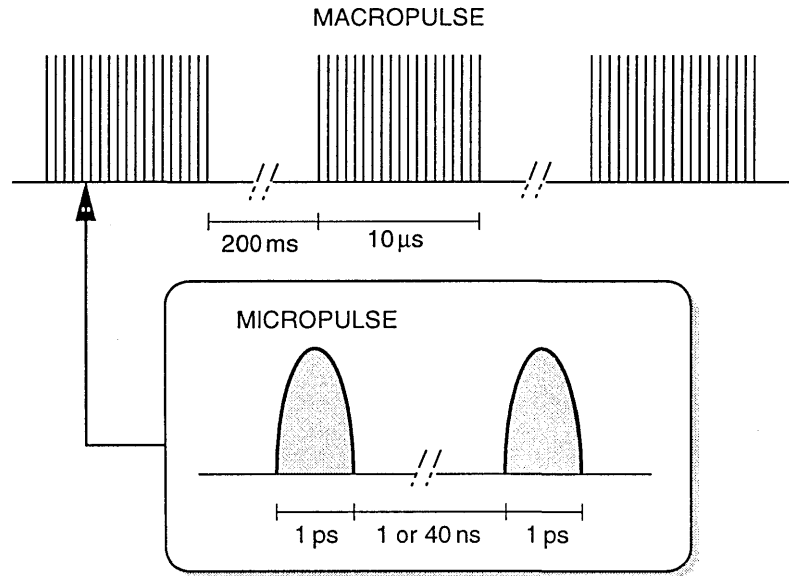
Figure 1.5 *Time structure of the electron beam provided by an RF-linac. The optical pulse structure is basically the same as the electron beam pulse structure.*

1.3.1 Slippage

The idea of slippage has already been introduced in section 1.2. Slippage refers to the fact that the electrons fall behind the optical field which they generate because (1) their velocity must be less than the speed of light, and (2) the electrons follow an undulating path. The distance that the electrons slip behind the radiation is constrained by the resonance condition (1.2.1) to be one radiation wavelength in the time taken to traverse one undulator period. An important length scale for short-pulse effects is the slippage length, L_s, which is the distance by which the optical pulse advances relative to the electron bunch during the passage through the undulator. In each undulator period the radiation moves ahead of the electrons by one radiation wavelength, so that on an undulator of N_w periods the slippage length will be given by $L_s = N_w \lambda$. Two consequences of slippage are: each individual electron interacts with a portion of the radiation field of length L_s; while each position in the propagating field is influenced by electrons in a length no greater than L_s of the electron beam – less than L_s if the electron bunch length is shorter than L_s.

The ratio of the slippage length to the electron bunch length σ_z – to be precise, σ_z^2 is the variance associated with the longitudinal electron distribution – is known as the slippage parameter, or longitudinal coupling parameter $\mu_c = N_w \lambda / \sigma_z$ and is a measure of the importance of short pulse effects. When $\mu_c < 1$, a large part of the optical pulse develops as if the electron beam were

continuous. Only at the beginning and end of the optical pulse are there regions where electrons and radiation are not in contact for the entire transit through the undulator: the front of the optical pulse interacts with electrons only at the beginning of the undulator, before the radiation escapes the electrons due to slippage; and the rear of the optical pulse is produced by the electrons at the rear of the electron bunch as they near the end of the undulator. As soon as the slippage length becomes comparable with the electron bunch length, transient effects at the beginning and end of the pulses can become important.

The slippage length is not always the most appropriate parameter to use to characterise short pulse effects. For example, in a high-gain single-pass device the radiation field reaches saturation before the end of the undulator and therefore the full slippage length is not an appropriate parameter to use. In that case the co-operation length [24] is an appropriate parameter. In a low-gain oscillator configuration, such as at FELIX, the optical pulses are stored in a resonator or cavity formed by mirrors at either end of the undulator, and amplified by fresh electron pulses on successive round trips in the cavity. In this case the end effects can accumulate and become observable even in cases where the slippage length is considerably less than the bunch length. Co-operation length is also an important concept when considering the evolution of short, superradiant optical pulses in a free-electron laser oscillator [23,25].

1.3.2 Lethargy

The effect of short electron pulses on the gain in successive round trips is illustrated qualitatively in Figure 1.6 which shows the relative positions of the electron and optical pulses at the entrance and exit of the undulator for three successive round trips. At the top of the figure an electron pulse and an optical pulse are shown at the entrance to the undulator. As they pass through the undulator, the optical pulse advances by the slippage length relative to the electron pulse and, at the same time, grows because of the gain mechanism described earlier in this chapter. Note that the leading part of the optical pulse shows relatively little gain because it loses contact with the electrons in the first part of the undulator. This effect is not simply due to slippage: the electrons entering the undulator are not bunched until they have gone some way along its length and therefore do not contribute significantly to the growth of the radiation field until they radiate coherently, due to bunching, towards the end of the undulator. This position-dependent gain results in the optical pulse peaking at its trailing edge while its leading edge loses contact with the electrons and experiences no gain. This can be interpreted as a reduction in the *group velocity* of the light pulse. The simplified description of the effect of slippage given in the previous section is therefore no longer valid: although electrons do indeed slip back by the distance L_s with respect to an optical pulse moving at the speed of light, c, they can in fact move ahead of the peak of the optical pulse that is moving at the group velocity which is less than c.

In the next round trip, shown in the middle part of the figure, the optical pulse at the entrance to the undulator is shown with a slightly reduced intensity because of cavity losses. As a result, in successive round trips, the front of the optical pulse decays more and more while a peak grows at the rear. Note, however, that the growth of the rear of the pulse is restricted because for most of the passage down the

undulator the electrons are interacting with the low intensity field at the front of the pulse. This effect is known as laser lethargy and results in the pulse growing slowly or not at all [26]. Lethargy is important during the build up of the optical field but is not important when saturation has been reached: at saturation the rear of the pulse cannot grow because of the reduced gain and therefore the group velocity of the optical pulse returns to c and the optical pulse shape remains constant.
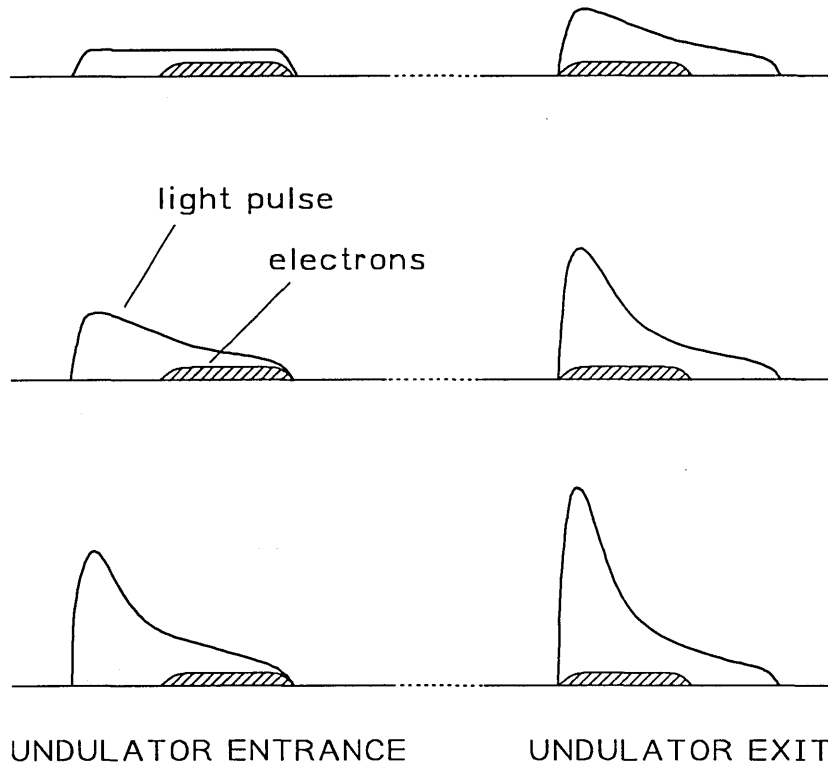
Figure 1.6 *Illustration of the effect of slippage on the growth of the optical pulse. The relative positions of an electron bunch and an optical pulse are shown at the entrance and exit of the undulator in a situation where the optical cavity has been adjusted for* **perfect synchronism** *between the circulating optical pulse and the newly arriving electron bunches. Successive round trips are shown from top to bottom. The leading part of the optical pulse does not grow because it interacts with the electrons only in the first part of the undulator where the gain is low because the electrons are not yet bunched.*

1.3.3 Cavity desynchronisation

The lack of gain at the leading edge of the optical pulse described in the previous section results in the slow build-up of optical power. This can be compensated by a slight shortening of the cavity length – usually termed cavity desynchronisation. Instead of arranging that the round trip time of the optical pulse exactly matches the repetition rate of the electron bunches—i.e. the optical round trip time is an integer multiple of the repetition rate, which is the case for a synchronised cavity—the cavity length is reduced by a small amount δL from its synchronous value. The optical pulse then arrives at the entrance of the undulator for its next round trip slightly ahead of the electron pulse, as illustrated Figure 1.7. In

successive round trips, the part of the optical pulse which experienced little gain is moved ahead of the electrons so that the electrons experience the larger optical field from the rear of the optical pulse at the beginning of the undulator. The optical pulse can then grow without the maximum shifting continuously backwards.

Looked at from a different point of view, the combination of the reduced group velocity of the optical pulse and the shortening of the optical cavity restores the effective synchronism between the optical pulse and the electron bunch and the optical pulse can grow into a stable shape that grows uniformly.
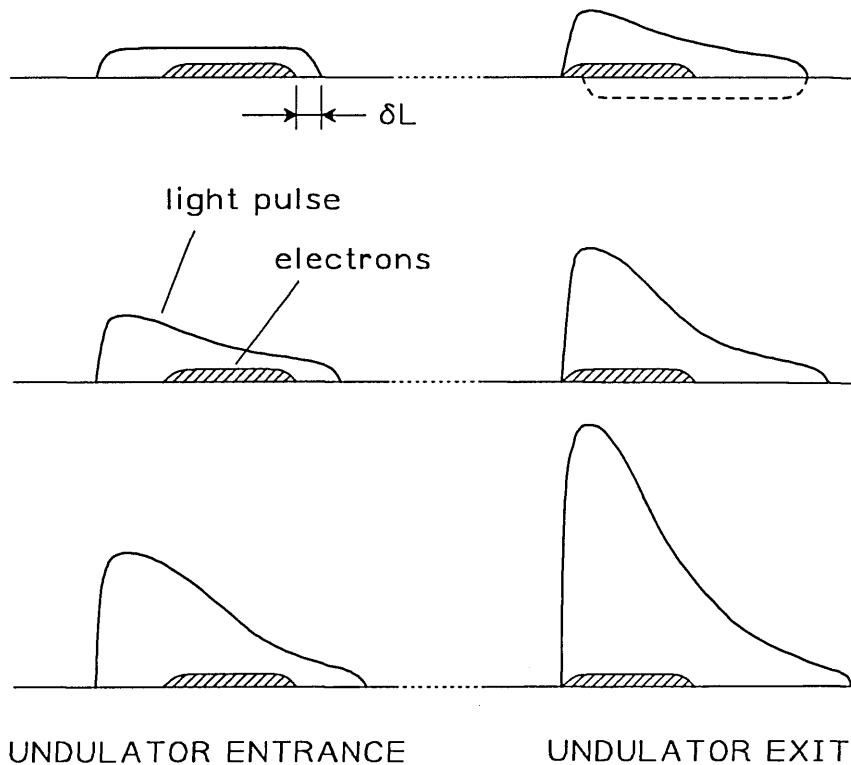
Figure 1.7 *Illustration of the effect of cavity desynchronism on the growth of the optical pulse. As previously, the relative positions of an electron bunch and an optical pulse are shown at the entrance and exit of the undulator and successive round trips are shown from top to bottom. The optical pulse can continue to grow without shifting backwards because the electron pulse experiences a higher optical field, producing efficient bunching, at the start of the undulator.*

1.3.4 Saturation

Saturation in the FEL occurs when the gain per pass drops to the level at which it equals the round trip cavity losses. When the optical field is sufficiently large, the electrons are efficiently bunched early in their passage through the undulator and they therefore emit radiation strongly and lose energy during this period. In phase space this corresponds to the electrons sweeping downwards and in a clockwise direction (Figure 1.4) then continuing their clockwise motion upwards *absorbing* energy from the optical field. This clearly reduces the total intra-cavity power and the gain per pass but does not

preclude growth at the leading edge of the optical pulse. Furthermore, under certain conditions, the optical pulse can evolve a modulation in power with a period of the order of the slippage length. The period of such modulations is the same as that of the synchrotron oscillations of the electrons in phase space and it introduces another scale length that will be of importance later, the synchrotron length, which is the distance travelled by the electrons in the observer's frame during the period of one synchrotron oscillation. This effect is known as the trapped particle instability, or sideband instability, because the modulation of the optical pulse shape introduces sidebands in the optical spectrum. Usually, this instability leads to irregular spiking operation [27]. A related manifestation of the non-linear dynamics of the electrons in the presence of strong optical fields can give rise to limit-cycle oscillations, period doubling and chaotic lasing [23]. Both limit-cycle oscillations and the period doubling phenomenon have been observed in FELIX [21].

An important consequence of the decreasing gain per pass is that the overlap between the optical pulse and the electron bunch may no longer be optimal. If the cavity has been desynchronised to overcome lethargy (see section 1.3.2), the round trip time has been set to match optical pulses with a group velocity less than c. The reduced gain at saturation means that the shape of the optical pulse remains stable so that its group velocity returns to c. Under these conditions the optical pulse moves ahead of the electron bunch, the portion which loses contact decays due to the round-trip losses, and the saturated power is consequently less than for a perfectly synchronised cavity. It seems, therefore, impossible to have both a rapid onset of lasing, which requires the cavity to be desynchronised and a large saturated power, which requires a synchronised cavity. The technique of dynamic cavity desynchronisation [22] manipulates the electron energy within the time of a macropulse so that both a relatively rapid start-up and a high maximum power can be obtained simultaneously.

1.3.5   Superradiance

Superradiant emission is characterised by having a peak intensity that scales as the square of the number of emitters N_e^2 and has for some time been predicted to occur in high-gain FEL amplifiers whereas theoretical and experimental results for long-pulse FELs indicate a saturated intensity scaling as $N_e^{\frac{4}{3}}$ [24]. Recent work has shown that superradiance is a general characteristic of FEL devices including low gain oscillators, and it has been experimentally observed at the FELIX facility [23].

1.4   FELIX

The Free-Electron Laser for Infrared eXperiments (FELIX) has been designed as a versatile source of radiation in the infrared and far-infrared regions. At the time of writing the spectral range is from 5 μm to 300 μm and is covered by two separate FEL branches. The long wavelength section (16 μm – 300 μm) is provided by FEL-1, while the short wavelengths (5 μm – 35 μm) are covered by FEL-2. FEL-1, which was originally designed to lase in the range 16 μm – 110 μm, was upgraded in 1998 by

the installation of a waveguide inside the undulator that extended its operating range to its present long-wavelength limit of 300 μm. A schematic layout of the machine is given in Figure 1.8.

1.4.1 The electron beam

The electron beam injector is formed by a thermionic triode electron gun that is modulated at 1 GHz to generate electron bunches with 1 ns separation. The electron bunches contain approximately 200 pC o charge and are of 200 ps duration. To inject these bunches into the 3 GHz travelling wave linear accelerator, the bunch duration is shortened by a prebuncher and buncher section. The 1 GHz prebuncher induces a velocity modulation on the electron bunch by the application of a rapidly varying electric field. The velocity modulation is such that the leading electrons slow down while the trailing electrons speed up. This velocity modulation results in a compressed bunch duration of about 40 ps at the end of the drift section between the prebuncher and the buncher. In the 3 GHz buncher a similar procedure is applied in 14 separate RF cavities, leading to the bunch duration of 6 ps that is necessary for injection into the first linac. The electron energy at the entrance to linac 1 is roughly 3.8 MeV so that the 200 pC bunches are no longer strongly influenced by space charge effects. The energy at the exit of linac 1 may be set to between 14 and 25 MeV by adjusting the amount of RF power fed to the linac. The beam is then either injected into FEL-1 or accelerated further, up to a maximum of 45 MeV, and injected into FEL-2. A chicane in the beam line, consisting of three quadrupole magnets between two dipoles, is used to direct the beam into the FEL resonator. This bending section is close to achromatic but has a slight non-isochronicity of about 0.2 mm/%. The bunch length may therefore be further compressed in this section by arranging for the bunch to have an appropriate energy distribution as it enters the chicane. An overview of the electron beam parameters is given in Table 1-1.
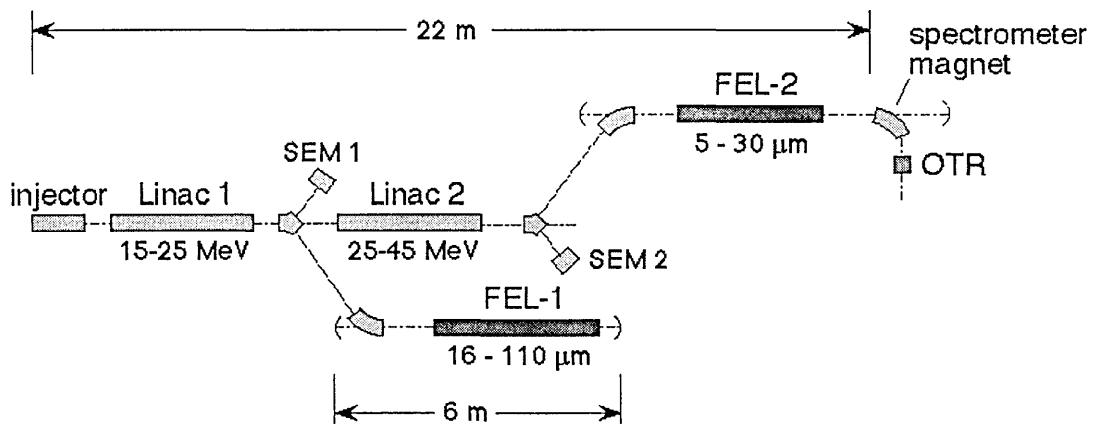
Figure 1.8 *The basic layout of the Free Electron Laser for Infrared eXperiments (FELIX). Two separate FEL sections are used to cover the wavelength range from 5-300 μm. The positions of the electron-beam diagnostics discussed in chapter 2 are indicated: SEM 1 and SEM 2 are secondary emission monitors and OTR is an optical transition radiation monitor.*

Table 1-1

Beam energy	14 – 46 MeV
Energy spread (rms)	0.2%
Normalised emittance	50π mm mrad
Bunch length (rms)	0.4 – 0.6 mm
Bunch charge	140 – 200 pC
Microbunch spacing	1 ns or 40 ns
Macropulse duration	$\leq 10\,\mu s$
Macropulse repetition rate	≤ 5 Hz

Note that the electron bunch separation may be switched between 1 ns and 40 ns. This is achieved by an additional modulation of 25 MHz at the electron gun, superimposed on the 1 GHz modulation. When set to 40 ns, there is only one optical pulse circulating in the cavity, which is useful when the radiation from FEL-2 is used to study fast phenomena with relaxation times greater than 1 ns.

1.4.2   The undulator and optical cavity

FEL-1 and FEL-2 have identical undulator sections consisting of two rows of samarium-cobalt permanent magnets forming 38 periods of length 65 mm. The distance between the rows can be varied to change the K value of the undulator and thereby alter the wavelength of the laser radiation over a time scale of a few tens of seconds. The maximum value of K, which corresponds to the longest wavelength radiation, is obtained when the gap size is at the minimum determined by the size of the electron beam vacuum tube. Table 1-2 lists the important parameters for the undulator and optical cavity.

Table 1-2

	FEL-1	FEL-2
Cavity length	6.0 m	6.15 m
Rayleigh length	1.2 m	1.2 m
Curvature of upstream mirror	3.0 m	2.783 m
Curvature of downstream mirror	4.0 m	4.0 m
Aperture radius	1.5 mm	1.0 mm
Cavity round trip loss	5 – 15%	5 – 10%
Mirror reflectivity at 10.6 μm	> 98%	> 98 %
Mirror radii	25 mm	25 mm
Vacuum tube width	27.0 mm	16.7 mm
Undulator period	65 mm	65 mm
Number of periods	38	38
Undulator strength (K)	< 1.3	< 1.9

In each FEL, the cavity consists of two gold-coated copper mirrors placed at opposite ends of the undulator. The measured cavity round-trip losses are shown in Figure 1.9. At the downstream end of the undulator the electrons are bent out of the optical cavity. In FEL-1 the electrons are simply dumped, but in FEL-2 the bending magnet was designed as a magnetic spectrometer, which is described in detail in Chapter 2. The total cavity length is 6 m, with the undulator positioned asymmetrically towards the downstream end. The curvature of the mirrors gives the optical beam a waist near the centre of the undulator and a Rayleigh length of 1.2 m. The downstream mirror is held in a solid gimbal mount carried by a precision translation stage, coupled to the vacuum system by bellows. Angular and longitudinal adjustments are made with motorised micrometers and the distance between the cavity mirrors is actively controlled to within 0.5 μm by a Hewlett-Packard laser interferometer system. A fraction of the optical radiation generated in the FEL cavity is coupled out through a hole in the upstream mirror and is guided in an evacuated transport system from the accelerator vault to the user stations in the experimental area. The optical beam line is evacuated to prevent absorption, and separated from the linac vacuum system by diamond windows at the Brewster angle.
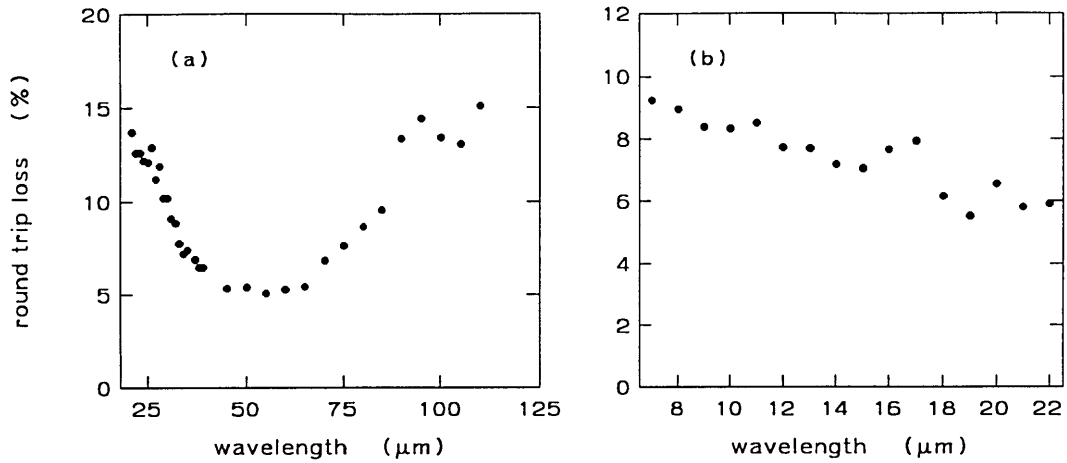
Figure 1.9 *The measured round-trip loss in FEL-1 (a) and FEL-2 (b). The losses are estimated from the ringdown time of the radiation coupled out through the aperture in the upstream mirror. The losses in FEL-1 increase at short wavelengths due to the formation of high-order transverse modes and at long wavelengths due to clipping of the optical field by the electron-beam vacuum tube in the undulator.*

1.4.3 Performance

Saturated laser output is achieved over the wavelength range 5 – 110 µm: full characterisation of FEL1 between 110 µm and 300 µm has not yet been completed at the time of writing. The wavelength can be changed relatively rapidly by means of altering the undulator field strength: a variation of a factor of two in FEL-1 and of three in FEL-2 may be obtained in a matter of minutes. The saturated output power and the optical micropulse energy for a number of such wavelength scans is presented in Figure 1.10. When a larger wavelength change is required, a change in beam energy or even a move to the other FEL may be necessary, which takes around 30 minutes. The data shown in Figure 1.10 represent the measured power at the FELIX diagnostic station. At each electron energy, only the undulator field strength was varied. In practice, the FEL output can be optimised at any particular wavelength by adjusting the accelerator settings for that case. The power available in the user experimental area is slightly lower than these values due to losses in the transport system. The rms stability of the optical power between macropulses is typically 1 – 2% when the cavity desynchronisation is not too small.
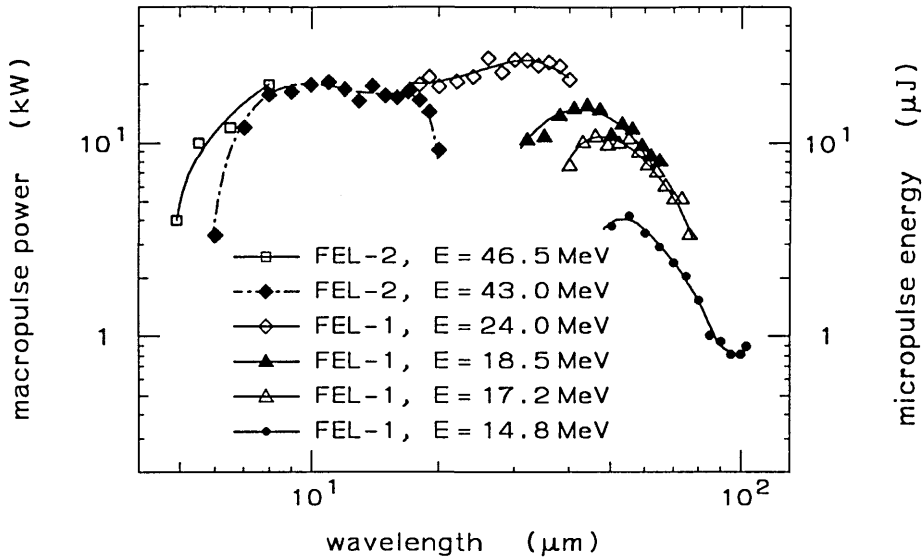
Figure 1.10 *Saturated macropulse power and micropulse energy as a function of the radiation wavelength. Results are shown for various values of the electron beam energy. At each electron energy, the wavelength is varied via adjustment of the undulator field strength.*

The micropulse duration may be tuned over roughly an order of magnitude by adjustment of the cavity desynchronism. Sub picosecond pulses have been achieved over a wide range of wavelengths and pulses as short as 200 fs have been measured leading to peak optical powers in the region of tens of MW. The combination of these high electric fields and short pulse durations make FELIX suitable for the study of non-linear phenomena and fast relaxation processes. In Figure 1.11 the optical pulse duration (a) and the width of the optical power spectrum (b) are shown for a wavelength of 24.5 μm as a function of the cavity desynchronism (solid circles). In Figure 1.11 (c) the time-bandwidth product is plotted, showing that it close to the Fourier transform limit – the theoretical time-bandwidth product is 0.31 for a $\mathrm{sech}^2 t$ -shaped pulse. The open circles in Figure 1.11(a) and (c) include the deconvolution with the 330 fs time resolution of the autocorrelator at this wavelength. Similar performance is found at other wavelengths.

1.4.4 Principal diagnostics

Several important items of diagnostic equipment have been purpose-built and used to characterise the FELIX electron and optical beams. The electron energy spectrometer, described in detail in chapter 2, provides 50 ns temporal resolution on each of 32 channels giving an energy resolution of the order of 0.2%, and was designed and built by the FEL group at the University of Abertay Dundee in close co-operation with the FELIX team. This device provides time-resolved electron energy data for each macropulse. The data may be archived for later analysis and some of it is available, in real time, in the FELIX control room.
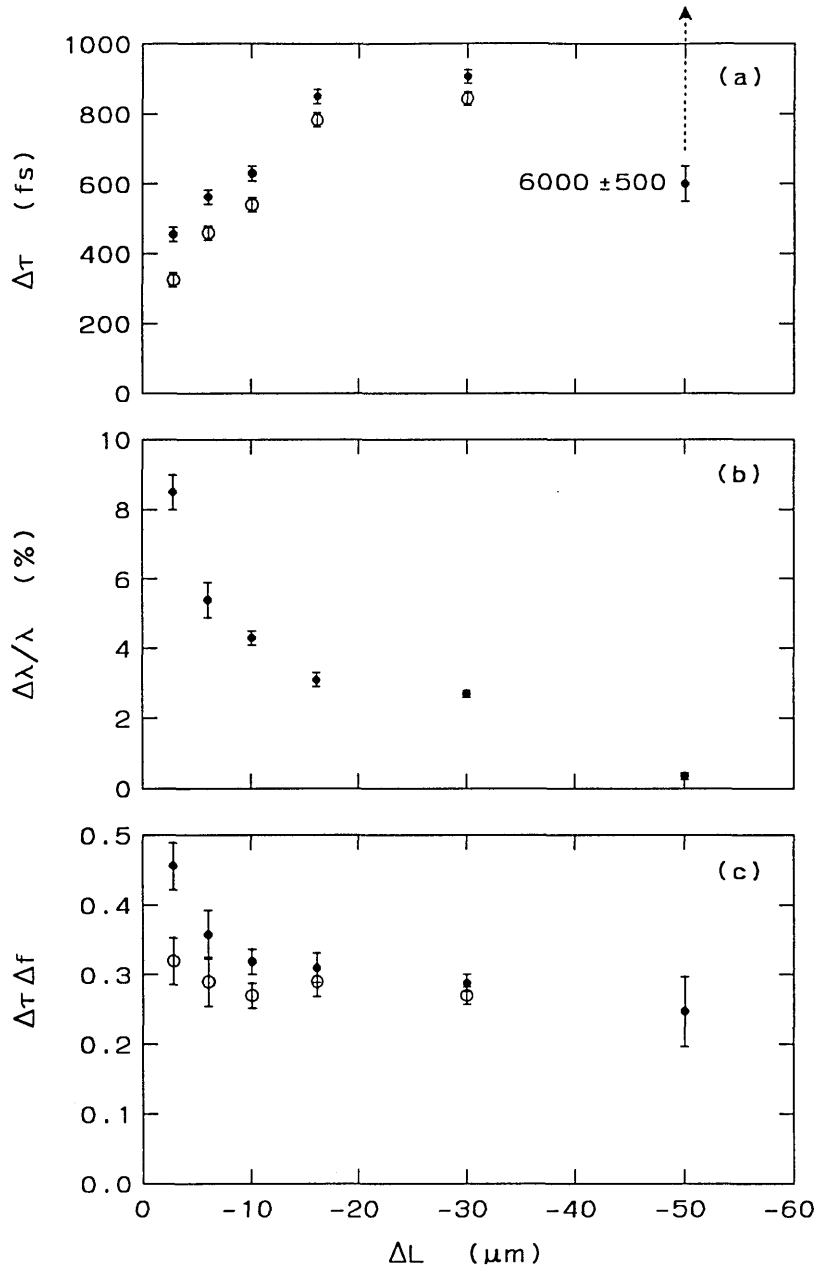
Figure 1.11 *Measured optical pulse duration (a), spectral width (b), and time-bandwidth product (c) as a function of cavity desynchronisation at a laser wavelength of 24.5 μm. All measurements (solid circles) are taken at the FWHM. The open circles represent the optical pulse duration and time-bandwidth product after deconvolution with the 330 fs time resolution of the autocorrelator at this wavelength. The deduced time-bandwidth product is close to 0.31, the theoretical value for a* $\mathrm{sech}^2(t)$ - *shaped pulse.*

A second-order optical autocorrelator, based on second-harmonic generation in a single crystal of cadmium telluride and designed and built by Dr. G. M. H Knippels of the FELIX team [28], is used to establish the optical pulse length. Recently work has commenced on a diagnostic that will provide the first direct measurement of both the FELIX optical pulse and of the shape of the electron bunch. This diagnostic uses the differential optical gating technique (DOG) [29,30] and a 10 fs pulse from a

Ti:Sapphire laser synchronised with the FELIX electron bunches. The shape of the electron bunch is obtained, in the first instance, using the mm-wave portion of the transition radiation, already produced for the electron energy spectrometer, to produce a rotation in polarisation in a crystal – through the Pockels effect – and modulate an external, visible light beam which can then be probed using DOG.

1.5   Outline of this thesis

The design of the FELIX facility started in 1987 and first lasing of FEL-1 was achieved in August 1991. Installation of FEL-2 followed and produced first laser light in August 1992. During this period the main theoretical and experimental investigations were into the hole-coupling mechanism, which was shown to operate successfully over a broad range of wavelengths, and the initial short pulse effects observed in FEL-1. One of the areas identified as requiring investigation was the need to measure the energy distribution of the electron beam immediately after the laser interaction in order to obtain a better understanding of the FEL

Damage to the gain medium in an FEL—the relativistic electron beam—is not an issue and therefore very high intracavity powers may be obtained. The time-resolved electron spectrometer described in chapter 2 allows the gain medium to be probed and its energy distribution to be measured immediately following the laser interaction. Furthermore, the gain medium is refreshed on a nanosecond time-scale and this allows the characteristics of the gain medium to be changed quickly. The spectrometer serves as a diagnostic tool for experiments in which the electron energy is ramped during lasing, producing a corresponding ramp in the wavelength of the radiation produced. Measurement of the energy distribution of the electron beam after lasing allows a direct measurement of the efficiency of the lasing process and such measurements have been used to provide the first experimental evidence for the observation of superradiance in an FEL oscillator.

An introduction to basic FEL physics and to the FELIX free-electron laser facility has been presented in the earlier sections of this chapter. Chapter 2 describes the design and construction of the principal diagnostic tool used in the work presented in later chapters: the time-resolved electron spectrometer system. The design philosophy, an overview of the system, and details of the measurements on the spectrometer magnet itself are presented in this chapter while technical details of the electronics and computer hardware and software—both of which were also designed and implemented as part of the project—are presented in an appendix. Chapter 3 covers the commissioning and initial testing of the system and the principal derived measurements are defined and illustrated.

An extensive series of efficiency and optical micropulse length measurements at various wavelengths and cavity desynchronisations is discussed in detail in chapter 4. The extremely short optical pulses obtainable in FELIX when the cavity is close to perfect synchronisation—optical pulses lasting only six cycles FWHM have been observed—give rise to much larger values of efficiency than were initially

expected using, for example, the crude $1/2N$ estimate of efficiency, where N is the number of undulator periods. The ultra-short pulses from FELIX, combined with slippage, effectively shorten the interaction time and hence the effective undulator length producing higher efficiencies. The experimental data are compared with various theoretical and numerical models. As well as characterising the FEL, the electron spectrometer has been used to study the various effects that can be obtained by manipulating the gain medium: in particular, sweeps in the initial energy of the relativistic electron beam may be used to program wavelength sweeps in the FEL radiation. Chapter 5 discusses how this can allow FELIX to be used as a voltage-controlled optical oscillator, which has found applications in molecular spectroscopy.

Superradiance was first experimentally observed in an FEL oscillator at FELIX in 1997. Chapter 6 presents a derivation, which is in agreement with a fuller theoretical treatment of the phenomenon, of the basic scaling laws for superradiance, showing that it arises from the ultra-short optical pulses produced in FELIX. Experimental measurements show directly that at near zero cavity desynchronisation the efficiency and intracavity power of FELIX scale respectively as the inverse square root and the inverse square of the cavity losses, as required by the supperradiant scaling, providing further experimental evidence for the observation of superradiance an FEL oscillator.

1.6   References

1. L.R. Elias, W.M. Fairbank, J.M.J. Madey, H.A. Schwettman and T.I. Smith, "Observation of stimulated emission of radiation by relativistic electrons in a spatially periodic magnetic field", *Phys. Rev. Lett*, **36**, 717-720, 1976.

2. D.A.G. Deacon, L.R. Elias, J.M.J. Madey, G.J. Ramian, H.A. Schwettman and T.I. Smith, "First operation of a free-electron laser", *Phys. Rev. Lett.*, **38**, 892-894, 1977.

3. G. Dattoli and A. Renieri, "Experimental and theoretical aspects of the free electron laser", in *Laser Handbook Vol. 4*, edited by M. L. Stitch and M. Bass, North-Holland, Amsterdam, pp. 1-133, 1985.

4. W.B. Colson, "Short wavelength free-electron lasers in 1997", *Nucl. Instrum. & Methods Phys. Res. A*, vol. 407, pp. 26-29, 1998.

5. G. Ramian, "The world-wide web virtual library: free-electron lasers – FELs", http://sbfel3.ucsb.edu/www/fel_table.html

6. B.N. Murdin, M. Kamalsaadi, C.M. Ciesla, C.R. Pidgeon, C.J.G.M. Langerak, R.A. Stradling, E. Gornik, "Landau level lifetimes in an InAs/AlSb quantum well determined by a picosecond far-infrared pump-probe technique." *Phys. Stat. Sol.* B, Vol.204, No.1, pp.155-158, 1997.

7. G.S. Edwards, D. Evertson, W. Gabella, R. Grant, T.L. King, J. Kozub, M. Mendenhall, J. Shen, R. Shores, S. Storms, R.H. Traeger, "Free-electron lasers: Reliability, performance, and beam delivery." *IEEE Jour. Sel. Top. in Quant. Elect.*, 1996, Vol.2, No.4, pp.810-817

8. G. von Helden, I. Holleman, G. M. H. Knippels, A. F. G. van der Meer and G. Meijer. "Infrared resonance enhanced multiphoton ionization of fullerenes", *Phys. Rev. Lett.*, 1997, **79** No. 26, pp. 5234-5237.

9. A. Dhirani and P. Guyot-Sionnest, "Efficient generation of infrared picosecond pulses from 10 to 20 μm", *Opt. Lett*, vol. 20, pp. 1104-1106, 1995.

10. F. Seifert, V. Petrov and M. Woerner, "Solid-state laser systems for the generation of mid-infrared femtosecond pulses tunable from 3.3 to 10 μm", *Opt. Lett*, vol. 19, pp. 2009-2011, 1994.

11. I. M. Bayanov, R. Danielius, P. Heinz and A. Seilmeier, "Intense subpicosecond pulses tunable between 4 μm and 20 μm generated by an all-solid-state laser system", *Opt. Commun.*, vol. 113, pp. 99-104, 1994.

12. D. Oepts, A.F.G. van der Meer and P.W. van Amersfoort, "The free-electron laser facility FELIX", *Infrared Phys. Technol.*, vol. 36, pp. 297-308, 1995.

13. K. W. Berryman and T.I. Smith, "A flexible far-infrared FEL user facility", *Nucl. Instrum. & Methods Phys. Res. A*, vol. 358, ABS 93, 1995.

14. E. Giovenale, F. Ciocci, A. Doria, G.P. Gallerano, M.F. Kimmit, G. Messina, P. Raimondi, A. Renieri and I. Spassovsky, "Upgrade on the ENEA compact FEL in the sub-mm region", *Nucl. Instrum. & Methods Phys. Res. A*, vol. 358, ABS 22, 1995.

15. J. M. Ortega et al., "CLIO - Collaboration for an infrared-laser at Orsay", *Nucl. Instrum. & Methods Phys. Res. A*, vol.285, pp 97-103, 1989.

16. Newnam, R.W. Warren, R.L. Sheffield, W.E. Stein, M.T. Lynch, J.S. Fraser, J.C. Goldstein, J.E. Sollid, T.A. Swann, J.M. Watson and C.A. Brau, "Optical-performance of the Los Alamos free-electron laser", *IEEE J. Quantum Electron.*, vol. 21, pp. 867-881, 1985.

17. G. Dattoli and A. Renieri, "Experimental and theoretical aspects of the free-electron laser", in *Laser Handbook Vol. 4*, edited by M. L. Stitch and M. Bass. North-Holland, Amsterdam, pp1-13, 1985.

18. T. C. Marshall, "Free-electron lasers", MacMillan, New York, 1985.

19. C. A. Brau, "Free-electron lasers", Academic Press, Boston, 1991.

20. J. B. Murphy and C. Pellegrini , "Introduction to the physics of the FEL" in *Laser Handbook Vol 6*, edited by W. B. Colson, C. Pellegrini and A .Renieri, North-Holland, Amsterdam, pp 9-70, 1990.

21. D. A. Jaroszynski, R. J. Bakker, A. F. G. van der Meer, D. Oepts and P.W. van Amersfoort, "Experimental observation of limit-cycle oscillations in a free-electron laser", *Phys. Rev. Lett.*, vol **70**, pp3412-3415, 1993.

22. R. J. Bakker, G. M. H. Knippels, A. F. G van der Meer, D. Oepts, and P. W. van Amersfoort, "Dynamic desynchronisation of a free-electron laser resonator", *Phys. Rev. E*, 48, R3256-R3258, 1993.

23. D. A. Jaroszynski, P. Chaix, N. Piovella, D. Oepts , G. M. H. Knippels and A. F. G. van der Meer, "Superradiance in a short-pulse free-electron laser oscillator", *Phys. Rev. Lett.*, vol **78**, pp1699-1702, 1997

24. R Bonifacio, B.W.J. McNeil and P. Pierini, "Superradiance in the high-gain free-electron laser", *Phys. Rev. A*, vol **40**, pp 4467-4475, 1989.

25. N. Piovella, P. Chaix, G. Shvets and D.A. Jaroszynski, "Analytical theory of free-electron laser oscillators", *Phys. Rev. E*, vol **52**, pp 5470-5486, 1995.

26. H. Al-Abawi, F. A. Hopf, G.T. Moore and M.O. Scully, "Coherent transients in the free-electron laser; laser lethargy and coherence brightening", *Opt. Commun.*, vol **30**, pp 235-238, 1979.

27. R. W. Warren, J. E. Sollid, D. W. Feldman, W. E. Stein, W. J. Johnson, A. H. Lumpkin and J. C. Goldstein, "Near-ideal lasing with a uniform wiggler", *Nucl. Instrum. & Methods Phys. Res. A*, vol. 285, pp1-10, 1989.

28. G. M. H. Knippels, "The short pulse free-electron laser: manipulation of the gain medium", Doctoral thesis, Free University of Amsterdam, 1996.

29. C. W. Rella, G. M. H. Knippels, D. V. Palanker, H. A. Schwettman, "Pulse shape measurements using differential optical gating of a picosecond free electron laser source with an unsynchronized femtosecond Ti:sapphire gate" *Opt. Commun.* vol **157**, pp. 335-342.

30. X. Yan, A.M. MacLeod, W.A. Gillespie, G.M.H.Knippels, M.J. van de Pol, A.F.G. van der Meer, C. W. Rella, "FEL pulse shape measurements with 100-fs temporal resolution using a 10-fs Ti:sapphire laser and differential optical gating", to be published in the proceedings of the 20th international free-electron laser conference, Williamsburg, VA., USA, 1998.

Chapter 2 A time-resolved electron spectrometer system

2.1 Introduction

This chapter documents the electron spectrometer system that was designed and constructed for the FELIX facility, although its modular nature makes it easily adaptable to other situations. The system permits software integration with other laboratory control systems, real-time calculation and graphical display of key beam parameters as well as the archiving of raw data, and has been used to provide insight into the operation of an FEL in the high slippage, short pulse regime. In particular, direct measurement of the extraction efficiency is possible from macropulse to macropulse. It has allowed a systematic study of efficiency as a function of wavelength and cavity desynchronisation to be undertaken; it has made it possible to produce programmed sweeps in wavelength, which have been used by molecular spectroscopists to excite target molecules through an anharmonic ladder of states; and it has provided further evidence for the recent observation of superradiance in an FEL oscillator

2.2 General considerations

Lasing was first achieved at the FELIX free-electron laser in the summer of 1991 [1]. FELIX was designed as a rapidly tuneable FEL user facility in the infrared, initially spanning a wavelength range of 8 μm to 80 μm. As such it required a stable, well-characterised electron beam with easily variable energy, which could be directed through two separate undulators to give the desired wavelength range. During the commissioning of FELIX, extensive measurements of the emittance and narrow energy spectrum of the electron beam under non-lasing conditions had been made and improvements in the energy stability of the linac greatly enhanced the performance of the FEL.

It became clear that several aspects of the proposed research programme required measurements of the electron energy spectrum over the 20 μs macropulse. Discussions with the FELIX team led to the specification of a spectrometer that would make measurements at 50 ns intervals over 32 energy channels spanning typically 4% in electron energy. It will be seen later in this thesis that the specified 4% energy spread was considerably smaller than the energy spreads encountered in practice due to the short pulse, effects and comparatively high extraction efficiencies encountered in the operation of FELIX.

A time-resolved measurement of the FEL electron energy spectrum benefits experiments in several ways. It allows a direct calculation of the mean energy extracted from the electron beam during the macropulse, which leads to a value for the efficiency of the FEL, an important operating parameter. Variation of the energy extraction during the macropulse in a prescribed way can then be produced by modifications in the FEL parameters [2]. It is also possible to dynamically vary the electron beam energy during the macropulse to produce rapid wavelength sweeps or wavelength steps [3], and this variation is monitored and calibrated using the electron spectrometer. More fundamentally, the ability

to probe the laser medium—the relativistic electron distribution—a few nanoseconds after its interaction with the stored radiation field, with good time and energy resolution, enhances our understanding of the microscopic laser interaction and ultimately improves our control over the dynamic behaviour of the laser.

Two basic classes of electron energy spectrum measurement are required of a practical system. First, the unbroadened (non-lasing) spectrum of the electron accelerator needs to be measured to verify the optimum injection conditions for the FEL, which for FELIX do not necessarily correspond to minimising the width of the electron energy spectrum. Second, the electron spectrum, shifted and broadened due to the lasing interaction, must be determined with adequate resolution in order to study the laser startup characteristics and the approach to saturation. Since lasing can be suppressed by detuning the optical cavity through movement of one of the mirrors, a single electron spectrometer following the undulator can perform both these measurements, and can therefore serve as a primary diagnostic for FEL performance. Additionally in FELIX, each undulator has a gap which can be opened to minimise the magnetic field on axis, effectively switching off its function.

The spectrometer itself comprises three main components: (1) a high-resolution 90° dipole magnet with rotated pole faces, in the focal plane of which lies (2) a multi-channel electron detector viewed by a variable optical system, and (3) a fast data acquisition system with the associated computer control and analysis software that allows data to be archived, or analysed and displayed in real-time in the FELIX control room. The modular nature of this spectrometer allows it to be used with both secondary electron emission detectors (SEMs) and detectors employing optical transition radiation (OTR). The compact 90° magnetic spectrometer (Figure 2.2) brings the electron beam at the output of the undulator of FEL–2 to a horizontal focus. The angled OTR radiator is viewed by a variable focal length optical system whose image plane contains the 35-element fast photodiode array (Hamamatsu S4114-35Q), of which 32 channels are used for spectral information. This arrangement allows the mapping between the electron focal spot and its optical image on the array to be adjusted to suit the experimental conditions, and permits the spectrometer resolution to be fully exploited over a range of FEL operating conditions. The design of the spectrometer is dominated by the limitations of space within the FEL cavity, making the electron-optical mode chosen a compromise between compactness and beam control.

2.2.1 Secondary emission monitors

Both 30-channel and 96-channel secondary emission monitors are in use at FELIX, consisting of 40 μm thick tungsten foils, having a height of 100 mm, a width of 0.7 mm and a centre-to centre spacing of 1.4 mm, which may be angled along a spectrometer focal plane or used as a simple beam profile monitor in a drift space. The foils are tensioned on a stainless steel frame and electrically isolated using machined ceramic supports, to which they are bonded using high-temperature epoxy adhesive. A multiple feedthrough of machined ceramic is used to lead the free ends of the foils out of the vacuum system to the preamplifier electronics. The secondary emission collection efficiency is enhanced by placing a rectangular aluminium frame collector at 1 kV positive potential about 20 mm downstream of

the foil plane. Two of these detectors are presently installed in the FELIX beam lines (SEM1 and SEM2 in Figure 1.8) beyond the switching dipoles in the beam distribution system, where they are used as spectrum monitors to facilitate the setting up of the electron beam delivered by the linac. A 4x32-channel multiplexer has been built to allow the digitisation electronics and data acquisition software to be used either with these SEMs or with the OTR monitor.

Secondary emission detectors have the advantage that under appropriate conditions [6] the secondary emission coefficient of thin foils or wires is very stable and displays good linearity up to high incident current densities, and thus no saturation effects are observed. The coefficient of thin foils is typically 1% – 2% per emitting surface, leading to relatively large signal levels, which in turn permit fairly narrow detecting elements and thus respectable spatial resolution. Secondary emission operates over a wide range of electron energies, and the direct measurement of charge loss from the foils allows the detector to be adapted to the angled and potentially curved focal surfaces typical of high-resolution electron spectrometers—an important practical advantage when large energy spreads must be accommodated at high resolution.

On the other hand, secondary emission detectors constitute at least a partially intercepting monitor, leading to foil heating, potentially significant beam loss due to multiple scattering, and the attendant radiation damage and background. For inadvertently focussed high incident fluxes, foil temperatures could exceed 2000 K, leading to significant thermionic emission, although this is unlikely in normal operation. Nevertheless, the detector elements must be protected against thermal damage and deformation, while thermal shock effects due to the pulsed nature of the energy deposited from the beam may also cause problems. Recent developments [7] with SEM detectors based on very thin metallic layers deposited on an insulating substrate may go some way towards compensating for these defects. Finally, due to the relatively large physical size of the foils in our SEM detectors and the (necessarily) unscreened connections to the outside of the vacuum chamber, fast response may be compromised due to capacitive effects, resulting in cross-talk between channels and consequent calibration errors.

2.2.2   Optical transition radiation detectors

Transition radiation is emitted when a high-energy charged particle traverses the interface between two regions of significantly different dielectric constant [8], and has a spectrum that can range from microwaves to X-rays depending on the energy of the traversing particle. It has been extensively used in recent years as a means of detecting both proton [9] and electron [10] beams. The production mechanism of transition radiation has been adequately reviewed by several authors [11,12] and therefore only the briefest of discussions pertinent to the mode of use in our application is given here. As shown in Figure 2.1(a) radiation is produced in both forward and backward pointing cones, shown as twin lobes in the diagram. The opening angle of each of the lobes is $\theta = \dfrac{2}{\gamma}$ where γ is the Lorentz

factor. For $\gamma > 100$, the lobe intensity maxima are equal to within a few percent and the intensity and angular distribution are both strong functions of energy. A characteristic of backward transition radiation at high γ is that the radiation generated at the leading interface is centred on the "direction of specular reflection" as defined by the Fresnel coefficients for the interface. For a radiator at 45° to the electron beam, the backward transition radiation therefore appears at 90° to the electron beam direction as in Figure 2.1(b), and the dipole radiation field is radially polarised with the electric vector lying in the plane of observation. The dependence of intensity on wavelength is in general quite complex, and within a relatively narrow spectral range it is dominated by the spectral properties of the radiator. Normally aluminium is chosen, which exhibits an approximately λ^{-2} dependence.

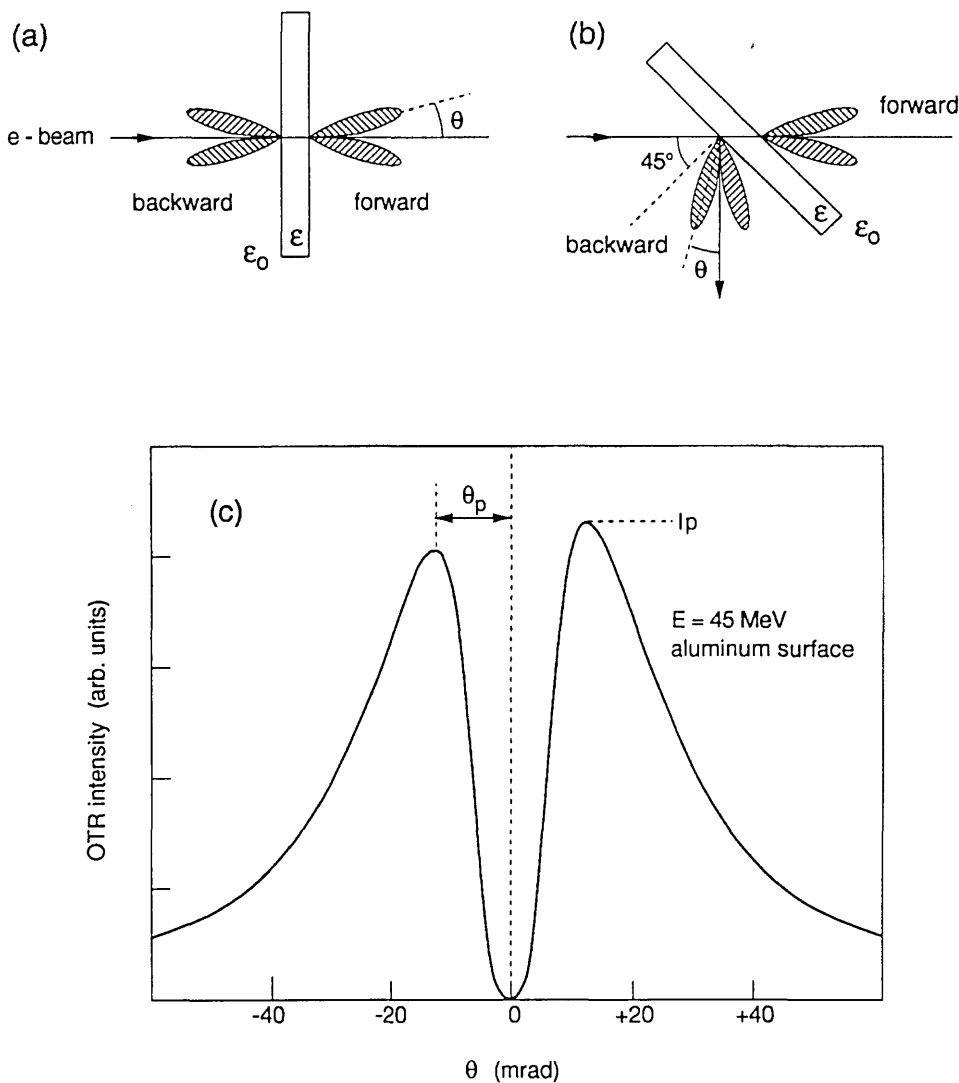**Figure 2.1** *Intensity and angular distribution of optical transition radiation at high γ. (a) and (b) show the forward and backward radiation patterns at normal and oblique angles of incidence on an aluminium foil. The backward angular distribution shown in (c) is a function of the emission angle θ. The angle of peak emission is $\theta_p = 1/\gamma$, and the peak intensity is $I_p \propto \gamma^2$.*

26

The system described in this chapter is based on an aluminium radiator and the measurements of transition radiation in the visible part of the spectrum, generally referred to as optical transition radiation, or OTR. In addition, because OTR is an interface emission process—essentially a kind of differential Cerenkov effect—it offers the possibility of using very thin radiators which need only cause minimum disturbance to the electron beam, an order of magnitude less than typical secondary emission foils or view-screens with the same efficiency. For the same reason, OTR avoids the effects of thickness and phosphor grain size which limit conventional view screen techniques, or the radiator thickness and internal reflection problems in Cerenkov systems based on, for example, quartz view-screens. OTR imaging is capable of high spatial resolution, and time resolution in the sub-picosecond domain is possible.

2.3 System requirements

The FEL physics requirements at FELIX require that the electron spectrometer have an energy resolution of 0.2% coupled with a time resolution of 50 ns in each of 32 energy channels. The electron spectrum monitor is used to provide measurements of electron beam profile and electron energy spectrum in FELs. The beam profile or spectrum is displayed on a graphics screen in the control room 40 m away from the electron spectrometer, and is also available via a LAN at other workstations in the laboratory. Data may also be transferred over the LAN to other computers for archiving.

2.4 Design philosophy

Several other European FEL laboratories expressed an interest in similar spectrometers, so the system is designed so that it may be customised to meet the specific needs of the user laboratory; it is capable of expansion to take measurements from more than one detector simultaneously or sequentially, allowing the comparison of spectra from electron and optical detectors within a single laser pulse. This is achieved by making the system highly modular: different detectors—at present either SEM or OTR— are accommodated by means of a relatively simple change in the preamplifier electronics, and the digitising system can be configured with 8, 16, 24 or 32 channels and expansion to 64 channels has been provided for. The computing hardware and software are also modular and comprise a VME-based Motorola 68020 microcomputer running the OS-9 operating system in which hardware independence is ensured by interfacing to the electronic subsystems by means of a parallel input/output (IO) card and a custom-written OS-9 device driver. This also allows the data acquisition and display software to run in a multi-tasking environment, where tasks other than the data acquisition, data processing and user interface processes associated with the spectrometer can execute concurrently. Evidence of the robustness of this approach is that the computer system and associated electronics, the prototypes of which were first installed in the summer of 1992, before the spectrometer magnet had been designed, have evolved, for reasons unconnected with the spectrometer, through two generations of microprocessor board and now operates with a 60 MHz Motorola 68060 processor and a different parallel IO card and has been in operation almost daily since its installation. Developments at FELIX

make it likely that the software will be reconfigured for an Intel Pentium-based system running the Linux operating system in the near future.

2.5 Specification and design

The system specification is the result of a compromise between the need to produce a low cost system and the requirement to study variations in the electron energy spectrum with sufficient resolution in amplitude and in time. The sampling interval of 50 ns allows features with a time scale of 1 μs to be readily observed in detail. The eight-bit resolution is adequate for current experiments: however if greater dynamic range is required in the future, the cost-effective upgrade path would be either to design variable gain preamplifiers or to use optical techniques to provide variable attenuation of the highly polarised optical transition radiation rather than to move to a 12-bit digitising system.

The system is capable of making measurements of the energy spectrum of the beam within a nominal 4% energy bite, at intervals of 50 ns during beam pulses of up to 20 μs in duration. It is modular and capable of expansion. Measurements are made with 8-bit resolution on all channels. The following display options are provided, and examples of the graphical output which are discussed in a later section, are given in Figure 2.5:

1. a histogram displaying the time-averaged energy distribution within a single pulse, which can be updated on the screen every pulse for repetition frequencies up to 10 Hz, or produced on demand;

2. graphs of energy against time for selected channels in a single pulse as either two dimensional or three dimensional graphs; and

3. graphs of intensity, average energy and variation in energy against time within a single pulse.

Data can also be displayed in tabular form, as hard copy of the graphics output options, or as a file on the local computer system. Data may be made available on the laboratory LAN, concurrently with any of the preceding options, for processing and display on a variety of workstations.

2.5.1 The spectrometer chamber and magnet

An overall design resolution of 0.18% in electron momentum was chosen, coupled with a nominal energy bite of 4% across the 32-channel detector, which, for the dimensions of the chosen detector, yields a focal-plane dispersion of 8 mm/%. Spectral widths of greater or less than 4% are accommodated by zoom optics, giving a factor of 2 in either direction. The use of parallel-to-point electron optics in the spectrometer horizontal plane helps overcome the severe space limitations, and exploits the focussing properties of the undulator in this plane: the FELIX undulator oscillates the beam in the vertical plane, and therefore the horizontal plane is the focusing plane. The horizontal object location for the spectrometer is therefore effectively at infinity, and the moderate beam divergence (~1.0 mrad) at the exit of the undulator allows adequate resolution to be obtained for this optical mode. The object for the spectrometer in the vertical plane is effectively at the undulator midplane, where the divergence is similar under conditions of good matching. As well as defining the focusing and

dispersive properties, the rotated pole edges must also control the vertical beam transport, since there is no space for additional quadrupole elements and essentially all of the beam current must be delivered to the beam dump following the spectrometer. Radiation background and damage to the equipment are thus minimised. The spectrometer vacuum chamber is equipped with additional optical viewports to aid laser and optical alignment of the whole system

The spectrometer layout is shown in Figure 2.2. The dipole has a bend radius of 230 mm, a bend angle of 90°, and pole edge rotations of $\beta_1 = 38°$ and $\beta_2 = 32°$. Despite the small bend radius, the second-order aberrations prove to be almost negligible, and good resolution can be maintained over a wide range of input conditions. The pole gap is chosen at 50 mm to reduce cavity diffraction losses at long wavelengths and the dipole is equipped with chamfered pole-edge profiles (in the Rogowski approximation) and re-entrant field clamps to guarantee precise control over the fringe fields and stability of the energy calibration. The fringe field simulations were performed using the program suite EMP/POISSON [5], and the spectrometer dipole was manufactured by Goudsmit Magnetic Systems, Aalst-Waalre, The Netherlands.

Careful measurements of the dipole field distributions, performed using equipment at the Accelerator Laboratory of Eindhoven University of Technology, were used to adjust the positions of the effective field boundaries (EFBs) at the dipole entrance and exit by movement of the clamp noses. After these adjustments, the EFBs varied by less than 0.7 mm over the complete excitation range of the dipole (0.1 T – 0.9 T). The relative homogeneity of the uniform field region was measured with a digitally controlled Hall probe (Siemens SBV 613) to be $\pm 3 \times 10^{-4}$. A typical plot of the field measurements is shown in Figure 2.3. The EFB is calculated by evaluating the integral $\dfrac{1}{B_0} \int_{r_0}^{\infty} B(r)dr$, in which the path of integration is perpendicular to the pole-face and extends from a point between the pole faces, where the field is uniform and of magnitude B_0, to a point outside the pole faces where the magnetic field is negligible—i.e. effectively to infinity.
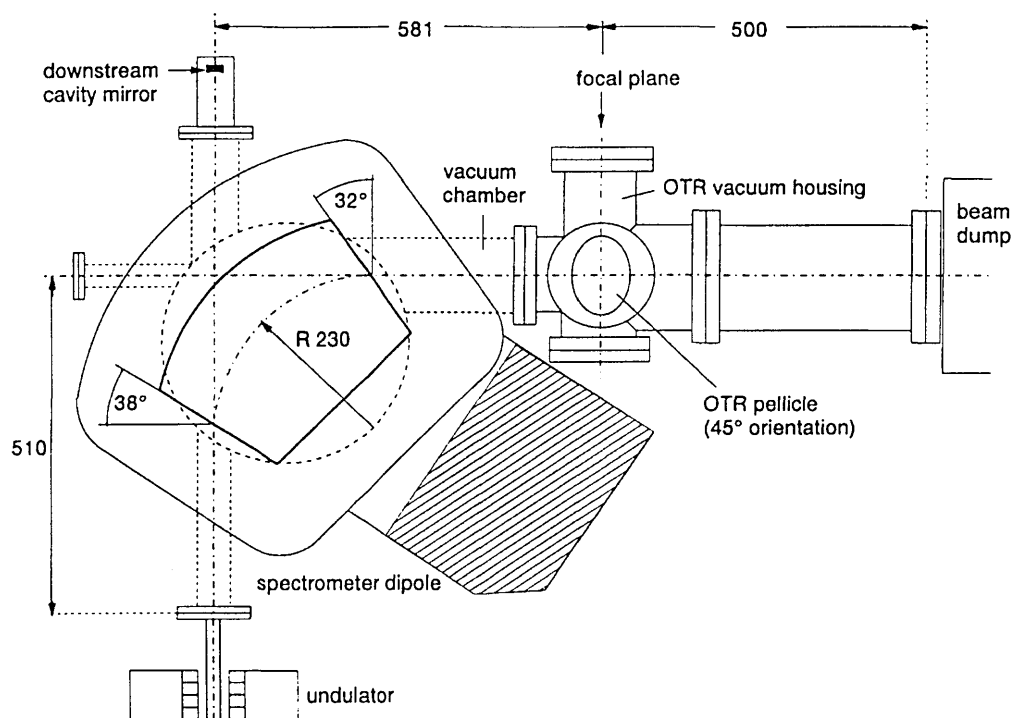
Figure 2.2 *A drawing of the spectrometer bending magnet at the downstream end of the FEL-2 undulator. The vacuum housing of the OTR pellicle is between the bend and the dump. The optical system lies along the vertical axis through the centre of the pellicle. Initially the OTR was directed downwards to the optics in a floor mounted tower. In a subsequent modification, the OTR foil was rotated so that the radiation is now directed upwards and the optical tower is mounted on the magnet support.*
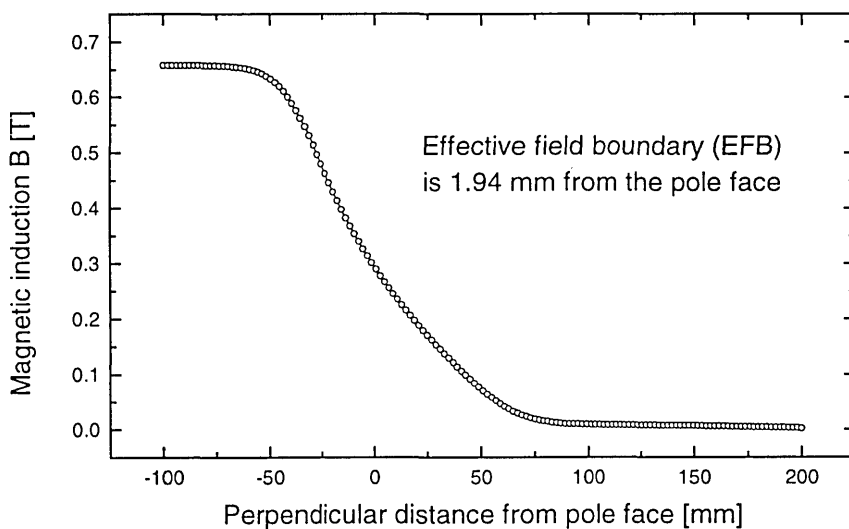
Figure 2.3 *A typical graph showing the variation in magnetic induction as a function of distance from the pole face. Measurements were made with a digitally positioned Hall probe (Siemens SBV 613)*

2.5.2 The OTR and optical system

The optical system is designed so that the nominal 4% energy bite would span the 32 channels of the detector array, which are at a pitch of 1 mm, under unity magnification and the zoom optics employed—with a magnification range of 0.5 to 2—can accommodate spectral widths ranging from the bare linac spectrum, of the order of 1%, to those corresponding to the severely broadened spectra acquired under high efficiency energy extraction. The latter can be considerably in excess of 10% full width, and are normally acquired using several overlapping settings of the spectrometer field. Single acquisition spectra are limited to around 6% due to the finite field of view of the zoom optics. Beyond this vignetting becomes a problem, making accurate calibration of composite spectra more troublesome. Furthermore, it proved impossible to take composite spectra for the broadest energy spreads observable because of radiation caused by the beam striking the vacuum chamber being picked up directly by the detector. The parameters chosen were more than adequate to resolve many features of interest within the 10 μs FELIX macropulse. In chapter 3, modifications to the optical system and vacuum chamber are described that allow spectra with widths of up to 7% to be acquired in a single shot without vignetting, and ensure that the broadest spectra do not cause the electron beam to strike the chamber.

The OTR radiator is either a thin pellicle of aluminised kapton film—typically 3-5 μm kapton with a 40 nm coating of aluminium (National Photocolor Corporation)—or simply a 10 μm thick pure aluminium foil. The film or foil is stretched over a 120 mm inside diameter machined aluminium holder, and the radiator is mounted at an angle of 45° to the horizontal, so that the backward transition radiation propagates vertically into the optical system. More than 90% of the total OTR intensity at 45 MeV electron energy lies within ±5° of the emission axis, and this is imaged on the fast photodiode array (Hamamatsu S4114-35Q) using an optical system comprising a large aperture objective lens (ϕ80 mm, f=310 mm) followed by a zoom lens (ϕ55 mm, f=75 – 300 mm), providing magnifications in the range 0.25 – 1.00. A beamsplitter allows the OTR to be simultaneously viewed with a CCD camera for direct observation of the electron distribution in the spectrometer focal plane. Provision was also made for an ultra-thin "blocking" pellicle to be inserted immediately upstream of the OTR radiator, in order to prevent optical radiation generated upstream (such as synchrotron radiation or undulator radiation) from creating a background to the OTR. This additional pellicle has so far proved unnecessary.

2.5.3 Secondary emission monitors

No new SEM detectors were specified or designed for FELIX. The two SEM devices that are in use are described in section 2.2.1 and are in fact those developed for the UK FEL project [13,14].

2.5.4 Data acquisition system structure and hardware

An overview of the measurement system is given in Figure 2.4. Apart from the detector, the main functional units are the preamplifier, the digitiser, and the VME bus MC68040-based single-board computer (now upgraded to a MC68060), including an intelligent interface card with an independent MC68000 cpu. Since there are 32 identical channels in the preamplifier and digitising units,

considerable effort was made to simplify their design and to use a small number of cheap and readily available components. It was decided to use a MC68040-based single-board computer on a VME bus system running the OS-9 operating system in order to provide real-time response while running multi-tasking software allowing the same computer system to acquire data, analyse and display these data while at the same time monitoring other aspects of the performance of the FEL. Detailed descriptions of the electronics and software are given in the appendix in section 2.8
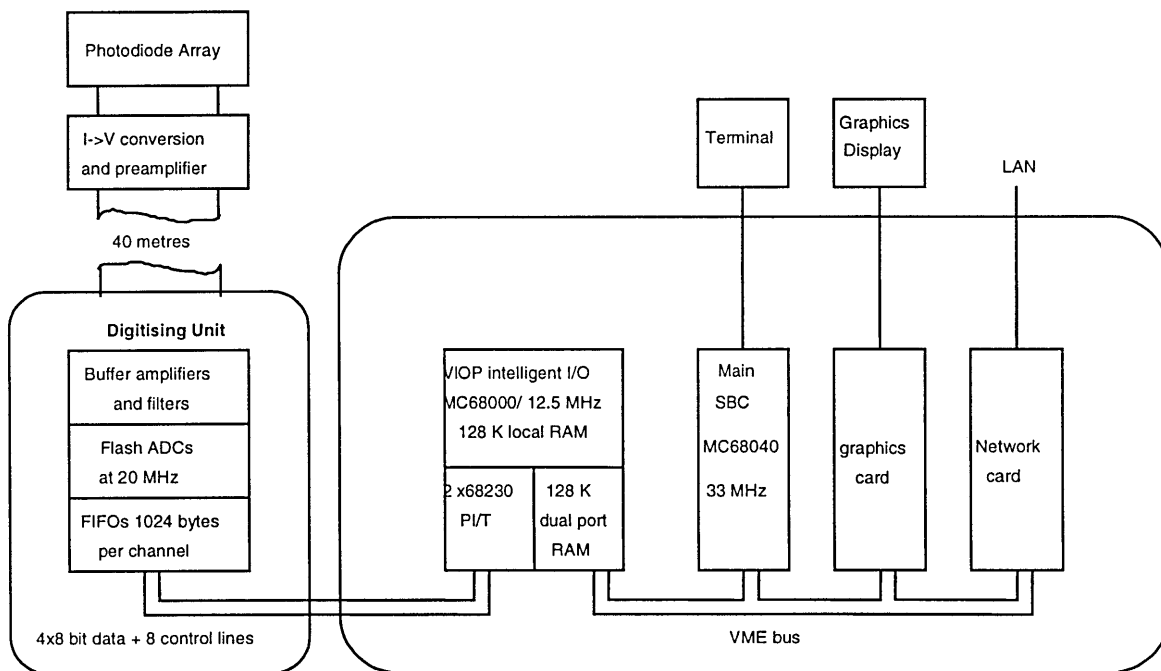
Figure 2.4 *An overview of the measurement system.*

2.6   A critical evaluation of the system

The system was installed in the FEL–2 beam line in December 1993, and the vacuum chamber was modified in July 1994 to increase the system energy acceptance. This was necessary because the electron spectral widths measured under conditions of large slippage were much larger than anticipated, and the resulting dispersed beam suffered significant loss within the original spectrometer vacuum system. Since mid 1994 the spectrometer has been used in a number of experiments associated with the measurements of dynamic energy extraction in the FEL during fixed-wavelength lasing, studies of ultrafast wavelength scans for use in molecular spectroscopy [3], and step-tapered undulator experiments to explore the potential for two-colour operation of the FEL [2].

File: Date: 17-07-94
γ=72   λ=30µm   -ΔL=1.7λ   K=1.93
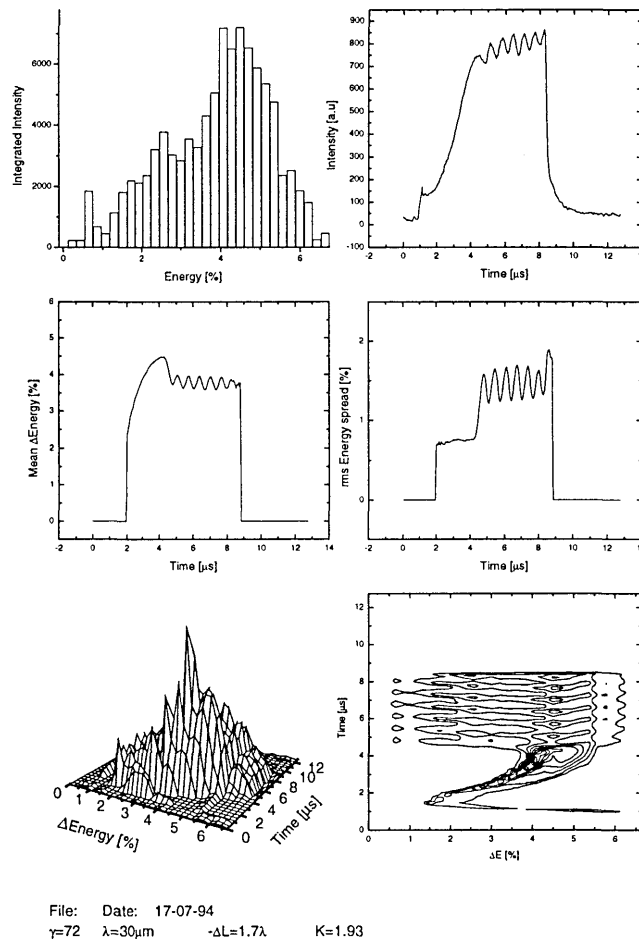
Figure 2.5 *Typical display available from the electron spectrometer system. The three-dimensional surface plot at the bottom left-hand corner may be re-oriented and scaled by the operator to bring out details of the spectrum. A contour plot of this surface is shown at the bottom right. The centre row shows the oscillations in energy and width, characteristic of the limit cycle mode of operation of the FEL. Note that the initial transient, due to beam loading, lasts about 3 µs and that the spectrum broadens during lasing. The top left shows a time-integrated spectrum, most useful for operator adjustment of the FEL. The top right shows a plot of the electron beam intensity as a function of time, important in establishing that what is detected is due to transition radiation, not due to electrons striking the vacuum chamber.*

Typical displays available from the system are presented in Figure 2.5 which presents data taken when lasing at λ=30 µm with a cavity desynchronism of -1.7λ. The integrated profile display (top left) is of great use to the FEL operator in making initial adjustments to the electron beam: the visual display

allows the operator to adjust the beam so that its integrated spectrum has a pre-determined shape allowing particular beam characteristics to be set up rapidly. The 3-D display (bottom left), while having an impressive appearance has not proved particularly useful in practice, although if time is taken to select a suitable viewpoint this display can be used to exhibit interesting features clearly. Of far greater use has been the contour display of the same information (bottom right), which is of course suitably coloured in the display available to the operator. As is evident from the contour plot, the electron beam energy starts off in a relatively narrow range for the first 2-3 μs before broadening considerably as the FEL begins to lase.

Other derived measurements are of interest and are also shown in Figure 2.5. The broadening of the spectrum described in the previous paragraph is also clearly shown in the plot of r.m.s. spectral width, against time (middle right). The variation of the mean energy with time (middle left) has been confirmed by independent measurements using a button monitor and found to be in good agreement: the initial transient in this plot is due to beam loading effects. Notice also that the onset of lasing, which occurs just after 4 μs in the graphs in Figure 2.5, is indicated clearly in three of the time resolved displays: by the sudden drop in mean energy in the mean energy/time plot, a corresponding broadening of the spectrum in the contour plot, and an increase in spectral width in the r.m.s. spectral width/time plot. These plots also show clearly that at this wavelength and detuning, the extreme slippage between the optical and electron micropulses results in a stable modulation of the FEL output—the so-called limit-cycle oscillation [15]. Note that the electron spectrum during lasing has a width of around 5%; under some conditions it has been measured to be greater than 15%, requiring the accumulation of data at several spectrometer fields.

2.7　References

1.　P. W. van Amersfoort et al, "First lasing with FELIX" *Nucl. Instr. and Meth.* A **318** pp. 42-46 (1992).

2.　D. A. Jaroszynski, R. Prazeres, F. Glotin, J. M. Ortega, D. Oepts, A. F G. van der Meer, G. M. H. Knippels and P. W. van Amersfoort, "Free-electron laser efficiency enhancement, gain enhancement and spectral control using a step-tapered undulator." *Phys. Rev Lett.* **74**, 2224 (1995).

3.　G. M. H. Knippels, A. F. G. van der Meer, R. F. X. A. M. Mols, D. Oepts, P. W. van Amersfoort, A. M. MacLeod and W. A. Gillespie, "Feasibility of a far-infrared free-electron laser as a voltage-controlled optical oscillator", *Infrared Phys. & Tech.*, **37**, pp 285-294, 1996.

4.　W. A. Gillespie, A. M. MacLeod, P.F. Martin A. F. G. van der Meer, and P. W. van Amersfoort "Time-resolved electron spectrum diagnostics for a free-electron laser", Rev. *Sci. Instrum.*, **67** (3) pp 641-648 (1996).

5.　EMP/POISSON code, version 2, Los Alamos National Laboratory, NM 87545.

6.　L Malter, *Phys. Rev.* **49**, 478 (1936).

7.　Ph. Guimbal – private communication.

8.　I. Frank and J. Ginsburg, *J. Phys. USSR*, **9**, 353 (1945).

9. J. Bosser, J. Mann, G. Feroli and L. Wartski, *Nucl. Instr. and Meth*, A **238**, 45 (1985)

10. X. K. Maruyama, R. B. Fiorito and D. W. Rule, *Nucl. Instr. and Meth*, A **272**, 237 (1988)

11. D. W. Rule, *Nucl. Instr. and Meth*, B **24/25**, 901 (1987)

12. A. H. Lumpkin, R. B. Feldman, D. W. Feldman, S. A. Apgar, B. E. Charlson, R. B. Fiorito and D. W. Rule, *Nucl. Instr. and Meth*, A **285**, 343 (1989)

13. C.R. Pidgeon et al., "The UK Free-electron laser: optical and electron beam diagnostics", *IEEE Journal of Quantum Electronics*, QE-21 (7) 1083-1088 (1985)

14. P.F. Martin, W. A. Gillespie and M. G. Kelliher, "An electron spectrum and profile monitor for the UK free electron laser", *Nucl. Instr. and Meth*, A **240**, 445-451 (1985)

15. D. A. Jaroszynski, R. J. Bakker, A. F. G. van der Meer, D. Oepts and P. W. van Amersfoort, *Phys. Rev. Lett.*, **70**, 3412 (1993)

2.8 Appendix

This appendix provides a detailed description of the electronics and computer hardware and software which were designed and implemented as part of the electron spectrometer system.

2.8.1 Hardware

The preamplifier unit consists of a set of four 8-channel preamplifier cards which convert the photodiode array current outputs to voltage signals and drive the 50 Ω cable links to the digitising units. The output voltage range of 0 - 1.6 V from the preamplifier cards was chosen to ensure that the signal to noise ratio on the cable links to the digitising unit was suitably large. An 8-channel card fits in to a double-height Eurocard frame located close to the detectors within the beam vault. As this area experiences a significant amount of radiation during the operation of the FEL, the remainder of the system is located 40 m away in the control room. The preamplifier cards have, however, been operating continuously for over 4 years and show no signs of radiation damage.

Each preamplifier channel, as shown in Figure 2.6, comprises two Analog Devices AD844 current feedback amplifiers, U_1 and U_2, the first providing the current-to-voltage conversion and the second providing the necessary voltage gain. Some variation in gain, to suit different detectors, may be provided by an appropriate choice of the feedback resistors R_1 and R_3. Cross-talk is minimised by using separate voltage regulators on the power supply lines for each channel.

The digitising unit provides each channel with an input buffer, an anti-aliasing filter, a flash analogue-to-digital converter (ADC) and first-in-first-out buffer (FIFO). The input buffer terminates the 50 Ω line and provides the level shifting required for the ADC. The filter is a 2-pole Butterworth filter with a -3 dB point at 5 MHz. The 8-bit flash ADC provides 20 MHz sampling and the data in each channel is stored in a FIFO that has a capacity of 1024 bytes. The digitising unit comprises a set of four 8-channel digitising cards and a single timer card which provides the clock signals for the ADCs and FIFOs as well as providing buffers which allow the data to be transferred to the VME system by means of the intelligent interface card. The digitising and timer cards are housed in a standard double-height Eurocard frame fitted with an uncommitted backplane which provides a 32-bit data bus linking the four digitising cards and the timer card, and carries clock, read and write signals to the ADCs and the FIFOs. A block diagram of an 8-channel digitising card and connections to the timer card is given in Figure 2.7
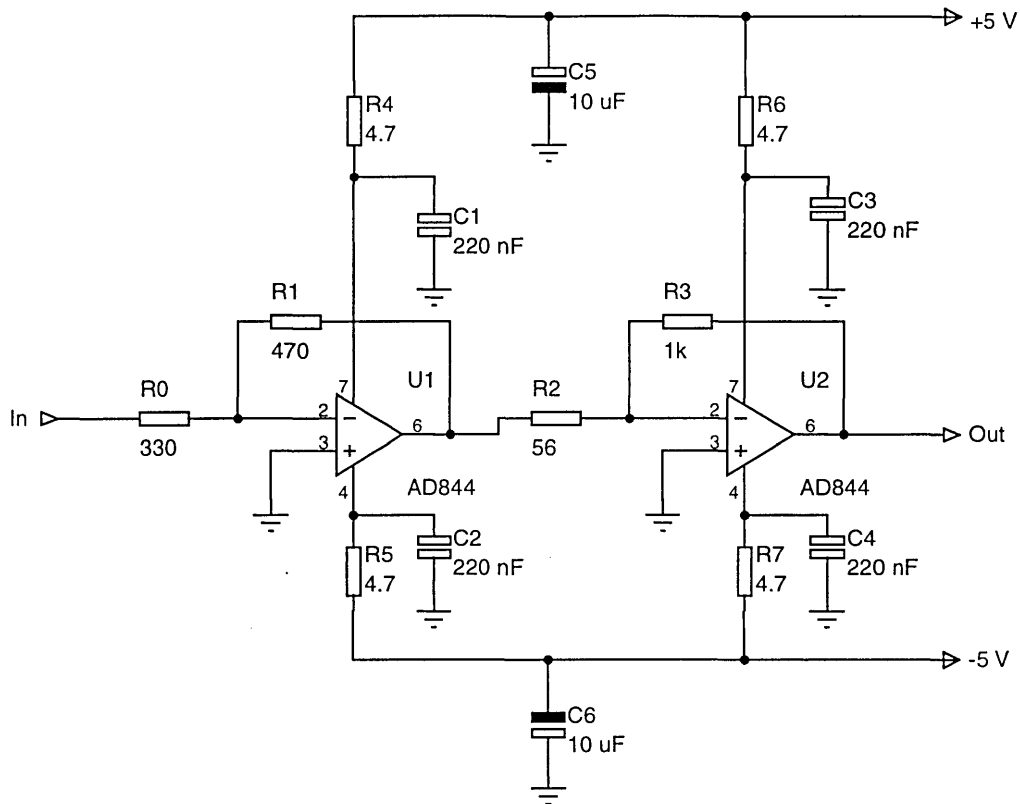
Figure 2.6 *A single channel pre-amplifier*

The intelligent I/O card is a VIOP digital output module from PEP Modular Computers which is controlled by a dedicated Motorola MC68000 microprocessor running at 12.5 MHz. It provides two MC68230 parallel interface/timers (PI/Ts), each of which provides two 8-bit ports and four handshake lines, the facility to both generate interrupts on the VME bus as well as receive interrupts from the main VME computer card, and 256 K of dual-ported SRAM in two banks of 128 K, one bank being 'visible' on the VME bus when the VIOP processor is stopped, the other being 'visible' when it is running. The software that runs on the VIOP is loaded by a process running on the main computer card into the dual-port RAM area when the VIOP processor is stopped. When the microprocessor on the VIOP is started, the second dual-port RAM bank is used as a buffer between processes running on the VIOP microprocessor and on the microprocessor of the main VME computer card.

The VIOP controls the operation of the digitising unit and the transfer of data from the FIFO buffers into dual-port RAM located on the VIOP card. Each 8-channel digitiser card is connected to its own dedicated 8-bit port. An important feature of the VIOP card is the ability to fetch 32-bits of data from four 8-bit ports simultaneously in a single 32-bit read cycle. The calculation of the integrated profile of a single beam pulse is performed by the processor on the VIOP. This profile consists of an integration over time of the signal on each input channel. The main computer card is allowed to gain access to the raw data and the integrated profile using the VME bus. This data is held in the dual-port RAM on the VIOP card and is only accessed by the main computer card on receipt of an interrupt from the VIOP unit.

37
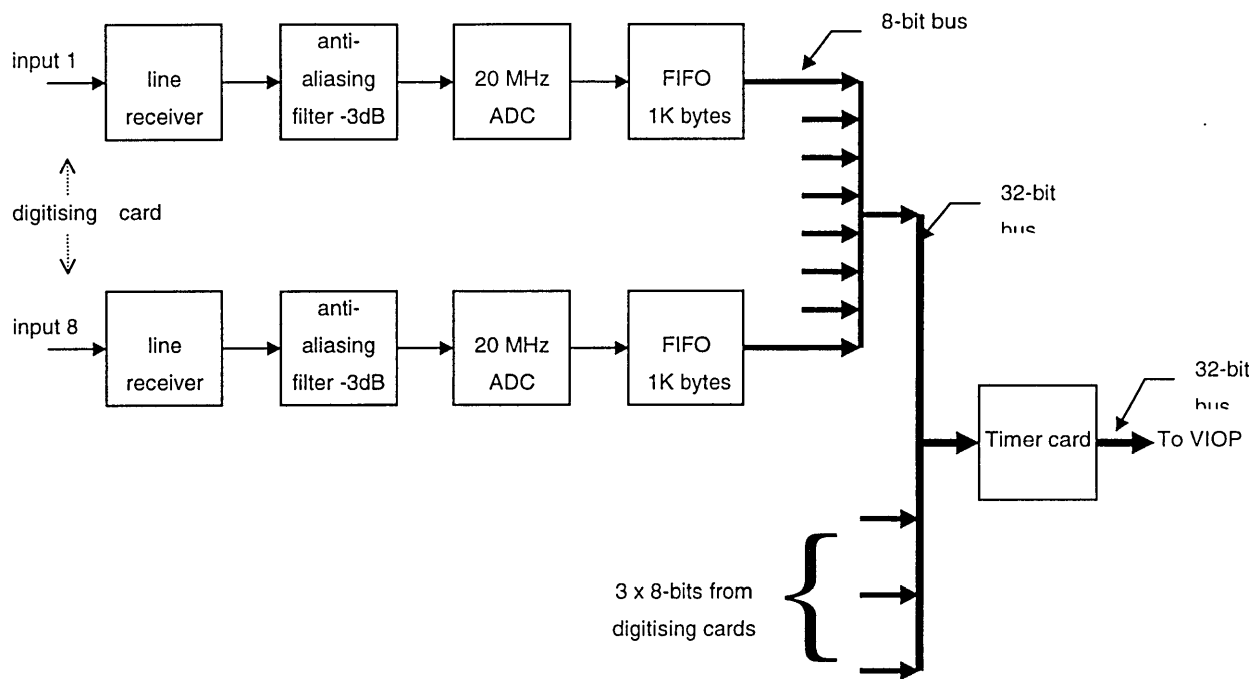
Figure 2.7 *Block diagram of a single 8-channel digitiser card and connections to the timer card and VIOP unit. FIFO select and logic control have been omitted for clarity.*

2.8.2 Software

An overview of the system software is shown in Figure 2.8 with additional detail in Figure 2.9. The software processes associated with the system run on two microprocessors: the MC68000 in the VIOP unit and the MC68040 on the main VME system computer card. As with the design of the hardware subsystems, considerable emphasis was placed on a modular approach to the design of the software and great importance was attached to subsystem specification and testing throughout the development process. The decision to separate the functionality of the software modules so clearly—data capture, data transfer and data presentation are handled by three distinct processes—has contributed greatly to the reliability of the system. Software maintenance since installation has been confined entirely to enhancements made to the data-presentation and operator interface process, *opif*. In addition the software has been successfully ported to a second VME system when faults developed on the hard disk and processor board of the original system and eventually to a third system, when the processing power required to be increased to accommodate the demands of other software running on the same VME system.
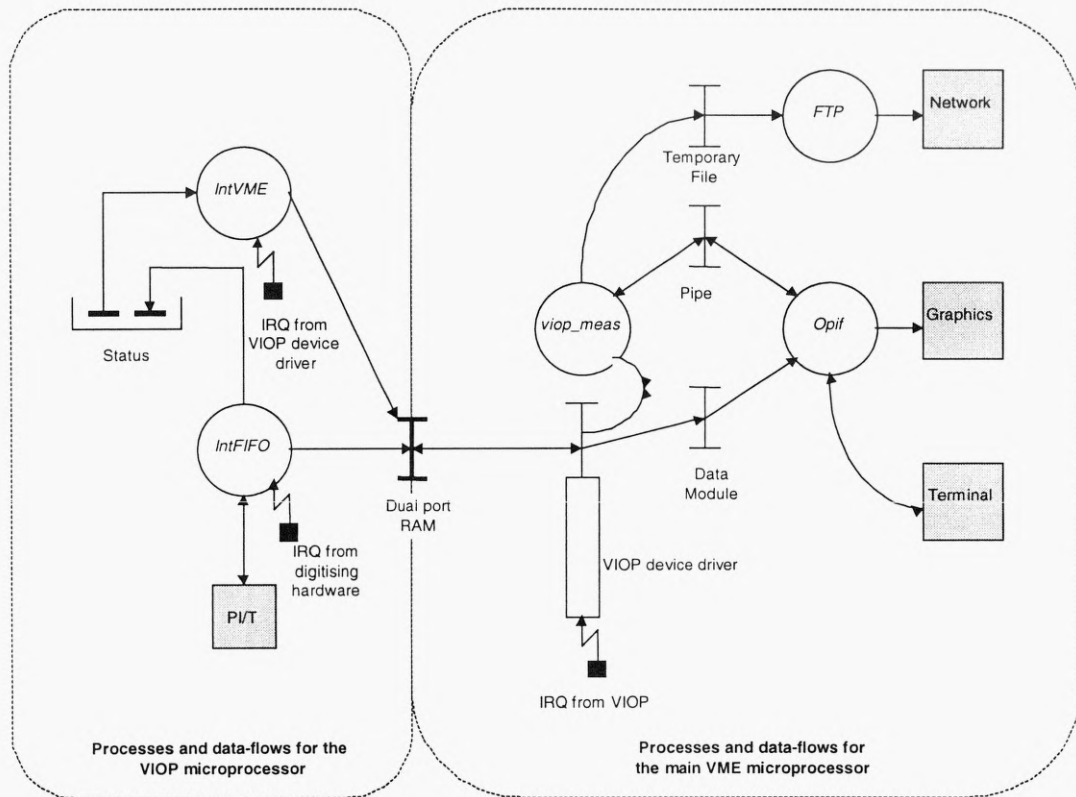
Figure 2.8 *Overview of the system software showing processes, main data flows and interaction with external hardware. Note that IntVME and IntFIFO run on the VIOP MC68000 cpu whereas the other processes run on the main VME MC68040/60 processor.*

The software running on the cpu of the VIOP card is interrupt driven: the main process is activated by an interrupt generated by the main VME computer card. This process then interacts with the digitising hardware, awaits data acquisition, transfers the data from the FIFOs in the digitiser cards into dual-port RAM, performs some signal processing if required—e.g. the calculation of the integrated profile—and finally generates an interrupt on the VME bus to indicate that data is available.

The main processor on the VME bus was a MC68040 (is now a MC68060) running OS-9, Microware's real-time multitasking operating system. There are two processes here: *viop_meas*, which interacts with the VIOP card, commissioning measurements, signalling their completion to the operator interface process, and handling background archiving tasks which make the acquired data available to all users on the laboratory LAN; and *opif*, the operator interface process which handles the user interface and performs the main data processing and display functions. Interaction with the VIOP module is handled in a hardware independent manner through the use of an OS-9 device driver which allows the VIOP to be integrated into the OS-9 input/output system.
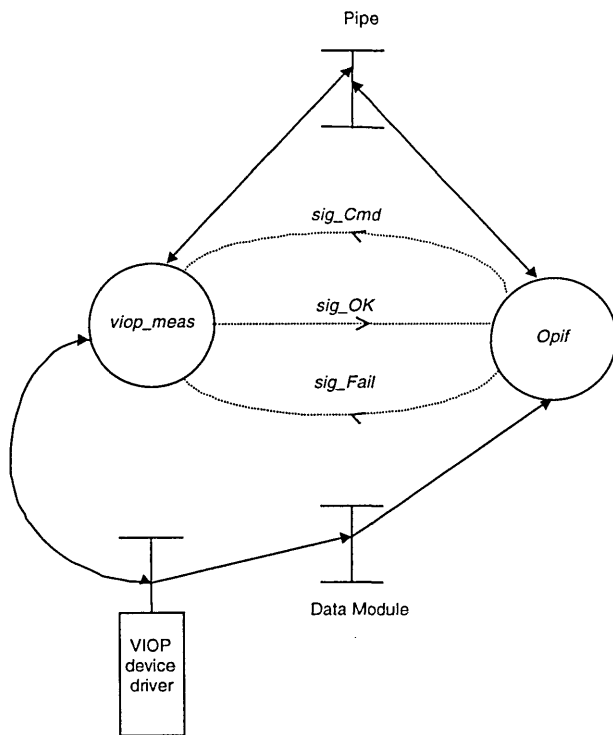
Figure 2.9 *Detail of the signals and data flows between the processes **opif** and **viop_meas***
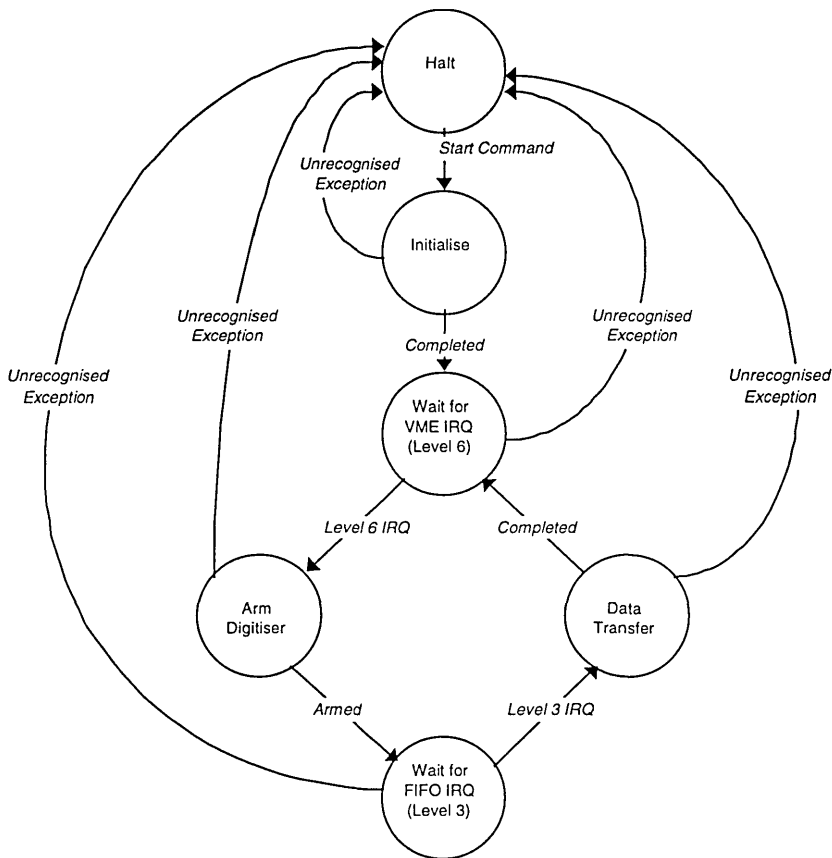
Figure 2.10 *State transition diagram for the VIOP module. Note that an external or VME bus reset condition is handled as an unrecognised exception.*

The process *viop_meas* is concerned with handling the hardware by means of the device driver, obtaining the data and, if required, making a copy of the data available to all users on the laboratory LAN. This activity was made a separate process principally to make it possible for the most recent data

to continue to be available on the LAN while allowing the FEL operator, who interacts only with the process *opif*, to be able to process and display data taken earlier.

2.8.2.1 Software for the VIOP module.

The software which runs on the MC68000 processor on the VIOP module is implemented entirely in MC68000 assembly language and has been deliberately kept simple. This fact, coupled with the clear separation of the functionality of the software modules, has helped to ensure the reliability of the system. It was possible at an early stage in the development of the system to test the VIOP software thoroughly and independently of the other system components. Integration with the OS-9 processes is handled by the device driver, described later in this article, and this too was tested in conjunction with the VIOP card but independently of the remainder of the system.

The code was developed under OS-9 on the main computer card and assembled to a binary file which can then be loaded into the dual-port RAM area when the VIOP MC68000 processor is halted. The code could also have been placed in an EPROM so that it is permanently installed on the VIOP card but the present system initialisation procedure downloads the code, as described above, before starting the VIOP cpu. Since no operating system was available for the VIOP card a skeleton was written, to intercept all interrupts and report any errors by writing to a status area in the dual-port RAM. This skeleton was useful in developing and debugging the remainder of the code which consists of a short initialisation routine and two interrupt service routines (ISRs), *IntVME* and *IntFIFO*, which perform the main tasks of the system. A state transition diagram for the VIOP software is shown in Figure 2.10.

On power-up, the processor is in the halted state and is activated by a run command on the VME bus. It will return to the halted state whenever any unexpected exception—an interrupt, trap or external reset signal—is encountered and the processor will halt after recording status information in dual port RAM to identify the nature of the exception. The status information may be accessed by processes running on the main VME microprocessor allowing recovery from the exception.

In normal operation the software moves through the remaining states in Figure 2.10 in the following sequence.

1. The initialisation sets up the data structures and puts the VIOP PI/T interfaces into the correct mode of operation. At the end of initialisation the VIOP cpu enters a waiting mode and will only respond to level 6 or level 7 (non-maskable) interrupts.

2. The level 6 interrupt, handled by the *IntVME* ISR, is generated by the main VME computer card after it has placed information regarding the type of measurement to be made in dual-port RAM. The *IntVME* ISR then resets the FIFOs on the digitising cards, arms the digitising hardware and exits leaving the VIOP cpu in another waiting state, this time with interrupts down to level 3 enabled.

3. When the digitising unit has captured the data for an electron beam pulse, it generates a level 3 interrupt on the VIOP by means of a handshake line on the one of the PI/Ts. The level 3 interrupt is handled by the *IntFIFO* ISR which transfers the contents of the FIFOs into dual-port RAM, calculates the integrated profile if required, resets the FIFOs and writes information about the status of the measurement into a special area of dual-port RAM. Finally, *IntFIFO* generates a VME bus interrupt to tell the main computer card that data is ready. The VIOP cpu then reverts to step 2 and waits for the next level 6 interrupt from the main VME computer.

2.8.2.2   The VIOP device driver

Device drivers are the means by which the OS-9 operating system deals with external hardware in a standard way using operating system calls. The VIOP device driver is an OS-9 SCF (Sequential Character File) device driver and, as is often the case for device drivers for specialised pieces of hardware, it implements only a limited subset of the full SCF device driver functions by means of **GetStat** and **SetStat** system calls. The present driver supports calls which

1. register the device with the operating system and install the interrupt service routine associated with the device,

2. pass parameters to and from the hardware following OS-9 file-manager conventions, and

3. remove all references to the device and its interrupt service routine from the operating system.

The driver writes status information into the dual-port RAM area, generates an interrupt for the VIOP cpu and suspends itself and therefore the calling process, which in normal use will be *viop_meas*, until an interrupt from the VIOP module indicates that measurements are available. Note that many other OS-9 processes, including *opif*, will remain active during this time. When the driver is woken by the interrupt sent on the VME bus by the VIOP, the driver's ISR transfers the data from the dual-port RAM into data structures which may be accessed by the calling program. Two types of data structures are used: an array of 32 integers for the integrated profile and data modules (OS-9 system-wide data structures to which several processes may gain access) for the time-resolved data which may be up to 32 K for any single measurement.

Since OS-9 is a multi-user operating system, care has to be taken to ensure that problems do not arise when more than one user attempts to access the hardware, or when a single user attempts to access it invalidly, for example by requesting a measurement when the system is already busy gathering data. Both problems may be taken care of by the OS-9 operating system firstly by making the access permissions of device driver restrict it to single-user use and secondly by ensuring that the device driver

returns an error message to any process attempting to access it when it is awaiting a response from the hardware.

2.8.2.3   The software upper levels

Figure 2.8shows that there are two processes running under OS-9 on the main computer card, namely *viop_meas* and *opif.* These processes communicate (as shown in Figure 2.9) by means of message-passing via a pipe, used for small amounts of data, in conjunction with interlocking signals which are provided by OS-9 as a standard means of inter-process communication. These are labelled *sig_cmd, sig_OK* and *sig_fail* in Figure 2.9. The large amounts of data from a single measurement are made available in an OS-9 data module. Data modules are a useful feature of OS-9 and are global data areas, the access to which is managed by the operating system.

Opif allows the operator to choose from a series of menus when and how to acquire data and to determine how it is to be processed and displayed. A time-integrated energy profile may be displayed as a histogram and updated every beam pulse. This option involves the smallest amount of data transfer between processes as the time-integration is performed on the VIOP cpu and only 4x32 bytes are transferred via the driver and pipe to *opif* which constructs the display. Other data capture options involve the transfer of data either from a single pulse (up to 32 K) or from a sequence of pulses. These allow the display of time-resolved graphs of the intensity of the beam at a given energy, of mean beam energy, of spectral half-width (i.e. the square root of the variance of the beam energy) as well as three-dimensional energy/time surfaces and contour plots. Examples of these are presented in the critical evaluation of the system in section 2.6.

The graph plotting routines which produce 2-dimensional graphs, contour plots and 3-dimensional displays are implemented in a standard way. *Opif* provides for only the integrated profile display (Figure 2.5, top left) to be updated after each beam pulse, and although either the mean energy or spectral half-width displays (Figure 2.5, middle) could also be updated at this rate there has been no user requirement for this. Continuous updating of the contour or the 3-dimensional displays is not possible with beam pulses repeating at a rate of around 10 Hz. All of the displays are available after a one-shot measurement of the spectrum.

The process *opif* is responsible for initialising the system, including the creation of the data modules and the pipe and spawning the *viop_meas* process. *Opif* is also responsible for unlinking and deleting these structures. The main stages in executing a system function are outlined in the following paragraphs.

The operator selects the required system function using the menu in *opif*. The functions which involve the display or archiving of data are executed by *opif* itself. The previously captured data are obtained by *opif* either from one of the data modules or in the case of the integrated profile from an internal array.

Functions which require the VIOP card to do something - e.g. make a measurement, set operating parameters for the hardware - are the responsibility of the *viop_meas* process. The *opif* process instructs *viop_meas* by placing the command or measurement type details in the pipe and sending a signal (*sig_cmd*) to *viop_meas* to inform it that it has a function to perform.

The *viop_meas* process then uses the VIOP device driver to implement the required function. This is achieved using the **GetStat** and **SetStat** functions. Commands, i.e. functions which do not generate data, are implemented by writing to the appropriate area of VIOP dual-port RAM . Measurements are implemented by the driver writing the measurement type code into the VIOP dual-port RAM and then by generating an *IntVME* interrupt request on the VIOP card to update the measurement type record in the VIOP status area.

The digitising unit captures data for every beam pulse and indicates that the capture process is complete using the FIFO Full signal. This signal can generate the interrupt which causes the VIOP to read the data from the digitising unit and place it in the appropriate locations in the VIOP dual-port RAM. On completion of this stage the VIOP generates a level 3 auto-vectored interrupt on the VME backplane.

The device driver reads the data from the VIOP dual-port RAM on receipt of the interrupt from the VIOP. Integrated profile data are returned to *viop_meas* for placing in the pipe. Raw data (from a single pulse or sequence of pulses) are placed directly into the appropriate data module. If no measurement is able to be taken - e.g. because the accelerator is not running - an error message is returned.

When the device driver has completed the **GetStat** function the *viop_meas* process sends a signal (*sig_OK* or *sig_fail*) to *opif* to indicate that data or an error code is available. The *opif* process can then read this data either from the pipe or the data module.

Chapter 3 Commissioning the system.

3.1   Introduction

In this chapter the commissioning and calibration of the electron spectrometer system is discussed. Its operation with secondary emission detectors (SEM) and optical transition detectors (OTR) is compared and the principal derived measurements—the time integrated energy profile, the mean electron intensity, the mean electron energy and the rms spectral width—are defined. A method for the direct measurement of extraction efficiency, which is used extensively in the investigations in following chapters, is proposed.

3.2   Preliminaries

3.2.1   Modular testing

The system was commissioned in stages. The VME computer hardware and software were thoroughly tested at Dundee in the absence of any digitising electronics, which were still under construction. The operator interface, graphing routines and inter-process communication—as described in the appendix to chapter 2—were thoroughly tested against the specification by using a modified version of the *viop_meas* process which returned simulated data from a file, rather than from the hardware. The low-level software running in the VIOP cpu, was verified against the specification independently of the rest of the system by simulating inputs to this device by means of switches, and checking that the status information recorded in the VIOP memory showed that it obeyed the state-transition diagram in Figure 2.10. Once this had been established, the device driver, which integrates the hardware with the OS-9 operating system, was tested using only the VIOP card and simulated input from switches.

Using the VME system, it was then a simple matter to test the device driver with the digitising electronics and produce data which could be output to a file and analysed using a graphics/spreadsheet package on a PC. The output was found to correspond qualitatively—gains and offsets had not yet been set—to that expected from the input signals. Finally the entire computer and data acquisition system were tested.

A prototype 8-channel digitising card was tested at Dundee using function generators to simulate inputs, and the VME system to display and log the data. Gains and offsets on each of the channels were adjusted appropriately and tests verified that there was no problem with cross-talk or with the noise arising from the hybrid analogue/digital nature of the circuits. Linearity was verified to better than $\pm \frac{1}{2}$ LSB.

3.2.2 SEM measurements

A single 8-channel system, comprising one digitising card and the VME computer system and software, was installed at FELIX and connected to the SEM-1 [1] located as shown in Figure 1.8. In this position, the dipole magnet immediately upstream produced dispersion with sufficient resolution to show useful electron energy spectra: the spectrometer magnet described in section 2.4.1 was not available at this stage. The contour plots in Figure 3.1 show data taken at an electron energy of 20.5 MeV and a nominal 10 μs RF pulse. The calibration in terms of energy—approximately 0.2% per channel—was obtained by varying the dipole current so as to scan a beam with a narrow energy spread across the detector. In normal operation, the electron gun current droops during the macropulse, and this droop is compensated by the application of an appropriately ramped voltage to the grid of the triode gun. The diagrams on the left of Figure 3.1 show the normal situation, with the compensation ramp applied. Note that the peak energy is well defined and stable whereas when the compensation ramp voltage is disabled, the energy peak sweeps continuously throughout the current pulse (by about 1.2%), and the stability is poor, as shown in the diagrams on the right of Figure 3.1.
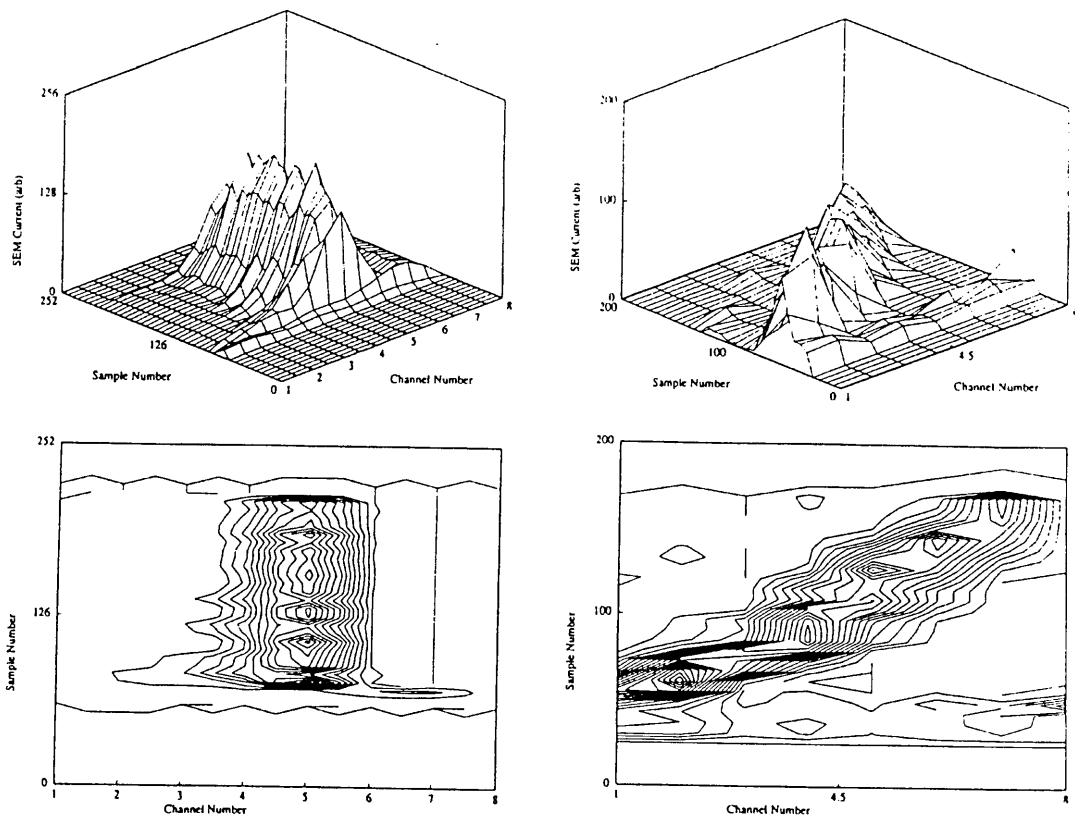
Figure 3.1 *The 3-D and contour plots are of time-resolved data taken at 20.5 MeV and a 10 μs RF pulse. The diagrams on the left are for the case when the compensation ramp is applied to the gun to compensate for a drop in current, producing a stable electron energy spectrum. The data shown on the right are taken with no compensation applied and clearly show energy instability.*

3.2.3 Initial OTR measurements and modifications

Before the installation of the spectrometer magnet, the electron beam leaving the undulator of FEL 2 continued in a straight line into a beam dump. The next phase of testing the measurement system involved a 16-channel digitising set up with an OTR foil placed in an existing SEM vacuum chamber (Figure 3.2) and inserting this into the beam line between the exit of the undulator and the beam dump.
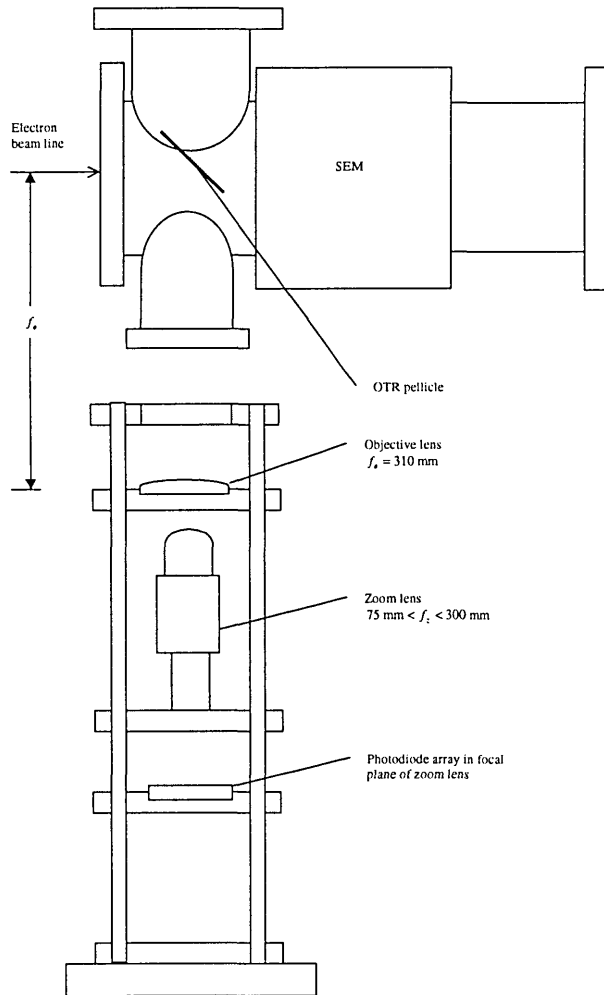
Figure 3.2 *A diagram showing the initial positioning of the SEM and OTR detectors. The OTR pellicle is in the focal plane of the 310 mm focal length objective lens. The zoom assembly provides for variable magnification to allow the full spatial resolution of the detector array to be used over a range of energy spreads.*

The electrons strike the OTR pellicle which is set at 45° to the beam line so that the backward OTR is directed vertically downwards and focussed on to the detector array. The OTR is generated in the focal plane of the objective and imaged by the zoom arrangement so that it covers an appropriate length of the detector array. In this way data from both the SEM and the OTR detector were captured for the same (non-lasing) macropulse. This is illustrated in Figure 3.3 where SEM data is shown on channels 0-7 and OTR data on channels 8-15. There has been no attempt to normalise the signals on the two

detectors—neither in respect of the effective dispersion nor in respect of the magnitude of the signal on each channel—but the good agreement of the general features is noted.

The spectrometer chamber and magnet (Figure 2.1) were then installed at the end of the FEL-2 beamline in the position shown in Figure 1.8. At this juncture, the optical system comprised an 310 mm focal length achromat with $\phi = 80$ mm as an objective (Spindler and Hoyer 32 2278) and a Sigma APO camera zoom-lens assembly with $\phi = 50$ mm and 75 mm $< f < 300$ mm together with a x2 teleconverter. It soon became apparent that the energy spreads produced under certain conditions greatly exceeded the design parameters for the system and were greater than the energy bite of the detector, as shown in Figure 3.4. This surprising result indicates that the extraction efficiency at FELIX is well in excess of the 1.3% predicted by the conventional 1/2N limit [2] is discussed at length in chapters 4 and 6 of this thesis. Had the problem arisen solely from vignetting in the imaging of the OTR spot by the optical system, it would have been possible to measure such large energy spreads by splicing together datasets taken at different settings of current in the spectrometer magnet – effectively scanning the electron beam-spot over the OTR detector foil during successive macropulses. However, attempts to do this failed because the spread in electron energies was in many cases so large that, as the electron beam was steered from its central position, the electrons struck the walls of the vacuum chamber before reaching the dump and produced radiation which swamped the detector.
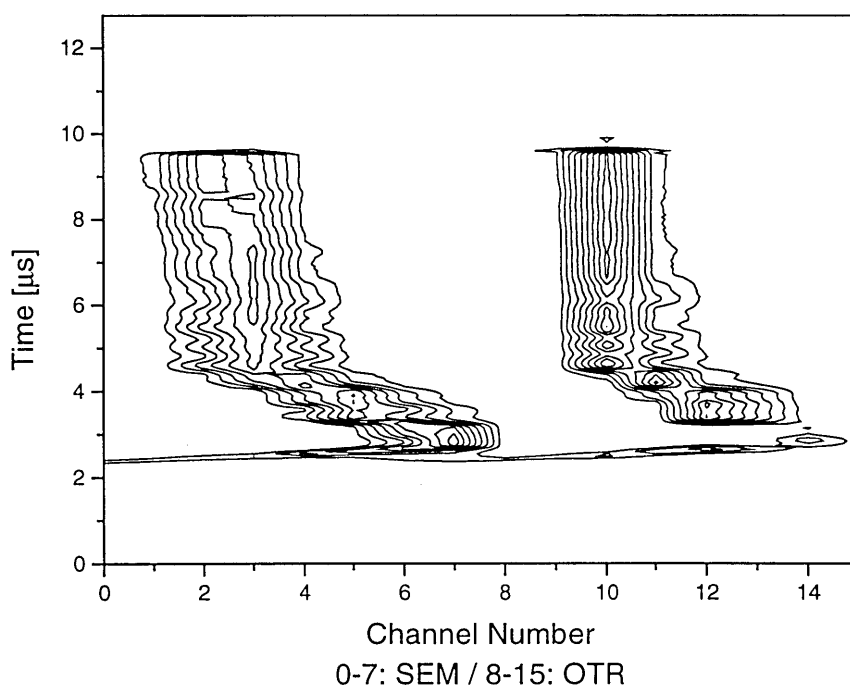
Figure 3.3 *A direct comparison of OTR and SEM electron spectra. Channels 0-7 are coneected to a SEM monitor placed directly behind an OTR pellicle. The remaining channels, 8-15 are connected to 8 of the 32 photodiodes which detect the OTR signal. Note that no attempt has been made to normalise the intensities in the OTR and SEM channels.*

OTR Intensity v Energy & Time

E = 37.2 MeV
λ = 23 μm
ΔL = -1 μm

2
4
6
8

Time [μs]

6
5
4
3
2
1
0

ΔE [%]
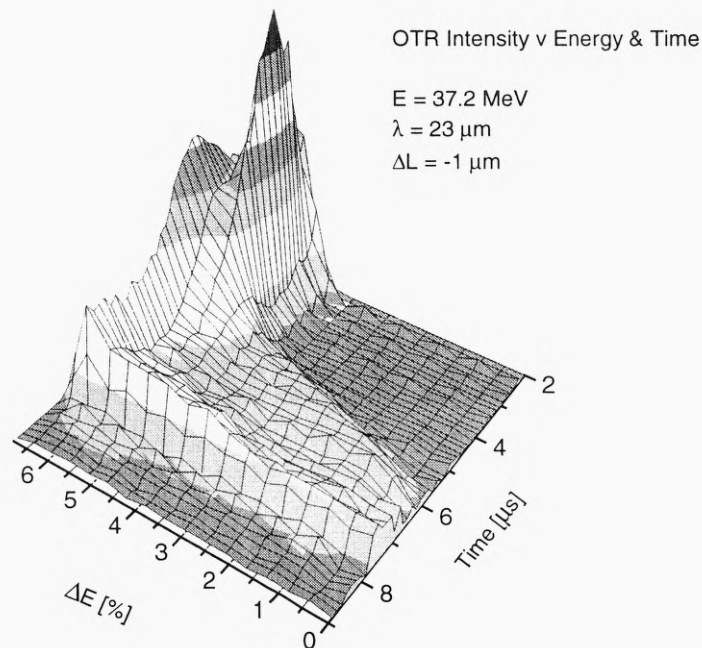
File: 26EL17.DAT

Figure 3.4 *These data, taken at an electron energy of 37.2 MeV , a wavelength of 23μm and a very small cavity desynchronism clearly show that the electron energy spread exceeds the detector energy bite.*

A number of options were considered to improve the situation. Redesign of the spectrometer magnet was too costly and the use of quadrupoles to make a variable-dispersion system was impossible due to lack of space. A curved aluminium OTR radiator was used to compensate for the divergence of the transition radiation ($\pm \frac{4}{\gamma} \approx \pm 44 \, \text{mrad}$) as it leaves the radiator. The optics were re-designed using Spindler and Hoyer achromats: an objective with ϕ = 100 mm and f = 300 mm followed by an achromat with ϕ = 80 mm and f = 160 mm such that there was a reduction in size by a factor of two and the spot size was optimised for optical wavelengths. Other magnifications could be produced by altering the positions of the lenses in the optical tower. The vacuum chamber from the start of the spectrometer to the dump was redesigned to make it as large as possible in the space available. As a result of these modifications, the effective dispersion, as measured on the photodiode array was found to be 0.22 % per channel and the effects of vignetting were considerably reduced resulting in intensity measurements which were constant to within 5% when narrow electron spectra were scanned across the detector. The problem of 'electron loss' with the widest energy spreads remained a limiting factor.

3.3 Energy spectra

Several examples of energy spectra and derived data have already been presented in Figure 2.5, Figure 3.1, Figure 3.2 and Figure 3.4. In this section some of the general features of these measurements are discussed. The raw data are available as an ASCII data file, which was analysed to produce the graphs in this chapter, although many of the displays are available directly from the measurement system on the display in the FELIX control room. The most natural way to view the data is in the form of a surface plot such as Figure 3.4 where the electron intensity is plotted as a function of energy and time, but the general features of energy spectra are more readily apparent if the data are projected onto the energy-time plane and presented as a contour plot.

3.3.1 General features

The contour plots in Figure 3.5 (a) and (b), which were obtained from data taken at 36.2 MeV with an undulator K value of 1.93, show a number of significant features. The two plots are of data taken under very similar operating conditions but from macropulses several minutes apart—in (a) the cavity desynchronism is set so as to prevent lasing whereas in (b) the cavity desynchronism is set at $-50\,\mu\text{m}$ so that lasing takes place at $30\,\mu\text{m}$. The remarkable stability of FELIX, which is present not only from macropulse to macropulse but also over periods of the order of an hour, is exhibited by the fact that the initial transients $(0 - 4\,\mu\text{s})$, which arise from beam loading as the RF cavities fill, are virtually identical in (a) and (b). This stability is important in experiments involving the measurement efficiency, which involves calculating differences in measurements from macropulses taken several minutes apart. Figure 3.5 (a) shows the non-lasing situation where the beam has been set up for a relatively large energy spread which shows a uniform 1.5 % FWHM energy spread from $4.5\,\mu\text{s}$ until the end of the pulse. Figure 3.5 (b) shows the electron spectrum corresponding to lasing at $30\,\mu\text{m}$ with a cavity desynchronism of $-50\,\mu\text{m}$. The onset of saturation at around $4.5\,\mu\text{s}$ manifests itself by an obvious broadening in the energy spectrum and the spectrum eventually shows the characteristic oscillations in the spectrum which are a result of the limit cycle oscillations observed in FELIX at long wavelengths [3].
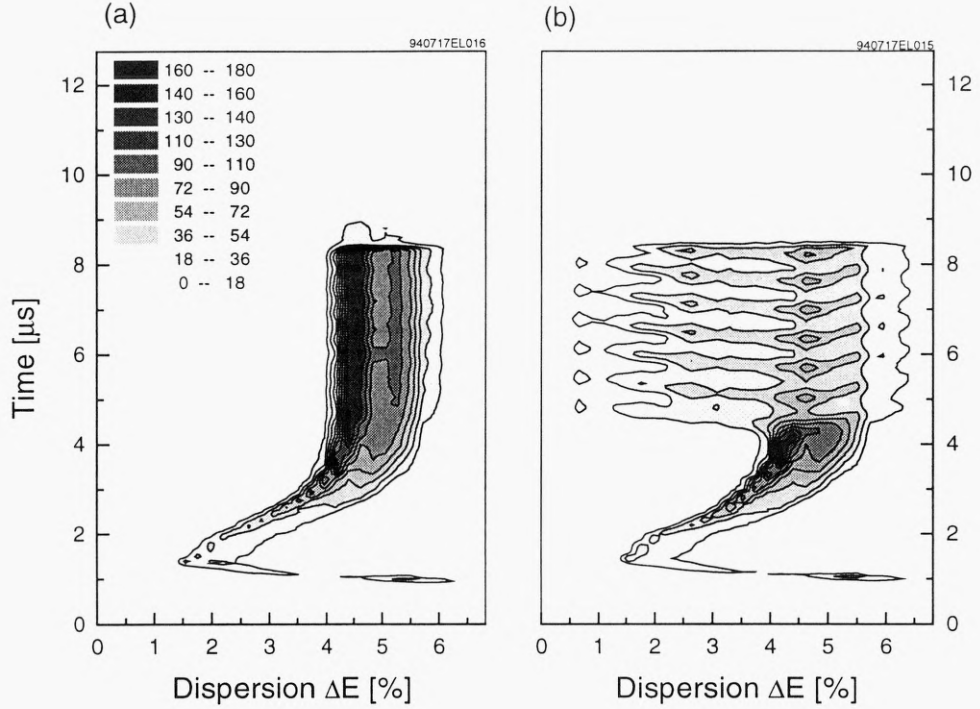
Figure 3.5 *Electron energy spectrum contour plots. Plot (a) shows a typical non-lasing spectrum, where the contours represent the electron intensity at the corresponding energy. The initial transient (0 – 4 μs) is caused by beam loading effects. The remainder of the pulse (4 – 9 μs) exhibits a uniform energy spread of approximately 1.5% (FWHM). Plot (b) shows a lasing spectrum at 30 μm with 50 μm cavity desynchronism. The initial portions of the spectra are almost identical. The onset of lasing at around 4.5 μs is accompanied by a noticeable broadening in the spectrum. The oscillations in the spectral width are due to limit-cycle oscillations in the FELIX output.*

3.3.2 Derived measurements

The most important measurements which can be derived from the spectrometer data have already been introduced qualitatively in section 2.5 and are illustrated in Figure 2.5. These are now defined precisely. The OTR detector array produces signals on channels $m = 0,...,M-1$, where M is typically 32, and the effective dispersion on the detector array is D percent per channel. The signals on each channel are sampled at times t_n, where $n = 0,...,N$, $t_{n+1} - t_n = 20$ ns, and N is typically 512. When n^{th} sample of electron intensity on the mth channel is then denoted by $f_m(t_n)$ we may define the following quantities, of which typical displays are given in Figure 2.5.

1. The (time) integrated profile (Figure 2.5, top left) as $\bar{I}_m = \sum_{n=0}^{N-1} f_m(t_n)$

2. The mean electron intensity (Figure 2.5, top right) as $\langle I(t_n) \rangle = \frac{1}{M} \sum_{m=0}^{M-1} f_m(t_n)$

51

3. The mean electron energy (Figure 2.5, middle left) as $\langle E(t_n) \rangle = \dfrac{D\sum\limits_{m=0}^{M-1} m f_m(t_n)}{\sum\limits_{m=0}^{M-1} f_m(t_n)}$

4. The rms spectral width (Figure 2.5, middle right) as $\langle \sigma(t_n) \rangle = \sqrt{\dfrac{\sum\limits_{m=0}^{M-1} \left(Dm - \langle E(t_n) \rangle\right)^2 f_m(t_n)}{\sum\limits_{m=0}^{M-1} f_m(t_n)}}$.

The integrated profile is useful in optimising the electron beam for a particular energy profile. The mean intensity—which is a measure of the number of electrons reaching the detector—proves useful in showing beam loss both within the spectrometer and elsewhere in the beam-line. In the latter case, a graph of intensity against time shows a dip, indicating that fewer electrons are reaching the detector while in the former, the intensity shows an unexpected peak which arises due to radiation caused by electrons striking the vacuum chamber swamping the detector. This particular diagnostic identified the problems already discussed in 3.2.3.

Although the rms spectral width measurement has proved of little practical value, the measurement of the mean electron energy permits, for the first time, a simple and direct measurement of extraction efficiency, η, of a FEL which is used extensively in the following chapters. This measurement uses the macropulse to macropulse reproducibility of FELIX: two measurements are taken – one of a non-lasing energy spectrum $\langle E_{non-lasing}(t_n) \rangle$ (obtained, for example, by de-tuning the cavity), and one of the lasing spectrum $\langle E_{lasing}(t_n) \rangle$. The efficiency η may then be calculated, as a function of time into the macropulse, as $\eta(t_n) = \langle E_{non-lasing}(t_n) \rangle - \langle E_{lasing}(t_n) \rangle$. This is shown in Figure 3.6, in which the solid line represents $\langle E_{non-lasing}(t_n) \rangle$, the dashed line $\langle E_{lasing}(t_n) \rangle$ and the dotted line $\eta(t_n)$. The mean energies and efficiencies are derived from the data described in 3.3.1: a beam energy of 36.2 MeV with lasing at 30 μm. Note again the excellent agreement between the two mean energies in the initial transient period up to around 4.0 μs. The dashed trace shows the electrons losing energy as lasing commences between 4.0 μs and 4.5 μs with the limit cycle oscillations in the saturated power showing clearly as oscillations in the extracted energy and in the efficiency. The mean extraction efficiency is around 1% in this case. Note that because it is only energy spreads or changes in energy that are important, mean energies are quoted as a percentage deviation from an arbitrary energy determined by the spectrometer magnet current.

Mean change in energy against time

940717el15.dat 940717el16.dat
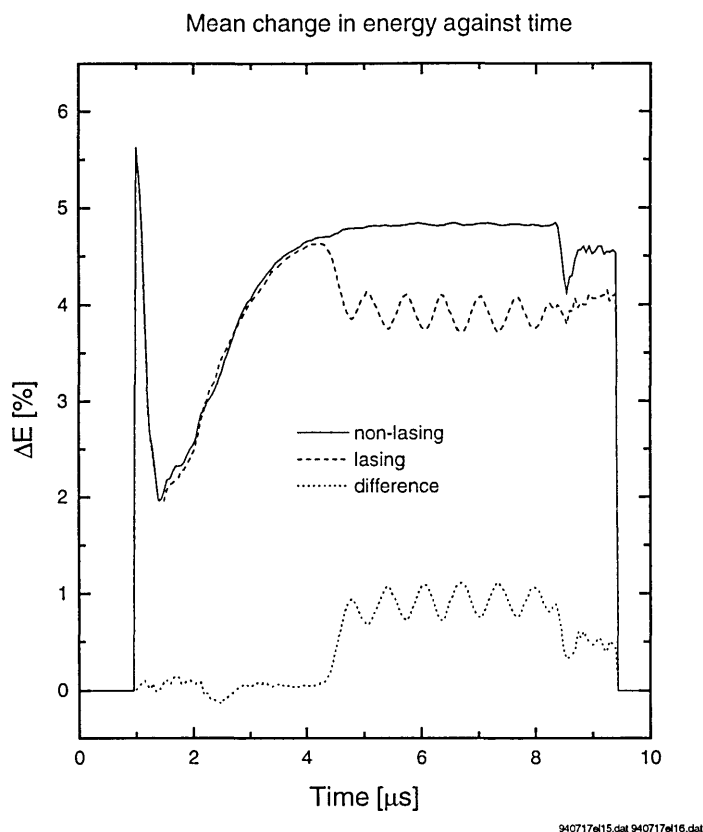
Figure 3.6 *Direct measurement of the extraction efficiency is possible from electron spectrum data. The curves here are derived from the data described in 3.3.1and displayed in Figure 3.5. The solid trace is the mean energy calculated from the non lasingspectrum, and the dotted trace is the mean energy calculated from the lasing energy spectrum: the difference between these is gives the percentage efficiency directly.*

3.4 Evaluation

The electron spectrometer was installed in the FEL-2 beam line in December 1993, and the vacuum chamber was modified in July 1994 to increase the system energy acceptance. This was necessary because the electron spectral widths measured under conditions of large slippage were much larger than anticipated, and the resulting dispersed beam suffered significant loss within the original spectrometer vacuum system.

Since mid-1994 the spectrometer has played an important part in a number of experiments associated with measurements of dynamic energy extraction in the FEL during fixed-wavelength lasing [6], studies of ultrafast scans for use in molecular spectroscopy [5], step-tapered undulator experiments to explore the potential for two-colour operation of the FEL [4], verification of an analytical approach to the theory of short pulse free-electron lasers [7], and investigations into superradiance in free-electron lasers.[8], [9].

3.5 References

1. W. A. Gillespie, P. F. Martin, A. M. MacLeod, A. J. Macdonald, R. J. Bakker, C. A. J. van der Geer , A. F. G. van der Meer and P.W. van Amersfoort, "Time resolved electron spectrum measurements on the FELIX facility", *Nucl. Instr. and Meth*, A **331**, 786-790 (1993)

2. T. C. Marshall, "Free-electron lasers", MacMillan, New York, 1985

3. D. A. Jaroszynski, R. J. Bakker, A. F. G. van der Meer, D. Oepts and P.W. van Amersfoort, "Experimental observation of limit-cycle oscillations in a free-electron laser", *Phys. Rev. Lett.*, vol **70**, pp3412-3415, 1993.

4. D. A Jaroszynski, R. Prazères, F. Glotin, J. M. Ortega, D. Oepts, A. F. G. van der Meer, G. M. H. Knippels and P.W. van Amersfoort, *Phys. Rev. Lett.* **74**, 2224 (1995).

5. G. M. H. Knippels, A. F. G. van der Meer, R. F. X. A. M. Mols, D. Oepts, P.W. van Amersfoort, A. M. MacLeod and W. A. Gillespie, "Feasibility of a far-infrared free-electron laser as a voltage-controlled optical oscillator", *Infrared Physics & Technology*, 37, 285-294 (1996).

6. W. A. Gillespie, A. M. MacLeod, P. F. Martin, G. M. H. Knippels, A. F. G. van der Meer, E. H. Haselhoff and P.W. van Amersfoort, "Electron energy spectral measurements in the large slippage regime", *Nucl. Instr. and Meth*, A **358**, 232-235 (1995)

7. N. Piovella, P. Chaix, G. Shvets and D.A. Jaroszynski, "Analytical theory of free-electron laser oscillators", *Phys. Rev. E*, vol **52**, pp 5470-5486, 1995.

8. D. A. Jaroszynski, P. Chaix, N. Piovella, D. Oepts , G. M. H. Knippels and A. F. G. van der Meer, "Superradiance in a short-pulse free-electron laser oscillator", *Phys. Rev. Lett.*, vol **78**, pp1699-1702, 1997.

9. A. M. MacLeod, W. A. Gillespie, D. A. Jaroszynski and A. F. G. van der Meer, "Cavity losses and extraction efficiencies in a short-pulse free-electron laser", *Nucl. Instr. and Meth*, A **407**, II 41-42 (1998)

Chapter 4 Measurements of the FEL efficiency

4.1 Introduction

A systematic study of extraction efficiency as a function of wavelength and cavity desynchronisation has been undertaken, the results of which agree well with the values expected from conventional theory at moderate values of cavity desynchronisation. At low values of cavity desynchronisation the efficiencies measured exceed the conventional $1/2N$ estimate by between 50% and 100%, and these results are shown to be consistent with the formation of the ultrashort optical pulses—in the region of 6 optical cycles in length—which have been observed experimentally using a second order autocorrelator. The measured values of extraction efficiency are compared with various theoretical estimates.

The extraction efficiency, η, is an important FEL parameter and is defined as

$$\eta = 1 - \frac{U_f}{U_i} \tag{4.1.1}$$

where U_i denotes the energy of the electron bunch at the entrance to the undulator and U_f is the energy at the exit of the undulator. A relatively crude estimation of the efficiency as $\eta = 1/2N$, where N is the number of undulator periods, is found in many textbooks [1,2,3]. It is generally agreed that this is an unrealistically high estimate, since it corresponds to the energy lost by an electron injected with an energy corresponding exactly to the top of the separatrix (Figure 1.4) performing exactly one half of a synchrotron oscillation as it traverses the undulator. Several possibilities have been investigated to increase the intrinsically low efficiency ($\eta = 1/2N$) of a Compton FEL. Tapering of the undulator in an FEL amplifier configuration has been effective [4]. Since this tapering reduces the small-signal gain, it is not a very attractive way to increase the efficiency in an oscillator configuration. Measurements of the efficiency in oscillators employing an untapered undulator have been performed at several laboratories. The FEL group at Los Alamos have reported efficiencies of up to 0.8 % (for N=37) with a uniform undulator when the FEL operated in the spiking regime [5], whereas work at the ELSA free-electron laser, CEA Bruyères-le-Châtel, has generated values of up to 2.5 % (for N=30) [6]. These high efficiencies were achieved with high electron bunch charges (3.5nC in a 10ps bunch at Los Alamos, and 1.5 nC in a 20 ps bunch at CEA). Theoretical work at CEA on the efficiency and electron spectral width expected in the case of a relatively long electron bunch (the continuous beam limit) has led to a description in terms of a stochastic diffusion process [7]. This theory is valid as long as the FEL operates in the so-called post-sideband regime, a highly saturated regime characterised by a broad and turbulent optical spectrum, and it predicts a constant ratio between the extraction efficiency η and the optical spectral width Σ [8,9]. Data from FELIX (where $N = 38$ suggests $\eta \le 1.3\%$) showing extraction efficiencies of up to 2% are presented later in this chapter.

When the FEL gain is high enough to reach the spiking regime [10], the optical field strength increases at certain positions in the optical pulse leading to the formation of a train of chaotic spikes that starts growing from the leading edge of the pulse. The development of such a train of pulses, which are generally separated by the synchrotron length—defined as the slippage distance that occurs in one period of the synchrotron oscillation of the electrons [11]—leads to a new equilibrium for the efficiency and the optical pulse duration.

4.2 Efficiency and cavity desynchronisation

Time-resolved electron and optical spectra have been measured over a range of laser wavelengths and cavity desynchronisations. The wavelength range 8 – 30 μm spans that of undulator FEL-2 at FELIX. Electron and optical spectra are simultaneously acquired during a single macropulse, and comprise 32 time-resolved electron energy channels and 48 time-resolved optical wavelength channels. The electron spectra typically span a 7% energy bite, although this can be varied by altering the OTR optical system. The relative sensitivities of the electron channels are checked at the beginning of each experimental run by stepping a narrow electron spectrum across the detector array, and calculating the integral of the time-averaged spectrum at each position. The sensitivities determined by this method show good uniformity across the whole array; only at the very edge channels does the response drop off due to vignetting in the OTR optics.

Modifications to the OTR detector include a curved radiator to focus the OTR angular distribution in the dispersion plane, allowing the array to span 7% in energy for the measurements reported here. Calibration spectra taken with this configuration demonstrated a very uniform response over the whole energy range, and the response of the complete diagnostic system (optical + electron) was checked for consistency by using the measured cavity ringdown data to reconstruct the extraction efficiency from a knowledge of the FEL optical macropulse.

The optical diagnostics comprise a second-order autocorrelator for measuring the optical pulse length, a bolometer to measure the total optical power, a pyroelectric detector with a response time of approximately 100ns to measure the optical power envelope, and a 48-channel spectrometer (Acton Research Corporation, Massachusetts, SpectraPro VM-504) equipped with a three-grating turret to cover the wavelength range from 5 μm to 110 μm. The spectrometer uses a linear array of pyroelectric detectors sampled at a maximum frequency of 10 MHz. The bandwidth of the pyroelectric detectors and amplifiers is 600 kHz. The autocorrelator is based on second-harmonic generation in a crystalline sample of CdTe, and is described in more detail in [12] and references therein. A crossed-beam set-up is used to obtain a background-free autocorrelation signal. The large transparency range and low dispersion of CdTe make it possible to operate the autocorrelator between 5 and 35 μm with one single crystal. The large bandwidth for the second-harmonic process (crystal thickness is 0.5 mm), results in a resolution of 200 fs around 10 μm wavelength. The autocorrelation trace is measured by scanning the variable delay branch. An autocorrelation trace consists of roughly 100 laser macropulses and takes two

minutes to record. The optical diagnostics are evacuated to avoid absorption of the infrared laser light by ambient water vapour.
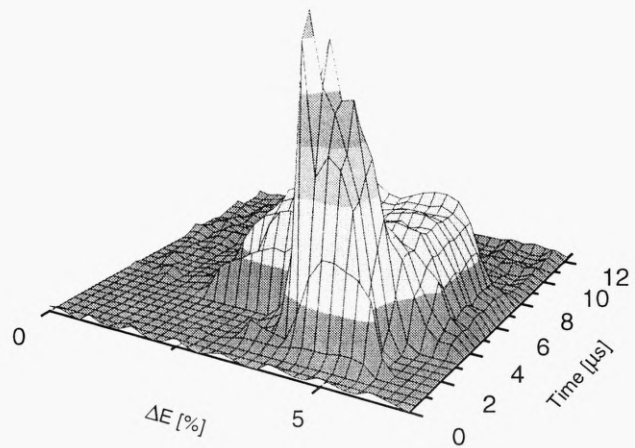
OTR Intensity v Energy & Time A25EL064.mat

Figure 4.1 *A 3-D plot of the electron spectrum corresponding to an initial electron energy E=46.0 MeV, a central emission wavelength λ=16 μm and a cavity desynchronisation ΔL=-1.0λ.*
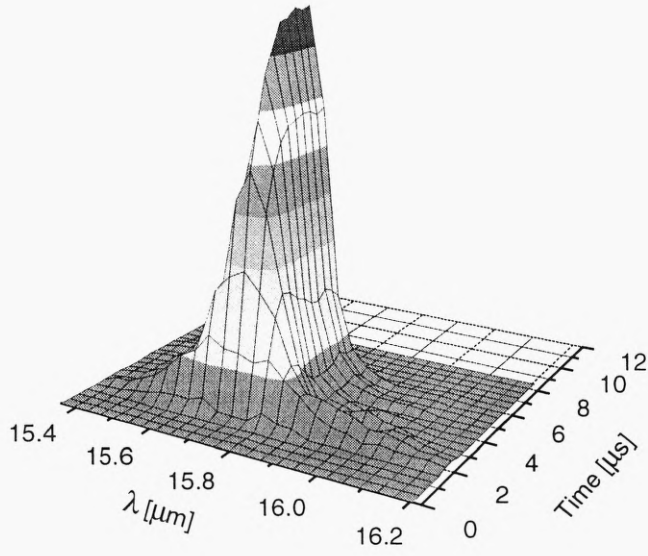
Optical power v λ and time sa25jul.031

Figure 4.2 *3-D plot of the optical spectrum corresponding to an initial electron energy E=46.0 MeV, a central emission wavelength λ=16 μm and a cavity desynchronisation ΔL=-1.0λ.*

Typical electron and optical spectra are displayed in Figure 4.1 and Figure 4.2 respectively as 3-D plots. These figures correspond to an initial electron energy E=46.0 MeV, a central emission wavelength λ=16 μm and a cavity desynchronisation ΔL=-1.0λ. Figure 4.2 shows the OTR intensity, which is proportional to the number of electrons, versus electron energy (in percent deviation from an arbitrary zero) and time. The time-resolved optical spectrum corresponding to Figure 4.1 is displayed in Figure 4.2. The FEL-2 undulator has two identical sections, the gaps of which were adjusted to produce a slight "anti-taper", which has been shown to be effective in suppressing synchrotron sidebands [13,14]. The optical spectrum exhibits no prominent sidebands. Figure 4.3 shows the variation of mean energy with time for lasing and non-lasing spectra taken at λ= 29.0 μm and ΔL ≅ 0 μm: the dotted curve is the measured electron energy spectrum without lasing (i.e. with the optical cavity strongly desynchronised); the solid line is the corresponding final electron spectrum after the laser interaction , and the dashed curve is the difference between the first two, yielding the electron energy loss or extraction efficiency. For these data, the rms spectral width is calculated to be Σ = 1.85% and the efficiency peaks at η = 1.8%, a high value for a bunch charge of 200pC. It is worth noting yet again the excellent agreement between the non-lasing and lasing energy distributions in the early part of the FELIX macropulse. This is a common characteristic of these data, and indicates stability of the spectra over time periods of at least several minutes.

Evidence of the consistency of the optical and electron measurements is given in Figure 4.4. When the extraction efficiency as a function of time in the macropulse $\eta(t)$ is measured, the optical macropulse $P(t)$ may be reconstructed, assuming constant cavity losses α by integrating the energy balance equation

$\frac{dP}{dt} + \alpha P = \eta(t)$. The value for the cavity loss coefficient α is obtained from the exponential tail of the optical macropulse as it decays after the electron beam has been switched off. Note that the vertical scale for the reconstructed optical macropulse is obtained by fitting it to the measured optical pulse. The results shown in Figure 4.4 (a) correspond to lasing at a wavelength of 16 μm and a cavity desynchronisation of $-\lambda$ and correspond to the data presented in Figure 4.1 and Figure 4.2. Agreement is good over a range of wavelengths and desynchronisms, indicating consistency between the optical and electron energy data, and fails only in cases where the energy spread of the electron beam after lasing begins to exceed the energy bite of the spectrometer, as in Figure 4.4 (b), which was produced from the electron energy data shown in Figure 4.3.
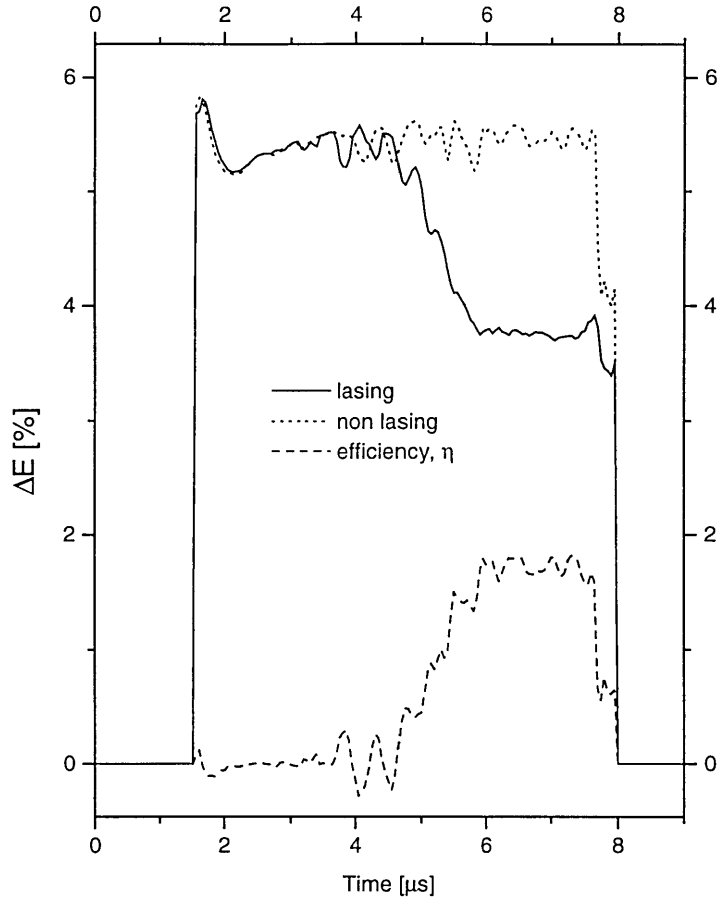
ΔE and η v t. Files: 26EL01.DAT, 26EL03.DAT -> 26EL01.EFF

Figure 4.3 *The variation of mean energy with time for lasing and non-lasing spectra taken at λ= 29.0 μm and ΔL ≅ 0μm: the dotted curve is the measured electron energy spectrum without lasing (i.e. with the optical cavity strongly desynchronised); the solid line is the corresponding final electron spectrum after the laser interaction, and the dashed curve is the difference between the first two, yielding the electron energy loss or extraction efficiency.*

Optical and electron energy measurements were taken at a range of wavelengths between 8 μm and 29 μm and at cavity desynchronisation ranging from near zero to -2λ. Figure 4.5 summarises the efficiency measurements as a function of radiation wavelength and cavity desynchronisation. The measured efficiencies are shown as open circles. As expected, the highest efficiencies correspond to the near-zero desynchronisation; at several longer wavelengths, the efficiency approaches $\eta = 2\%$. Also shown for comparison are (1) the efficiencies estimated using a simple model that is discussed in the following section (plotted as open squares), and (2) the efficiencies calculated from simulations using the code ELIXER [15] (plotted as open triangles). At several longer wavelengths, the measured efficiency approaches 2%, more than 50% greater than the conventional $1/2N$ estimate (1.3% for FELIX).
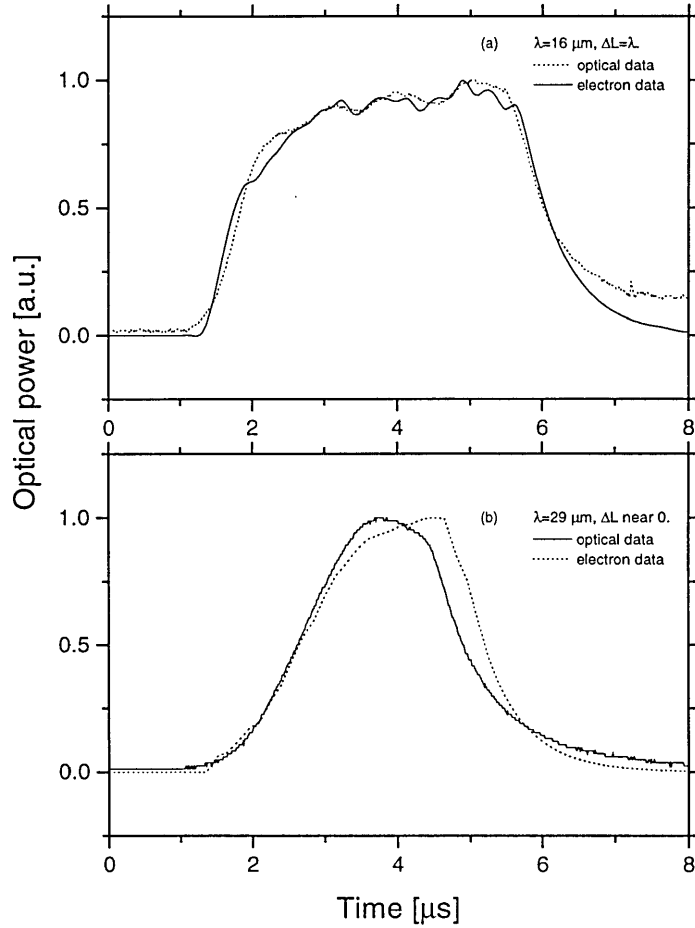
Figure 4.4 *The consistency of the optical and electron measurements at (a) 16 μm and a desynchronisation of −0.1λ and (b) at 29 μm and near zero desynchronisation. The optical pulse (shown as a solid line) may be accurately reconstructed (shown as a dotted line) from electron energy data, as in (a) over a range of wavelengths and desynchronisations. The reconstruction is less good, as in (b) when the energy spread begins to exceed the acceptance of the spectrometer.*

4.3 Theoretical background

When the electron beam in an FEL is produced by a radio-frequency (RF) linac, the electrons emerge in short (picosecond) bunches separated by fixed (nanosecond) periods determined by the frequency of the RF source. The spacing of the electron bunches is a multiple of the period of the RF field, and a long train of these bunches constitutes the electron macropulse, typically several microseconds long, which is repeated several times per second to yield the desired average power. The radiation in the optical cavity naturally also exhibits this structure and consists of a train of short, equally-spaced micropulses. Laser

oscillation is achieved if the optical cavity length is chosen so that the round-trip time for a micropulse is precisely matched to the period of the fresh electron bunches entering the undulator.

Electrons which enter the undulator at the same time as an optical micropulse gradually slip behind the micropulse, both because their velocity is less than that of light in vacuo and because their trajectories are not straight lines. The FEL resonance condition for the fundamental radiation is that this slippage should be equal to one radiation wavelength, λ, per undulator period traversed so that an electron bunch slips back relative to the optical micropulse by a "slippage distance" $L_s = N\lambda$ in an undulator comprising N periods. Slippage effects are characterised by the longitudinal coupling parameter,

$\mu_c = \dfrac{N\lambda}{\sigma_z}$, where $\sigma_z^{\,2}$ is the variance associated with the longitudinal electron density profile (σ_z is

half the "bunch length"). In most FELs $\mu_c \ll 1$ so that slippage effects are relatively unimportant. However, in FELIX the combination of short bunch length and long radiation wavelength gives values of μ_c between 0.3 and 10 [16]. The short bunch leads in turn to a short optical micropulse duration. Pulses containing only six cycles of the optical field have been observed at FELIX at a number of wavelengths, and have been reported elsewhere [17].

Due to the fact that the gain is enhanced towards the downstream end of the undulator, by which point the electron bunch has slipped back with respect to the optical micropulse, the micropulse peaks at its trailing edge. This change in shape of the optical micropulse may be viewed as a reduction in its group velocity. Thus, in a perfectly synchronised cavity, the optical micropulse would continue to retard and narrow on each pass through the undulator. This reduced contact with the gain medium leads to a reduction in the gain per pass and restricts the growth of laser power; this effect is known as "laser lethargy" (see 1.3.2 and references therein) and may be compensated for by a slight reduction in the cavity length (ΔL) from the value corresponding to a perfectly synchronised cavity in such a way that the peak of the optical micropulse is advanced again with respect to the next electron bunch entering the undulator. When the laser saturates, however, there is no further amplification and therefore the group velocity of the optical micropulse returns to its vacuum value. Maximum power under these conditions will be achieved only for a cavity length close to perfect synchronism. It may thus be seen that the saturated power and the small-signal gain depend in opposite senses on the cavity desynchronisation, ΔL : small values of ΔL lead to a high saturated power but slow growth, while larger values ensure rapid growth to a smaller saturated value. Note that by dynamically altering the desynchronisation during the build-up of laser power it is possible to arrange for rapid growth coupled with large output powers [18].

When the saturated power level is high enough, reabsorption of optical energy by the synchrotron motion of the electrons in the ponderomotive well becomes important. The combination of reabsorption of radiation and cavity desynchronisation modulates the optical pulse envelope. Since the optical pulse moves away from the electron bunch due to the applied cavity desynchronisation, the leading edge of

the optical micropulse will eventually decay due to cavity losses. A new pulse rapidly begins to develop from the trailing edge of the micropulse. In this way a single micropulse evolves, over several round trips, into a train of sub-pulses and this exhibits itself as an oscillation in the optical power envelope.

The synchrotron motion is important for the saturation process, since it is related to the maximum energy that can be extracted from the electron beam. The synchrotron frequency Ω is defined as [4,19]

$$\Omega = \frac{c}{N\lambda}\sqrt{|a|} \qquad (4.3.1)$$

where $a = |a|e^{i\phi}$ represents the dimensionless complex field formed by the combined fields of the undulator and the optical radiation. The value of $|a|$ is given by [2]

$$|a| = (4\pi N)^2 \frac{K}{1+K^2}(J_0(\xi) - J_1(\xi))\frac{e\lambda E}{2\sqrt{2}\pi mc^2} \qquad (4.3.2)$$

$$\xi = \frac{1}{2}\frac{K^2}{1+K^2} \qquad (4.3.3)$$

where K is the (rms) undulator strength and E is the envelope of the complex electric field. The parameter K is a dimensionless parameter proportional to the peak magnetic field, B_u, in the undulator,

$$K = \frac{eB_u\lambda_u}{2\sqrt{2}\pi mc} \qquad (4.3.4)$$

where λ_u, e, m, and c are the length of an undulator period, the electron charge, the electron rest-mass, and the vacuum velocity of light, respectively. The Bessel functions J_0 and J_1 account for the fact that a planar undulator is used.
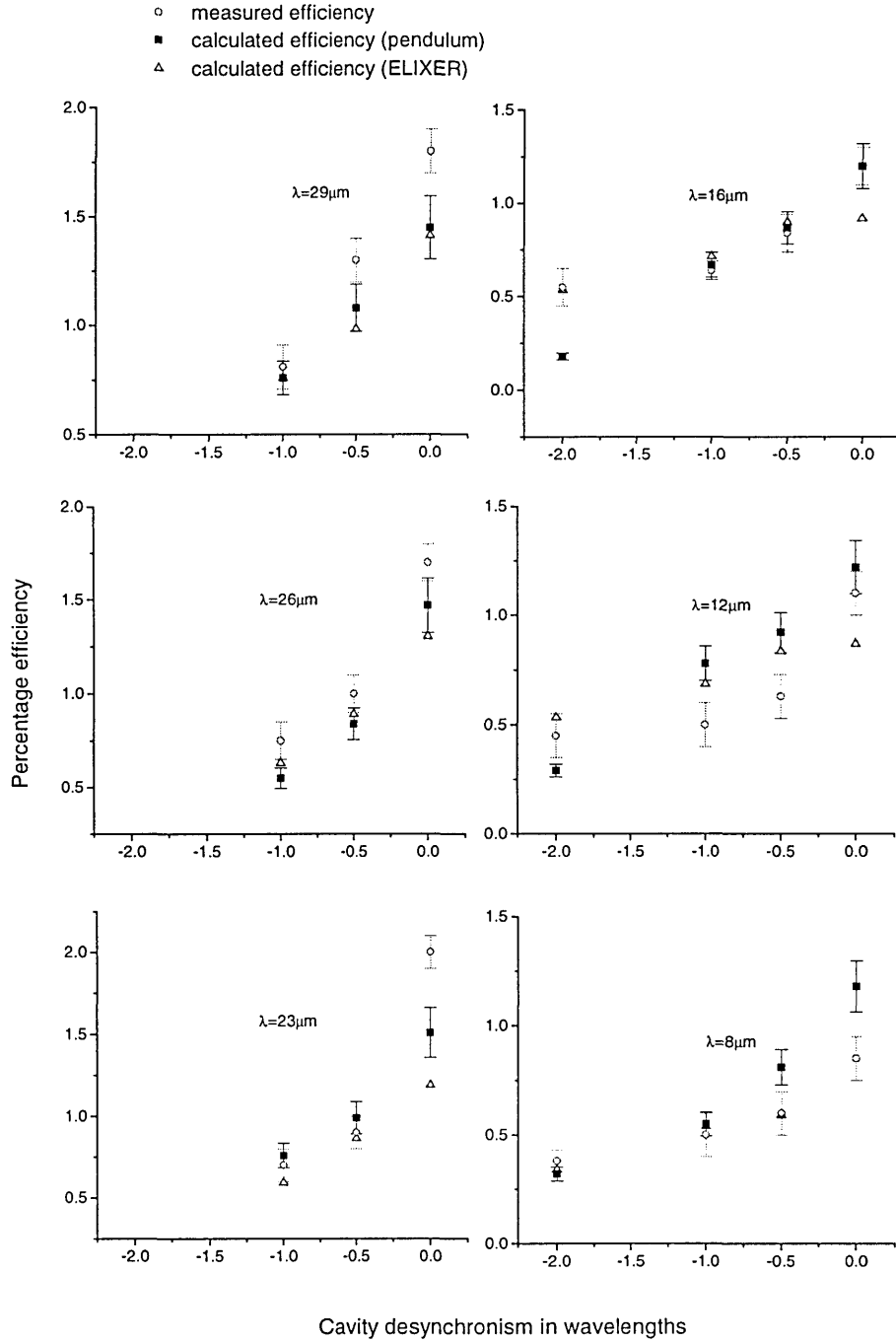
Figure 4.5 *Plots of the measured efficiency (circles), efficiency calculated using the 'pendulum' model in section 4.4 (squares) and efficiency obtained from simulations using the code ELIXER (triangles) as a function of cavity desynchronisation in wavelength units for lasing at at 8 μm, 12 μm, 16 μm, 23 μm, 26 μm and 29 μm. The highest efficiencies occur at low desynchronisations and both models predict the general trend of the measured results, but efficiencies at low desynchronisations and long wavelengths are greater than predicted by the simple model or the full simulation.*

4.4 Estimates of extraction efficiency

To estimate the energy extracted from the electron beam when the electrons perform their synchrotron motion, we use the depth of the separatrix in phase-space (see Figure 1.4). The separatrix defines the boundary between trapped and untrapped particles. The efficiency η, defined as the ratio between the energy ΔU lost by the electrons and the electron beam energy U, can then be written as

$$\eta = \frac{\Delta U}{U} = \frac{\Delta \gamma}{\gamma} = \frac{\Delta v}{4\pi N} \tag{4.4.1}$$

if we note that Δv is the change in the dimensionless energy given by $\Delta v = 4\pi N \Delta\gamma/\gamma$. The maximum depth of the separatrix is given by $\Delta v = 4\sqrt{a}$, leading to an expression for the maximum achievable efficiency of

$$\eta = \frac{\sqrt{a}}{\pi N} \tag{4.4.2}$$

The assumption that saturation sets in at $\sqrt{a} = \pi/2$ leads to the well-known $1/2N$ estimate for the maximum efficiency [2,3]. Experimental results presented here show that efficiencies 50% larger than this may be obtained and indicate that this is because the value of $\sqrt{a}$ can become substantially higher.

The value of a can be calculated from equations (4.3.2)-(4.3.4) if the electric field amplitude E is known. An estimate of the intracavity power allows us to calculate the intracavity electric field, since

$$P = \frac{1}{2} c \varepsilon_0 A E^2 \tag{4.4.3}$$

where A is the effective mode area in the cavity. It can be shown [20] that a disk of diameter πw_0 (where w_0 is the spot size at the waist) encloses 99% of the power at the beam waist, assuming a transverse Gaussian beam profile. Using fact that at FELIX the Rayleigh length equals half the undulator length L_u [21], the effective mode area is then given by

$$A = \frac{\pi^2 L_u \lambda}{8}. \tag{4.4.4}$$

Combination of equations (4.4.3) and (4.4.4) results in an electric field of

$$E = \sqrt{\frac{16P}{c\varepsilon_0 \pi^2 L_u \lambda}} \tag{4.4.5}$$

which enables the calculation of a for a given value of the intracavity peak power. The latter can be estimated from outcoupled power, measured by the pyroelectric detector, the cavity losses, and the measured optical micropulse duration.

Note that the value of $\sqrt{a}$ may be determined in this way entirely from optical data and used in equation (4.4.2) to provide an improved estimate of the extraction efficiency which is then measured purely from electron energy.

Several estimates are presented in the following paragraphs and comparisons with the data from the electron measurements are shown in Figure 4.5 and in Table 4-1.

1. The conventional assumption of $\sqrt{a} = \pi/2$ at saturation leads to $\eta_1 = 1/2N$, as previously mentioned. This is a very crude estimate, giving a fixed value of 1.3% for FELIX. This value is not shown in Figure 4.5.

2. Using the value of $\sqrt{a}$, estimated from the optical measurements, in equation (4.4.2) yields an estimate η_2 which may be expected to set an absolute maximum for the possible extraction. This is indeed the case, and values are consistently higher than the measurements by a factor of the order of 2.5, and are again not plotted in Figure 4.5. Representative values, for the cases of near zero and one wavelength desynchronisation, are shown in Table 4-1. Note that the value calculated represents the entirely unrealistic case when all the electrons fall from the top to the bottom of the separatrix.

3. The electron dynamics in the ponderomotive potential maybe described by the pendulum equation [2,3]:

$$\ddot{\psi} = -|a|\sin(\psi) \tag{4.4.6}$$

where ψ is the electron phase, and a dot represents differentiation with respect to the dimensionless time τ which runs from 0 to 1 as the electrons traverse the undulator. The dimensionless energy, v used in (4.4.1) is given by $v = \dot{\psi}$. Using the optical estimate for $|a|$ as before, and assuming it to be constant at saturation, equation (4.4.6) may be integrated numerically to yield a value for Δv. By considering an ensemble of electrons entering the undulator with an initial energy v_0 but with a random spread of phases it is possible to find the average energy loss of these electrons and further, to maximise this over initial energies and evolution time in the undulator.

$$\overline{\Delta v} = \max_{\substack{0<v_0<2\sqrt{a} \\ 0<\tau<1}} \langle \Delta v \rangle \tag{4.4.7}$$

$\overline{\Delta v}$ is thus an estimate of the maximum average energy loss possible from such an ensemble of electrons. The maximisation over τ corresponds to the physically unrealistic situation where the

synchrotron motion in the ponderomotive potential is stopped just before the commencement of any net absorption of energy by the electrons. In this way the third estimate η_3 is formed, which could reasonably be expected to place an upper bound on the measurable efficiency. This is found to be the case (see Figure 4.5, solid squares) except at long wavelengths and small desynchronisations. The anomalous results at desynchronisations of -2λ at 12 µm and 16 µm are not understood.

4. The simulation code ELIXER [15] was augmented to provide output of the electron energy data at the end of each pass. This allowed the mean electron energy to be calculated and hence values for the extraction efficiency. These values are plotted as triangles in Figure 4.5.

Table 4-1 *Comparison of the efficiencies, measured pulse duration and synchrotron length for FEL-2 at a number of wavelengths and near zero cavity desynchronisation(left hand pane) and one wavelength desynchronisation (right hand pane). The symbols, from top to bottom, indicate the wavelength, the efficiency as measured from the electron energies, an upper bound for the efficiency defined in paragraph 2 above, the efficiency from the 'pendulum model' of paragraph 3 above, the cavity losses per round trip, the FWHM optical pulse duration, the square root of the dimensionless optical field strength and the synchrotron length in mm.*

	Near-zero cavity desynchronisation						One-wavelength cavity desynchronisation					
λ [µm]	8	12	16	23	26	29	8	12	16	23	26	29
η [%]	1.0	1.1	1.2	2.0	1.8	1.8	.45	0.5	0.6	0.7	0.7	0.8
η_2 [%]	3.5	3.6	3.6	4.5	4.4	4.3	2.3	2.6	2.5	2.6	2.31	2.6
η_3 [%]	1.2	1.2	1.2	1.5	1.5	1.4	0.55	0.78	0.67	0.76	0.55	0.76
α [%]	9	8	8	6	6	5	9	8	8	6	6	5
τ [fs]	370	470	670	645	760	780	970	670	1000	1420	2100	1520
$\sqrt{a}$	4.2	4.3	4.2	5.4	5.2	5.2	2.8	3.2	3.0	3.1	2.7	3.1
L_{syn} [mm]	0.5	0.6	0.9	1.0	1.2	1.3	0.7	0.9	1.3	1.8	2.3	2.2

4.5 Discussion

Uncertainties in the efficiency values have been omitted for clarity. The efficiency values measured from the electron data are accurate to ±10%. To assess the uncertainty in the optical calculations is more difficult: the cavity losses are known to within 10% and although errors in the calculation of the intracavity power—especially from the estimated pulse times—are potentially large, they enter in to the calculation raised to the power of ¼ so that the effect of the error is reduced. The 'optical' efficiencies and the calculations of synchrotron lengths are therefore probably accurate to between ±10% - ±20%. A more serious problem is that because the radiation is coupled out of the cavity by a hole in the upstream mirror, the actual intracavity power could be considerably higher that the estimates here due to the presence of cavity modes with zero on-axis power. All efficiencies calculated from the optical data would therefore be underestimates.

The dependence of the measured efficiencies on the cavity desynchronisation is reasonably well understood, at least qualitatively. Operation at larger cavity desynchronisations results in lower efficiencies because of the consequently poorer overlap between the optical pulse and the electron bunch at saturation. This leads to low saturated power and a slow synchrotron motion in the ponderomotive well—in fact the electrons do not fall far in the well and the efficiency remains low. At the smallest cavity desynchronisation, the synchrotron motion is so fast that the electrons at the rear of the optical pulse start re-absorbing the optical field before they leave the undulator. This re-absorption shortens the optical pulse and allows a new equilibrium to be reached with a higher optical power and a shorter optical pulse. The measured data clearly exhibit these trends in the efficiency, the optical pulse duration, the optical field strength and the synchrotron length, i.e. the distance the electrons slip behind the optical field in one period of the synchrotron oscillation in the ponderomotive well. This mechanism allows the optical power and efficiency to become higher than the crude $1/2N$ estimate (η_1). One could argue that when optical pulses are formed which are shorter than the electron bunch length, as is the case here, that they interact with any given electron for only part of the length of the undulator before that electron loses contact with the optical pulse. In this way the effective value of N for the undulator is reduced.

It is significant that the measured values of efficiency exceed all estimates except the unrealistically high η_2 value at longer wavelengths and small cavity desynchronisations. The reason for this is apparent when considering the measured duration of the optical pulses involved: for example only eight optical cycles at 29 μm and zero cavity desynchronisation. Under these circumstances the "slowly varying optical envelope" approximation—used in the theory leading to the ideas of ponderomotive potential and the pendulum equation [2,3]—is no longer valid. The same approximation is built in to the simulation code ELIXER.

4.6 'Anomalously large' energy spreads

Figure 4.6 shows a final electron spectrum taken at E = 37.2MeV, λ = 23.0μm, and ΔL = -1μm. Clearly visible towards the end of the 6.5μs macropulse is the broad final electron distribution (>7% wide) evolving from the original narrow "double-humped" electron spectrum. Experience with FELIX is that the best lasing conditions are in general not achieved by setting the linac to produce the narrowest energy spectrum entering the undulator, but rather by deliberately broadening the input spectrum and relying on the non-isochronicity of the injection chicane to compress the electron pulse, thereby enhancing the pulse current. This broadened spectrum is typically 0.6-1.0% FWHM, compared with a "minimised" spectral width (rms) of < 0.2%. For the present experimental runs it proved beneficial to generate a "double-humped" electron spectrum with a total rms width of 1.5%, although the reason for this is not yet clear. In Fig.6 the lasing spectrum extends significantly beyond the 7% bite of the OTR detector. A realistic extrapolation of the data suggests that the true efficiency may be closer to 2.5%.
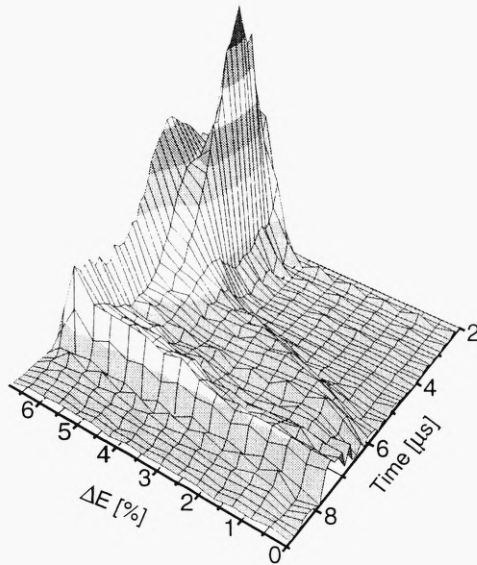
Figure 4.6 *The electron energy spectrum taken at $\lambda = 23.0\mu m$, and $\Delta L = -1\mu m$ Clearly visible towards the end of the 6.5μs macropulse is the broad final electron distribution (>7% wide) evolving from the original narrow "double-humped" electron spectrum A realistic extrapolation of the data suggests that the true efficiency may be closer to 2.5%.*

4.7   References

1. G. Dattoli and A. Renieri, "Experimental and theoretical aspects of the free electron laser", in *Laser Handbook Vol. 4*, edited by M. L. Stitch and M. Bass, North-Holland, Amsterdam, pp. 1-133, 1985

2. W.B. Colson, "Classical Free electron theory", in *Laser Handbook Vol 6*, edited by W. B. Colson, C. Pellegrini and A .Renieri, North-Holland, Amsterdam, pp 115-194, 1990.

3. T. C. Marshall, "Free-electron lasers", MacMillan, New York, 1985.

4. N. M Kroll, P. L. Morton and M. N. Rosenbluth, "Free-electron lasers with variable parameter wigglers", *IEEE J. Quantum Electronics*, **17**, pp 1436-1468, 1981.

5. B. E. Newnam et al., "Optical performance of the Los Alamos free-electron laser", *IEEE J. Quantum Electronics*, **21**, pp 867-881, 1985.

6. D. Iracane, V, Fontenay, P. Guimbal, S. Joly, S. Striby and D. Touati, "Experimental evidence for high efficiency, low brightness behavious in free-electron lasers", *Phys. Rev Lett.*, **72**, pp 3985-3988, 1994.

7. P. Chaix, D. Iracane and C. Benoist, "Stochastic electronic motion and high efficiency free-electron lasers", *Phys. Rev E.*, **48**, pp R3259-3262, 1993.

8. D. Iracane, P. Chaix and J. L. Ferrer, "Spectral behaviour of high-power Compton free-electron lasers I. Broadening and asymptotic equilibrium", *Phys. Rev. E*, **49**, pp. 800-814, 1994.

9. D. Iracane, P. Chaix and H. Delbarre, "Spectral behaviour of high-power Compton free-electron lasers II. Effect of filtering and tapering on sideband generation", *Phys. Rev. E*, **49**, pp. 815-827, 1994.

10. B. A. Richman, J. M. J. Madey and E. B. Szarmes, "First observation of spiking behaviour in the time domain in a free-electron laser", *Phys. Rev. Lett.*, **63**, pp 1682-1684, 1993.

11. S. J. Hahn and J. K. Lee, "Non-linear short-pulse propagation in a free-electron laser", *Phys. Rev. E.*, **48**, pp2162-2171, 1993.

12. G. M. H. Knippels, "The short pulse free-electron laser: manipulation of the gain medium", Doctoral thesis, section 2.1 pp19 – 32, Free University of Amsterdam, 1996.

13. D. A. Jaroszynski, R. Prazeres, F. Glotin, J.M. Ortega, D. Oepts, A.F.G. van der Meer, G.M.H. Knippels and P.W. van Amersfoort, "Free-electron laser efficiency enhancement, gain enhancement, and spectral control using a step-tapered undulator", *Phys. Rev. Lett.*, vol. 74, pp. 2224-2227, 1995

14. G. M. H. Knippels, A. F. G van der Meer, R. F. X. A. M. Mols, D. Oepts, P. W. van Amersfoort, D. A. Jaroszynski, "Influence of a step-tapered undulator field on the optical pulse shape of a far-infrared free-electron laser", *IEEE Journal Of Quantum Electronics*, 1996, Vol.32, No.6, pp.896-904.

15. G. H. C. van Werkhoven, "ELIXER, a simulation code for the spatial structure of light pulses in free-electron lasers", *Rijnhuizen report 95-226*, September 1995.

16. R. J. Bakker, D. A. Jaroszynski, A. F. G van der Meer, D. Oepts and P. W. van Amersfoort, "Short pulse effects in a free-electron laser", *IEEE Journal Of Quantum Electronics*, 1996, **30**, pp.1635-1644, 1994.

17. G. M. H. Knippels, R. F. X. A. M. Mols, A. F. G van der Meer, D. Oepts, and P. W. van Amersfoort, "Intense far-infrared free-electron laser pulses with a length of six optical cycles", *Phys. Rev. Lett.*, **75**, pp1755-1758, 1995

18. R. J. Bakker, G. M. H. Knippels, A. F. G van der Meer, D. Oepts, and P. W. van Amersfoort, "Dynamic desynchronisation of a free-electron laser resonator", *Phys. Rev. E*, 48, R3256-R3258, 1993.

19. S. Riyopoulos, *Phys. Plasmas I* 9, 3078 (1994).

20. A.E. Siegman, *Lasers*, University Science Books, Mill Valley (1986), p. 666

21. R.J. Bakker, C.A.J. van der Geer, D.A. Jaroszynski, A.F.G. van der Meer, D. Oepts and P.W. van Amersfoort, "Broadband tunability of a far-infrared free-electron laser", *J. Appl. Phys.*, vol. 74, pp. 1501-1509, 1993.

Chapter 5 Manipulation of the FEL gain medium

5.1   Introduction – energy and wavelength sweeps

The unique nature of the gain medium in an FEL—a relativistic electron beam—makes it possible to program the optical spectrum in a rather precise way by manipulating the electron beam energy during the electron macropulse. In this chapter an experimental investigation into the time-resolved spectral response of FELIX, on a microsecond time scale, to steps and linear sweeps in the electron energy is presented. The time resolved spectral output has been measured at several wavelengths and cavity desynchronisms. Sweep rates of up to 1.4 % per μs have been measured, indicating three orders of magnitude improvement over other reported results [7]. The investigation into the way in which the electron beam energy can be swept on a microsecond time scale has made it possible to produce given sweeps in wavelength—of up to 2%, limited only by the constraints of the electron beam transport system—which have been used by molecular spectroscopists to excite target molecules through an anharmonic ladder of states: the FEL is in effect made to operate as a voltage controlled optical oscillator with a response in the microsecond range.

There are several ways of controlling the wavelength of a FEL, each with its characteristic time scale. Tuning the wavelength by setting the accelerator to a new energy typically takes several tens of minutes because all elements of the beam line (bending magnets, quadrupole lenses, steering coils etc) have to be adjusted for that new energy. A faster and easier method of wavelength control is possible in those FELs which have an adjustable undulator field. The magnetic field strength is changed by varying the current in case of an electromagnetic undulator, or by adjusting the gap between the two opposing rows of magnets in case of a permanent-magnet undulator. The latter technique permits wavelength scans over an octave in one or two minutes [1].

Modulation of the electron beam energy at fixed settings of the beam line elements results in the fastest changes in radiation wavelength, albeit over a limited spectral range. In 1989, the FEL group at Los Alamos reported preliminary results for changes in the integrated optical spectral width when an energy slew of 0.5 % in 100 μs was applied to the electron beam, but no data on the temporal evolution of the spectrum were presented [2]. Electron energy modulation has been demonstrated experimentally at Stanford University and resulted in wavelength changes of 1 % on a millisecond time scale [3,4]. In the Stanford FEL, which is driven by a superconducting accelerator, the gain per pass is rather low and the FEL operates just above threshold due to the limited current that can be delivered. However, the current can be sustained over hundreds of milliseconds, thereby providing enough time for the laser to reach saturation. The low gain is responsible for the slow (millisecond) time response of the FEL in Stanford, in contrast to the FEL at Los Alamos. This FEL was driven by a room-temperature accelerator which delivering a much higher beam current and, therefore, has a much larger gain per pass. Theoretical work

describing the effect of a change in electron energy on the FEL wavelength and gain has been done by a number of groups, and several mechanisms for wavelength shifting have been identified [5,6].

Studies of fast wavelength shifting have been motivated by the fact that it allows users to operate the FEL as a voltage-controlled optical oscillator (VCOO) [3], with facilities similar to those available in a conventional electronic voltage-controlled oscillators at kHz and MHz frequencies. A scan in wavelength can be programmed by applying an appropriate waveform to modulate the electron energy. Experiments for which this is desirable include the resonant excitation of molecular systems: the anharmonic ladder of vibrational modes can be climbed efficiently by tuning the laser wavelength to the resonant value during the excitation process, provided that the time scale on which the FEL wavelength is swept is faster than the lifetimes of the excited states. Recent work by the molecular dynamics group at FELIX is putting this technique to good use.

5.2 Theoretical background

Changing the wavelength by modulation of the beam energy involves some interesting FEL physics. The processes involved in shifting the wavelength depend on, e.g. the presence of sidebands in the optical spectrum of the FEL [9] and on "lethargic start-up" (see Chapter 1). Sidebands in the optical spectrum can serve as seed field for the new wavelength corresponding to the shifted electron energy. To overcome this lethargic start-up, the cavity is shortened slightly. The resulting cavity desynchronisation advances the peak of the optical pulse with respect to the peak of the next electron bunch at the moment it enters the undulator, and hence restores the gain. When the optical field intensity saturates, amplification stops and, on successive round trips, the optical pulse moves away from the electron bunch due to the applied cavity desynchronisation. This reduces the overlap between the optical pulse and the electron bunch. The FEL thus can be operated in two regimes, depending on the cavity desynchronisation ΔL. A large ΔL results in a large small-signal gain and a fast start-up, but the reduced overlap at saturation results in a low saturated power. A small value of ΔL results in a slow growth, but a higher saturated power is reached.

FELIX is characterised by an electron bunch length that is smaller than the slippage distance. In such a short-pulse FEL, wavelength shifting via the so-called chirp-by-creep mechanism is important [2,5,7]. It is based on the finite interaction time between the optical pulse and an electron bunch as they travel through the undulator. When a sweep in the electron energy is applied, the energy of the electron bunches that enter the undulator changes from round trip to round trip although the energy of one bunch remains constant. The radiation wavelength will try to adapt to this new energy. At saturation it is difficult for the electrons to change the wavelength of the optical field because of the large field amplitude, so only electrons that have slipped away from the optical pulse can easily generate radiation at a new wavelength. The electrons at the trailing edge of the electron bunch have slipped away when they reach the last stage of the undulator, and since the strong optical field has bunched them efficiently in the first part of the undulator they generate coherent emission near the trailing edge of the optical

pulse [2]. On successive round trips the new wavelength moves forward in the optical pulse by a distance equal to the applied cavity desynchronisation, and is amplified to saturation. The measured change in centre wavelength in the Stanford FEL has been described quantitatively by this chirp-by-creep mechanism [7].

It is interesting that besides a shift in centre wavelength, a frequency chirp will be generated over each individual micropulse. The magnitude of the frequency chirp is expected to depend strongly on the applied cavity desynchronisation. The chirp-by-creep process thus offers a way to produce optical pulses which are chirped on a picosecond time scale, and indeed this has been reported elsewhere [8].

5.3 Experimental set-up

The pulsed electron beam in FELIX is produced by a thermionic triode gun [11]. A bias voltage on the grid between the cathode and the anode permits the electrons to pass through the grid. The bias voltage consists of a 1 GHz voltage added to a constant offset voltage, in order to emit electron bunches at this frequency. The opening angle of the gun is changed by changing the offset voltage. This changes the charge in each electron bunch. After acceleration to a relativistic energy (14 - 46 MeV) by a room-temperature radio-frequency linear accelerator (linac), the electron beam is injected into the undulator of FEL-2.

In these experiments the energy U of the electron beam is swept. In the experiments on the Stanford FEL the energy was changed by changing the RF-power fed into the linac [4]. A different approach, based on the beam-induced field in the linac, is used here. The beam-induced field is proportional to the average current in the beam and counteracts the accelerating field [12]. To control the charge per bunch and thus the average beam current, the offset voltage on the grid is changed. A decrease of this voltage leads to an increased opening angle. This increases the current drawn from the gun, which in turn increases the beam-induced field in the linac. The resulting energy of the electron beam at the linac exit is therefore decreased. In a similar way, an increase of the grid voltage leads to an increase of the beam energy. The rate at which U can be varied is determined by the characteristic filling time of the accelerating structures. In the case of a travelling-wave linac, as used in FELIX, the filling time τ is given by $\tau = L/v_g$, where L is the length of the accelerating structures (3.15 m) and v_g is the group velocity of the RF-wave in the structures ($9.3 \cdot 10^6$ m/s) [13]. These values lead to a filling time of $\tau = 0.34$ μs.

Under normal operation the current drawn from the gun shows a droop, caused by thermal effects in the solid-state amplifier which provides the 1 GHz RF-power to the grid. This droop in current is removed electronically by an appropriate correction pulse, applied to the offset voltage of the grid [13]. The electronics generating these correction pulses were used in the experiment to generate a step or a linear sweep on the electron energy.

The electron bunches are injected into the optical cavity by means of a achromatic bending system [13]. The bending system consists of two dipole magnets separated by 3 metres. Between the dipoles there is a quadrupole triplet. Although the bending system as a whole is (close to) achromatic, there is dispersion in the bend itself. An energy sweep on the electron beam will therefore influence the position of the beam in this dispersive part. The dimensions of the vacuum tube in the bending section limit the maximum energy sweep to 1.2 %.

Furthermore, the sweep in energy causes variations in the position and shape of the electron beam in the undulator. These are due to the small residual lack of achromaticity of the bending system caused by imperfect alignment of the electron beam and the transport system. These variations adversely influence the overlap between the optical beam and the electron beam. The variations in transverse electron beam position were observed on a fluorescent screen that was put in the undulator, and are typically a few millimetres at the largest energy steps. Another complication involves the fact that the phase of the RF-field in the linac changes due to the beam-induced field. This phase change influences the time at which the electron bunches enter the undulator, thereby changing the synchronism with the optical pulses.

After the electrons have passed through the undulator they are bent out of the cavity and are analysed with the energy spectrometer system described in Chapter 2. The optical power spectrum is monitored with a spectrometer (SpectraPro VM-504, Acton Research, Massachusetts) and a 48-channel pyroelectric detector array. The macropulse (optical power envelope) was measured with a pyroelectric detector, which has a response time of roughly 100 ns. The optical diagnostics were evacuated to avoid absorption of the infrared laser light by ambient water vapour.
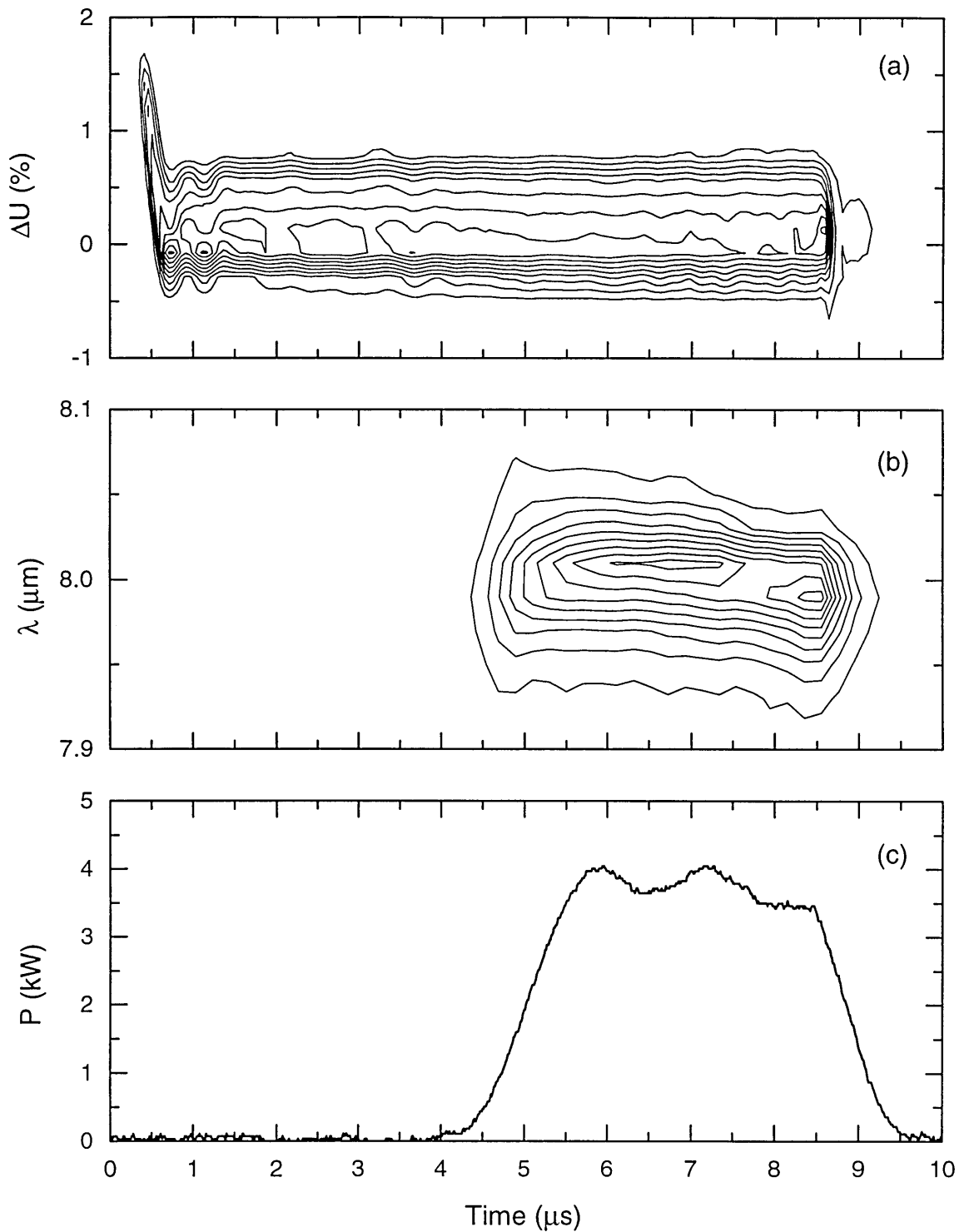
Figure 5.1 *Time-resolved electron spectrum recorded after the undulator, without laser interaction (a), time-resolved optical spectrum with laser interaction (b), and the corresponding power envelope (c). The laser interaction has been switched off in case (a) by applying a large cavity desynchronisation ($\Delta L > 200\ \mu m$). In (b) the cavity desynchronisation was set to $\Delta L = -16\ \mu m$. The central energy in (a) corresponds to 46 MeV. The phases of the linear accelerators were not set for the smallest possible energy spread but for optimal lasing performance with respect to power, resulting in a spectral width of 0.7 % (fwhm). The contours in (a) and (b) represent steps of 10 % in intensity*

5.4 Operation with a fixed electron energy

Before investigating the performance of FELIX as a VCOO, the optical and electron spectra at a fixed electron energy were measured. In Figure 5.1(a), the time-resolved electron spectrum is shown as measured after the undulator, without a laser field in the cavity. The absence of the laser field is achieved by desychronising the cavity in such a way that there is no overlap between electron pulses and the spontaneous emission from the electrons. A transient is seen in the electron energy at the start of the pulse, due to the beam-induced field in the linac. After the transient, the energy spectrum is stable to within 0.1 % and has a width of approximately 0.7 % (FWHM). Note that the phases of the RF-fields in the linacs were not optimized for obtaining the narrowest energy spectrum (in which case an rms-width of 0.2 % is possible) but for maximizing the laser power [14]. The optical spectrum at a cavity desynchronisation of ΔL = -16 µm was recorded at a wavelength of 8.2 µm. This optical spectrum and the corresponding (wavelength-integrated) macropulse are shown in Figure 5.1(b,c). The width of the optical spectrum, 0.7 % (FWHM) in case of Figure 5.1(b), can be adjusted between 0.5 % and 2.5 % by changing the cavity desynchronisation. Note that the electron macropulse appears to be longer than the optical macropulse, since the optical macropulse has to grow typically eight orders of magnitude from spontaneous emission before it is visible with our pyrodetector. The 4.5 µs needed for this growth indicates a net gain of the order of 19 % per round trip. The average power in the macropulse is 4 kW. Second-order autocorrelation measurements performed at this wavelength (not shown here) show short bandwidth-limited micropulses [15]. From the optical spectral width we therefore deduce a 2.0 ps (FWHM) long micropulse. The pulse energy is 4 µJ and the corresponding peak power in such a micropulse is 2 MW.

5.5 Steps and sweeps in the electron energy

In Figure 5.2 the step in the electron beam energy that is applied during the macropulse is shown. The step in the voltage on the grid of the electron gun is applied at the moment indicated by the arrow. The amplitude of the step can be controlled by changing the amplitude of the pre-programmed waveform. In practice, the maximum amplitude of the step in energy is limited to 1.2 % by the dimensions of the vacuum tube in the bending section, as mentioned earlier. The rise time (10/90 %) was measured to be 0.7 %/µs.

To minimise the effect of the variations in position and shape of the electron beam in the undulator, an initial series of measurements was taken with a small step up in energy of 0.5 %. It was not possible to make equally sized steps in both directions because of the droop present on the energy (see section 5.3), so a different series of measurements was taken with a step down in energy of 0.9 %. The optical spectrum and the power envelope were recorded at λ = 8.2 µm for various cavity desynchronisations.
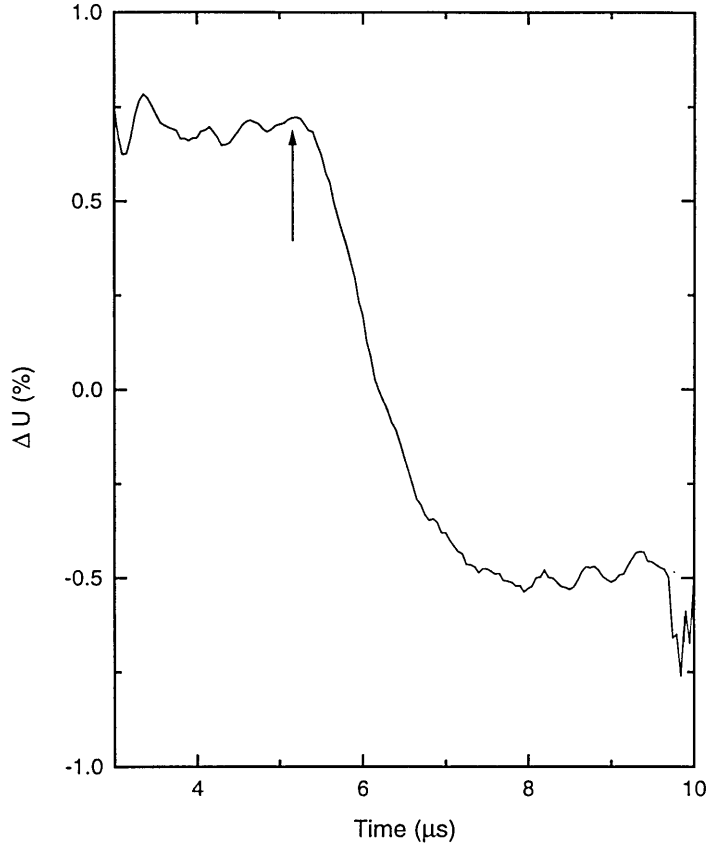
Figure 5.2 *Change in mean energy of the electron beam* $\Delta\overline{U}$ *versus time in the macropulse when the step in grid voltage is applied (at the moment indicated by the arrow). The rise time (defined by the 10/90 % level) was 0.7 %/μs. The rise time is determined by the filling time of the accelerating structures. The maximum amplitude of the step is 1.2 %, limited by the vacuum-tube dimensions in the bending system of our beam line.*

The results are shown in Figure 5.3. The step is applied in these measurements at t = 4.4 μs. It follows from the FEL resonance condition $\lambda \propto \gamma^{-2}$ that a step down in energy will lead to a step up in wavelength that is expected to be twice as large since $\Delta\lambda/\lambda = -2\Delta\gamma/\gamma$. The optical spectrum is broader for small ΔL, as shown in Figure 5.3 (a) and (d). In these cases the step in centre wavelength is small compared to the instantaneous spectral width. However, for large desynchronisations, where the spectral width is small (Figure 5.3(c) and (f)), the step in centre wavelength is larger than the spectral width. This shows that the FEL can be swept well outside its spectral bandwidth. When the step in energy is applied, the laser has to restart on that new energy. The time that the FEL needs to reach saturated power at this new energy depends on the gain per pass and the amount of seed field that is present at the new wavelength. At large cavity desynchronisations, the net gain per pass is relatively high (19 % in Figure 5.3(c) and (f)), but the seed field at the new frequency is small because of the limited spectral width. At small desynchronisations the spectral width is larger and the gain per pass is somewhat lower (16 % in Figure 5.3(a) and (d)). The differences between the step up in energy (a-c)

and the step down in energy (d-f) are mainly due to the fact that the steps cannot be made equally large. In Figure 5.3(d)-(f) the steps are much larger (0.9 %) so that there is less seed field present at the new wavelength than in Figure 5.3(a)-(c) and so the power of the FEL decreases on application of the step.

A similar series of measurements was performed at a wavelength of 20 μm with the same steps in electron energy, as shown in Figure 5.4. At 20 μm the gain per pass is higher (27% in Figure 5.4 (c) and (f)) compared to the measurements taken at 8.2 μm wavelength. Also at this longer wavelength the instantaneous spectral width can be tuned up to 6 %, by adjusting the cavity desynchronisation. Due to the larger gain and large seed fields at the new wavelength, the response of the FEL shows no decrease in macropulse power in Figure 5.4 (a)-(c) and very little in Figure 5.4 (d)-(f).

Results for the largest possible step in energy (1.2 %) as limited by the vacuum-tube dimensions in the bending section, are given in Figure 5.5, for both $\lambda = 8.2$ μm and $\lambda = 20$ μm. Only the results for a step down in energy are given. The step is so large that, due to transverse position variations of a few millimetres in the electron beam position in the undulator, there is loss of overlap between the stored optical beam and the electron beam. Since the transverse optical beam size is smaller at 8 μm (the waist area at 8 μm is calculated to be 13 mm² compared to 30 mm² at 20 μm), the loss of overlap is expected to be more pronounced at this wavelength than at 20 μm. This is responsible for the observation that the FEL stops lasing in the low-gain case plotted in Figure 5.5(a). At the new wavelength it has to restart from a level which is not detectable by the spectrometer. At 20 μm the effect of position variations is less pronounced, see Figure 5.5(d)-(f). However, compared to Figure 5.4 (a)-(c) a stronger influence of the cavity desynchronisation is observed: this is due to the fact that the larger step (1.2 % versus 0.5 %) in energy makes the FEL more sensitive to the amount of seed field in the wings of the spectra.

An almost linear ramped electron beam energy can be produced when a different pre-programmed waveform is used, as shown in Figure 5.6(a). Again the laser interaction has been switched off to prevent distortion of the electron spectrum by the optical field. The optical response of the FEL is given in Figure 5.6(b) for $\lambda = 20$ μm. A sweep rate of 0.45 %/μs was achieved and a total sweep of 2.0 % was measured. In this case, taken at $\Delta L = -40$ μm, the total sweep is larger than the instantaneous spectral width of 0.66 % (FWHM).
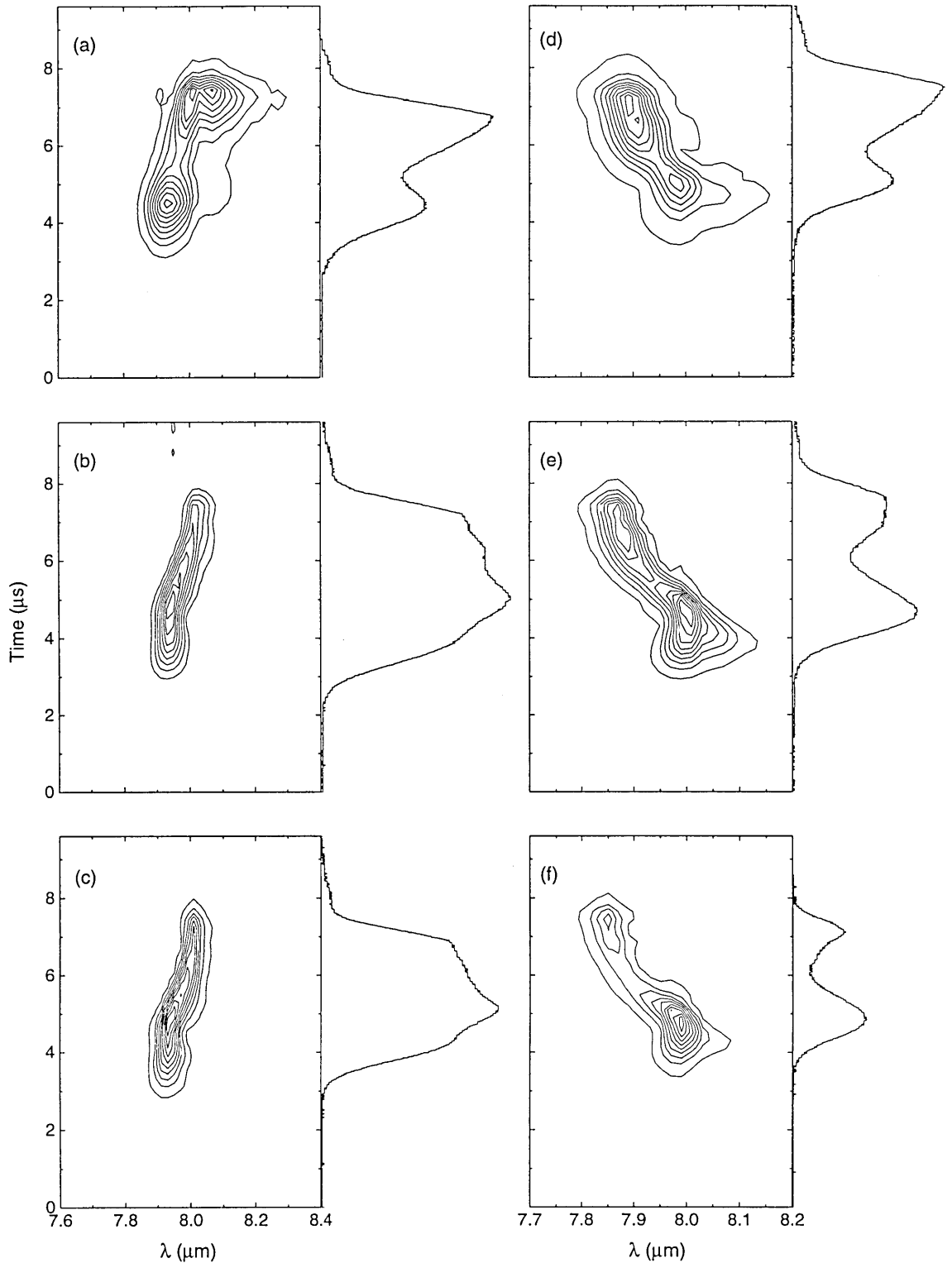
Figure 5.3 *Time-resolved optical spectra at λ = 8.2 μm and the corresponding (wavelength-integrated) power envelope when a step in energy is induced. Figures (a-c) correspond to three different cavity desynchronisations when a step up in energy of 0.5 % is applied. The measurements in (d-f) are for a 0.9 % step down in energy. In all cases the step is applied at 4.4 μs. The cavity desynchronisations are respectively ΔL = -5 μm for (a) and (d), ΔL = -11 μm for (b) and (e), ΔL = -20 μm for (c) and (f). The net gain per pass ranges from 16 % in (a) and (d) to 19 % in (c) and (f). The contours represent steps of 10 % in intensity. The macropulses on the right-hand sides of (a-f) are plotted to scale*
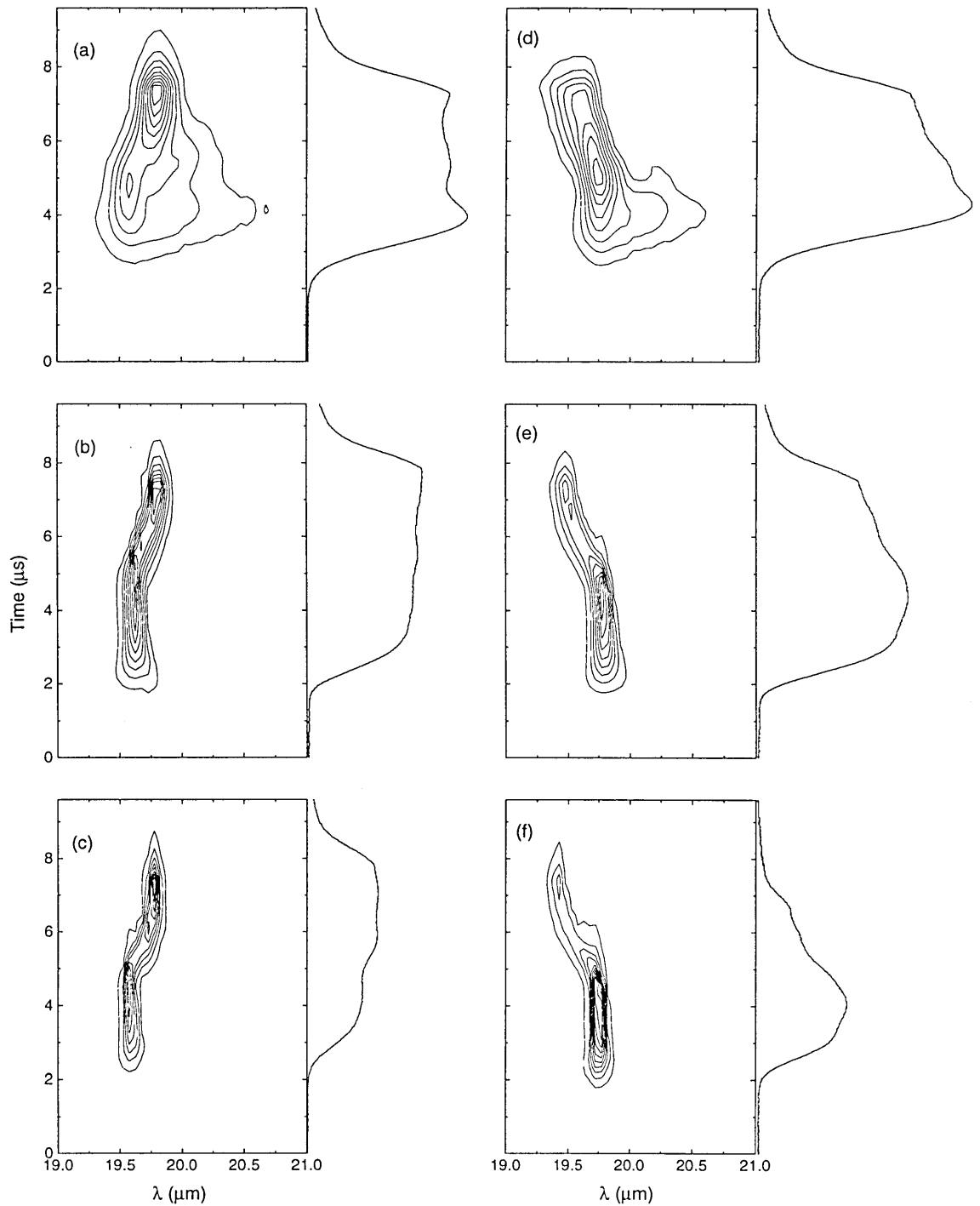
81

Figure 5.4 *Time-resolved optical spectra at λ = 20 μm and the corresponding (wavelength-integrated) power envelope when a step in energy is induced. Figures (a-c) correspond to three different cavity desynchronisations for a step up in energy of 0.5 %. The measurements in (d-f) are for a 0.9 % step down in energy. In all cases the step is applied at 4.4 μs. The cavity desynchronisations are respectively ΔL = - 10 μm for (a) and (d), ΔL = -30 μm for (b) and (e), ΔL = -60 μm for (c) and (f). The net gain ranges from 17 % in case (a) and (d) to 27 % in (c) and (f). The contours represent steps of 10 % in intensity. The macropulses in (a-f) are plotted to scale.*
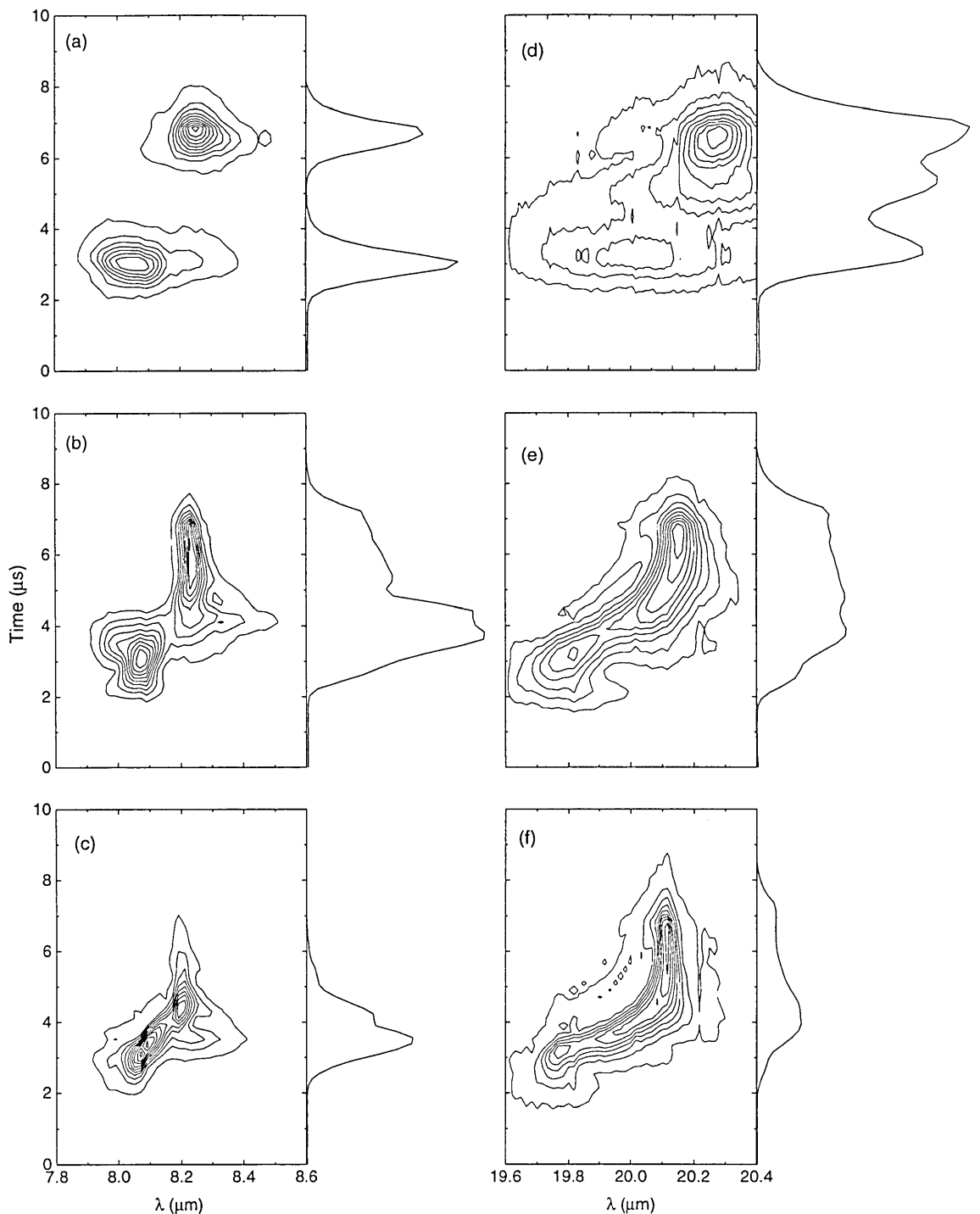
Figure 5.5 *Time-resolved optical spectra and the corresponding (wavelength-integrated) power envelopes when a step down in energy of 1.2 % is induced. Fig. (a-c) correspond to three different cavity desynchronisations at a wavelength of λ = 8.2 μm, and Fig. (d-f) correspond to three desynchronisations at a wavelength of λ = 20 μm. The cavity desynchronisms for case (a) to (f) are respectively, ΔL = -6 μm, -13 μm, -24.5 μm, -10 μm, -30 μm and -61.4 μm. A sweep rate of up to 1.4 %/μs is measured in case (f). The contours represent steps of 10 % in intensity. The macropulses in (a-c) and in (d-f) are plotted to scale.*
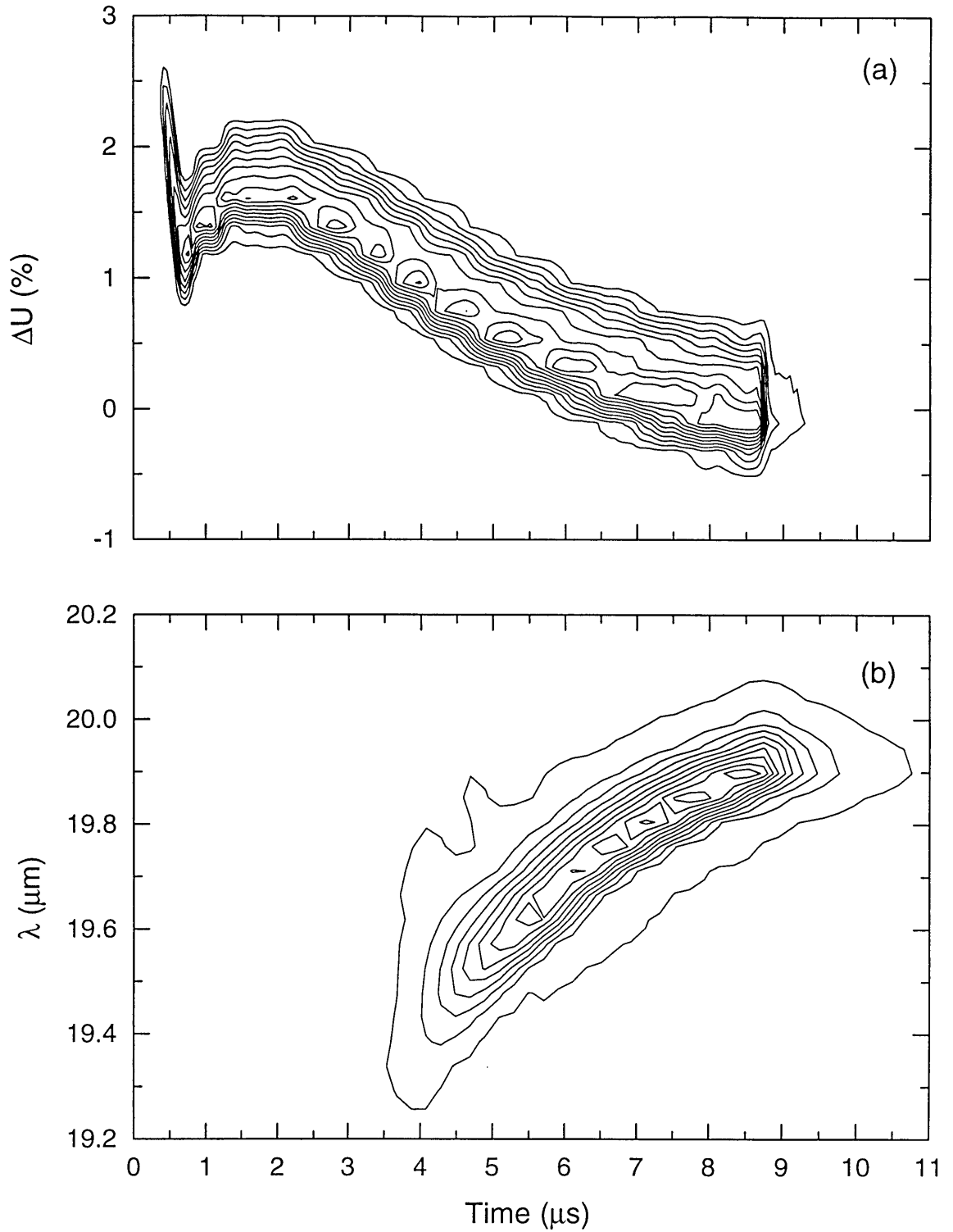
Figure 5.6 *Generation of a linear ramp: time-resolved electron spectrum (a), when laser interaction is switched off by desynchronising the cavity, and the time-resolved optical spectrum at λ = 20 μm (b). The central energy corresponds to 46 MeV. The observed islands in the electron spectrum are artefacts, due to the finite width of the discrete channels in the spectrometer. In case (b) a cavity desynchronisation of ΔL = -40 μm is applied, resulting in an instantaneous spectral width of 0.66 % (fwhm). The measured wavelength sweep rate in (b) is 0.45 %/μs. The total wavelength sweep is 2.0 %. The contours in (a) and (b) represent steps of 10 % in intensity.*

5.6 FELIX as a voltage-controlled optical oscillator

In conclusion, operation of FELIX as a VCOO makes it possible to program far-infrared wavelength scans on a microsecond time scale, limited by the finite acceptance of the electron beam line and the loss of overlap (and possibly loss of synchronisation) of the optical pulses and the electron beam in the undulator. Maximum sweep rates of 1.4 %/μs have been obtained at 20 μm wavelength, with total sweeps of up to 2.0 %. The limited number of pre-programmed functions that can be applied will be extended in the near future by an arbitrary waveform generator. The larger gain per pass, larger optical beam size, and larger instantaneous spectral widths present at long wavelengths, make the process more effective at these wavelengths

5.7 References

1. R.J. Bakker, C.A.J. van der Geer, D.A. Jaroszynski, A.F.G. van der Meer, D. Oepts and P.W. van Amersfoort, *J. Appl. Phys.* **74**, 1501 (1993).

2. R.W. Warren, J.E. Sollid, D.W. Feldman, W.E. Stein, W.J. Johnson, A.H. Lumpkin and J.C. Goldstein, *Nucl. Instrum. & Methods Phys. Res.* **A285**, 1 (1989).

3. T.I. Smith and H.A. Schwettman, *Nucl. Instrum. & Methods Phys. Res.* **A304**, 812 (1991).

4. R.L. Swent, K.W. Berryman, H.A. Schwettman and T.I. Smith, *Nucl. Instrum. & Methods Phys. Res.* **A304**, 272 (1991).

5. R.K. Wong and W.B. Colson, *Phys. Rev. E* **52**, 981 (1995).

6. G. Shvets and J.S. Wurtele, *Phys. Plasma I*, **1** 157 (1994).

7. A. Marziali, T.I. Smith and H.A. Schwettman, *Nucl. Instrum. & Methods Phys. Res.* **A358**, 252 (1995).

8. G. M. H. Knippels, PhD thesis Chapter 7, Vrije Universiteit, Amsterdam (1996).

9. B.A. Richman, J.M.J. Madey and E.B. Szarmes, Phys. Rev. Lett. 63, 1682 (1989).

10. R.J. Bakker, D.A. Jaroszynski, A.F.G. van der Meer, D. Oepts and P.W. van Amersfoort, IEEE J. Quantum Electron. 30, 1635 (1994).

11. R.J. Bakker, C.A.J. van der Geer, A.F.G. van der Meer, P.W. van Amersfoort, W.A. Gillespie and G. Saxon, Nucl. Instrum. & Methods Phys. Res. A307, 543 (1991).

12. J.E. Leiss, in *Particle Accelerators*, edited by P.M. Lapostolle and A.L. Septier, North-Holland Publishing Company, Amsterdam (1970), page 147.

13. C.A.J. van der Geer, R.J. Bakker, A.F.G. van der Meer, P.W. van Amersfoort, W.A. Gillespie, G. Saxon and M.W. Poole, Nucl. Instrum. & Methods Phys. Res A334, 607 (1993).

14. A.F.G. van der Meer, R.J. Bakker, C.A.J. van der Geer, D. Oepts, P.W. van Amersfoort, W.A. Gillespie, P.F. Martin and G. Saxon, Nucl. Instrum. & Methods Phys. Res. A331, 282 (1993).

15. G.M.H. Knippels, A.F.G. van der Meer, R.F.X.A.M. Mols, P.W. van Amersfoort, R.B. Vrijen, D.J. Maas and L.D. Noordam, Opt. Commun. 118, 546 (1995).

16. G. Dattoli and A. Renieri, "Experimental and theoretical aspects of the free-electron laser" in *Laser Handbook Vol. 4*, edited by M.L. Stitch and M. Bass, North-Holland, Amsterdam, pp 1-133 (1985).

Chapter 6 Superradiance in the FEL

6.1 Introduction

Further evidence for the recent observation of superradiance in an FEL oscillator [7] has been provided by an investigation which shows that the efficiency and intracavity power of the radiation scale respectively as the inverse square root and the inverse square of the cavity losses, verifying the superradiant scaling laws predicted by the supermode theory [5]. Furthermore these scaling laws are shown to be a direct consequence of the short optical pulse lengths which have been observed. The practical importance of this is that the superradiant scaling laws indicate that increasing the bunch charge and reducing the cavity losses may allow the operating parameters of FELIX to be improved from six cycle optical pulses with an energy of several tens of microjoules towards single cycle pulses with energies of the order of half a millijoule. These pulses would have peak powers of many gigawatts – corresponding to intracavity powers that approach the terawatt level.

In 1954 Dicke [1] showed that the most efficient way of extracting energy from an inverted two-level atomic system is through co-operative emission where the radiation rate is enhanced by the mutual interaction of radiators through a common radiation field produced by neighbouring radiators. This enhanced rate, which Dicke termed the *superradiant rate*, is proportional to the number of emitters, n_e. In addition it was shown that such a system produces pulses of coherent radiation with a peak intensity scaling as the square of the number of emitters, n_e^2. The same phenomenon has been predicted to occur in FEL amplifiers [2,3]. More recently it has been shown theoretically that superradiance can occur in the FEL oscillator [4,5,6] and experimental observation of superradiance in a FEL oscillator was noted in [7] and [9].

For a Compton FEL in saturation, it can be shown that the peak power is expected to scale as $n_e^{4/3}$ with scaling as $n_e^{5/3}$ possible for a tapered undulator [10]. Radiation intensities scaling as n_e^2 may arise from coherent radiation emitted by electrons that have been pre-bunched by an external source, e.g. a strong laser field. The radiation fields emitted by such pre-bunched electrons sum up coherently to give an n_e^2 scaling. Strictly speaking this is the direct analogue of the Dicke definition of superradiance, viz. spontaneous emission from a coherently prepared system. A different phenomenon is observed in our experiment. The electrons enter the undulator in an unprepared state—unbunched and with no external input signal—so that the intensity of the emitted radiation is initially proportional to n_e. The electrons begin to bunch on interacting with the combined undulator and radiation fields and evolve to emit radiation with an intensity proportional to n_e^2: i.e. we observe radiation with a peak intensity scaling as n_e^2 and arising from a self-bunched system.

The experiment described in this chapter provides further evidence for the observation of superradiance in FELIX. Measured values of extraction efficiency and peak intra-cavity power are shown to depend on the cavity losses α as $\alpha^{-1/2}$ and α^{-2} respectively, as predicted in [7].

6.2 Theoretical background

It has been shown [5,6] that at small signal levels the optical pulse will evolve into a steady state shape characterised by the supermodes of the linear equations of motion. Following [7] the expression

$$\eta = \rho \sqrt{\frac{l_b}{\alpha l_c}}$$ is used for the maximum efficiency of an FEL close to zero desynchronism at

$$\Delta L = 0.18 l_b \left(\frac{\alpha l_c}{l_b}\right)^{\frac{3}{2}}.$$

$$\rho = \frac{g_0^{\frac{1}{3}}}{4\pi N_u}$$ is the FEL Pierce parameter,

$$g_0 = N_u^3 \gamma \frac{I_b}{I_A} \frac{\lambda}{z_R} f(a_u)^2$$ is the cw small signal gain coefficient [8],

I_b is the peak current,

$I_A \approx 17000$ A is the Alfven limit current,

z_R is the Rayleigh length for the optical cavity,

$$f(a_u) = 4\pi \frac{K}{1+K^2}(J_0(\xi) - J_1(\xi)) \text{ with } \xi = \frac{1}{2}\frac{K^2}{1+K^2} \text{ and } K \text{ the rms undulator strength,}$$

l_b is the bunch length,

$$l_c = \frac{\lambda}{4\pi\rho}$$ is the cooperation length

and α is the cavity loss per round trip.

Using the bunch charge $Q = I_b \dfrac{l_b}{c}$ we may write the efficiency as

$$\eta = \left(\frac{cQ}{I_A z_R}\right)^{\frac{1}{2}} \frac{K}{1+K^2}(J_0(\xi) - J_1(\xi))\gamma^{\frac{1}{2}}\alpha^{-\frac{1}{2}}. \qquad (6.2.1)$$

It should be noted that this represents the measured efficiency only if the optical pulse sweeps—due to slippage—through the whole electron pulse as the pulses co-propagate down the undulator. Where, as in this experiment, the slippage length is less than the bunch length, the calculated efficiency, η, is an "effective efficiency" representing the energy extracted only from the part of the electron bunch swept by the optical pulse. It is related to the "measurable efficiency", η', by $\eta' = \eta \dfrac{l_s}{l_b}$ where $l_s = N_u \lambda$ is the slippage length [7].

Following [7], the scaling relationships predicted by the supermode theory for the peak optical power and the extraction efficiency may also be derived from the assumption that at saturation the optical pulse has narrowed so that the electrons perform an oscillation in phase which is limited by the duration of the optical pulse. In this situation the optical pulse length is shorter than the slippage length (and the electron bunch length) so that electrons are only in contact with the optical field for part of the journey along the undulator as the optical pulse sweeps through the slippage distance. The scaling is derived by considering the energy interchange between an electron bunch and a single optical pulse—of length shorter than the electron bunch—as they propagate down the undulator.

Equation (4.3.2) for the modulus of the dimensionless complex field gives $|a| = (4\pi N)^2 \frac{K}{1+K^2}(J_0(\xi) - J_1(\xi))\frac{e\lambda E}{2\sqrt{2}\pi mc^2}$ so that at a fixed wavelength (which is here taken to mean fixed values of both K and γ) it can be seen that

$$|a| \propto E \qquad\qquad (6.2.2)$$

where, as before, E is the amplitude of the complex electric field envelope. Equation (4.4.2) shows that the efficiency η is proportional to $|a|^{1/2}$ so that

$$\eta \propto E^{1/2}. \qquad\qquad (6.2.3)$$

From equation (4.4.3) it follows that for peak intra-cavity power, P_o

$$P_o \propto E^2. \qquad\qquad (6.2.4)$$

The assumption necessary to generate the scaling rules is that the interaction time, which is determined by the pulse length τ, is a (fixed) fraction of the synchrotron oscillation period so that, from (4.3.1) $\tau \propto |a|^{-1/2}$ and thus

$$\tau \propto E^{-1/2}. \qquad\qquad (6.2.5)$$

The energy in the optical micropulse U_o is proportional to the product of P_o and τ so that

$$U_o \propto E^{3/2} \qquad\qquad (6.2.6)$$

and the energy in an electron bunch, $U_e = \gamma mc^2 \frac{Q}{e}$, where Q is the bunch charge, so that

$$U_e \propto Q.$$ (6.2.7)

Conservation of energy at saturation implies that the energy extracted from an electron bunch, ηU_e is equal to the energy removed from the optical micropulse due to out-coupling and cavity losses. Thus

$$\eta U_e = \alpha U_o = \alpha P_o \tau,$$ (6.2.8)

so that from (6.2.2), (6.2.6) and (6.2.5) $E \propto \dfrac{Q}{\alpha}$

and the scaling relationships for P_o and η follow immediately from (6.2.3) and 6.2.4):

$$\eta \propto \left(\frac{Q}{\alpha} \right)^{\frac{1}{2}}$$ (6.2.9)

and

$$P_o \propto \left(\frac{Q}{\alpha} \right)^2.$$ (6.2.10)

6.3   Electron and optical measurements

Measurements were made on FEL-2 with the beam current, beam energy and r.m.s. undulator strength, held constant at 198 mA, 40.6 MeV and 1.40 respectively, giving a constant bunch charge and a wavelength of 15.2 μm. The cavity losses were varied between 4% to 24% by inserting fine wires into the optical cavity. A fast HgCdTe detector was used to monitor the out-coupled infra-red radiation and determine the cavity losses per round trip α from the exponential decay of the optical signal after the electron beam was switched off. The optical pulse duration was measured using a zero background second-order autocorrelation technique (described in Chapter 4) and the data were fitted to a $\mathrm{sech}^2(t)$ pulse to give a FWHM pulse width τ. Values of τ between 600 fs and 1200 fs were obtained. Typical results are shown in Figure 6.1 giving $\tau = 633$ fs. For each measurement, the cavity desynchronism was adjusted to yield the maximum extraction efficiency which was measured using the electron spectrometer (see Chapter 2)
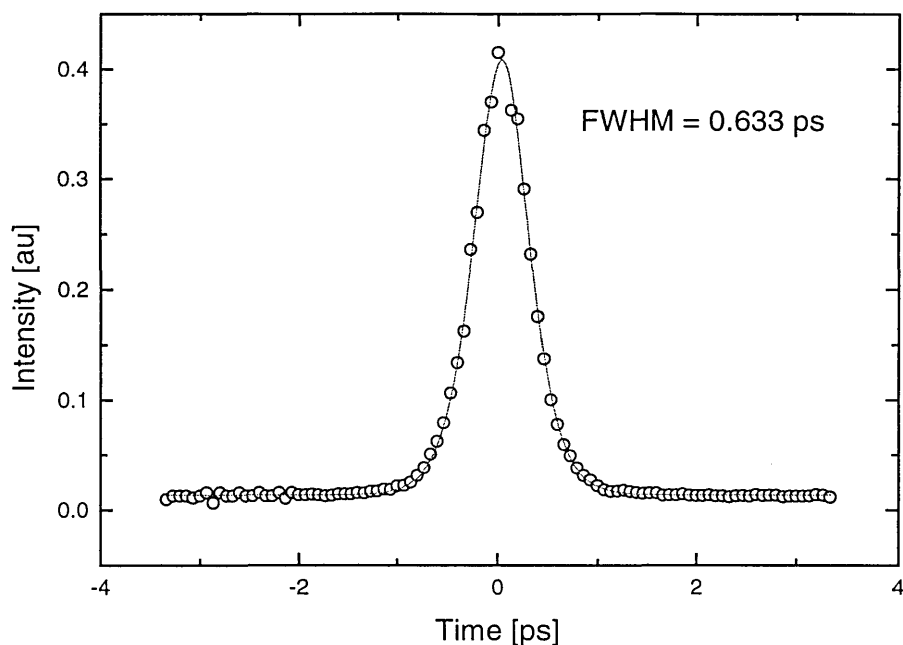
Figure 6.1 *A typical set of data from the autocorrelator for lasing at 15.2 μm, near zero desynchronisation and 4% cavity losses. The* $\mathrm{sech}^2(t)$ *curve fitted gives a FWHM of 633 fs.*

6.3.1 Measuring efficiencies at large energy spreads

It has already been noted (see 4.6) that operating FELIX under conditions which produce short optical pulses can lead to electron energy spreads which exceed the acceptance of the spectrometer. Such conditions may be easily detected from a graph of the electron beam intensity calculated from the electron spectrometer data. The electron beam intensity should remain constant throughout the beam pulse and so deviations from this indicate that some electrons are not being detected. Under conditions of severe energy spread, electrons leaving the spectrometer magnet strike the vacuum housing producing X-rays which cause a misleading rise in the detector output, as in Figure 6.2, which shows a contour plot of the electron energy distribution with a graph of the electron beam intensity above and on the same time-scale. The data up to 6 μs is certainly valid. Thereafter, from 6 μs to 7.5 μs the intensity starts to drop slightly—indicating electrons not being detected—before rising abruptly—due to X-ray production when the electrons strike the vacuum housing.

Figure 6.2 *A contour plot of the electron energy distribution with a graph of the electron beam intensity above and on the same time-scale. The data up to 6 μs are certainly valid. Thereafter, from 6 μs to 7.5 μs the beam intensity starts to drop slightly—indicating electrons not being detected—before rising abruptly—due to X-ray production when the electrons strike the vacuum housing.*
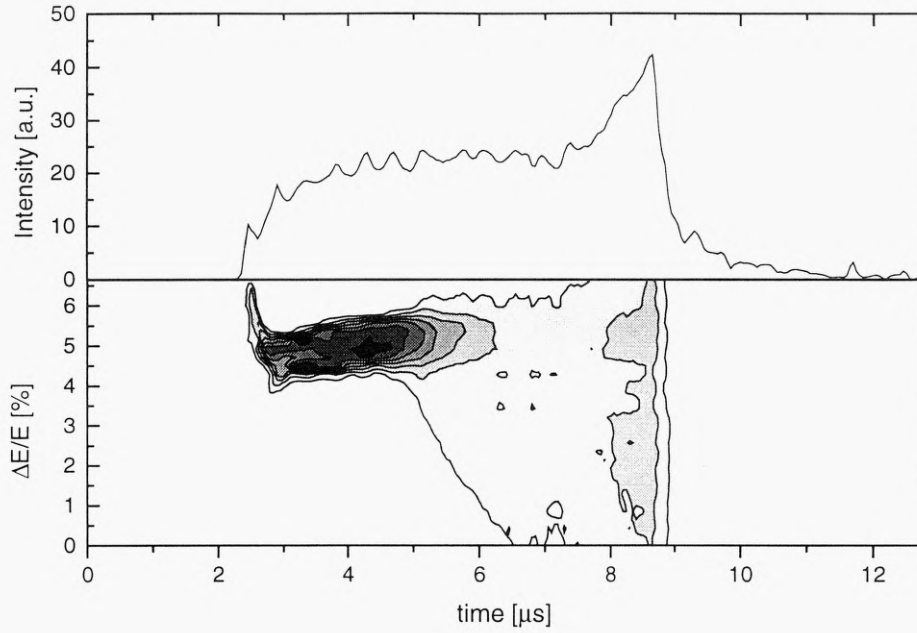
The consistency of the mean energy data and the optical power envelope data has already been demonstrated in section 4.2 (see particularly Figure 4.4). Using the reverse of this procedure, the mean energy data, and hence the extraction efficiency can be calculated up to an arbitrary—and as yet unknown—scale factor from the optical macropulse envelope $P(t)$ by evaluating the quantity $\frac{dP}{dt} + \alpha P$. However if a partially valid set of electron data is available, the scale factor can be determined by fitting $\frac{dP}{dt} + \alpha P$ to the valid portion of the electron mean energy data and thus allowing the extraction efficiency to be calculated even at energy spreads which greatly exceed the energy bite of the spectrometer. This procedure is illustrated for lasing with cavity losses per round trip $\alpha = 4\%$ and almost zero desynchronism in Figure 6.3. The reconstructed extraction efficiency curve indicates an efficiency of 2.3%.
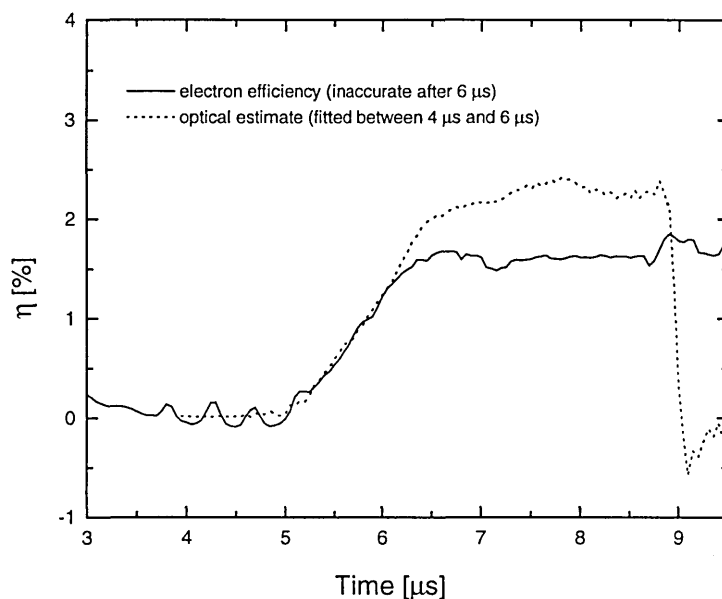
Figure 6.3 *Graphs of the extraction efficiency corresponding to the graphs in Figure 6.2—lasing at 15.2 μm, near zero cavity desynchronisation and 4.4% cavity losses. As indicated in Figure 6.2, the electron data after 6 μs are no longer valid. The solid line is the efficiency as calculated from the electron spectrometer data. The dotted trace is the efficiency as reconstructed from the optical data and scaled by fitting to the section of the electron data between 4 μs and 6 μs which is known to contain valid. The extraction efficiency peaks at 2.4%.*

Extraction efficiencies were calculated using this method in all cases, even when the electron spread was small enough to allow the electron data to remain valid throughout the macropulse. Good agreement between the 'direct' and 'optical' values was obtained in those cases, providing an important check on the consistency of the measurement system.

6.3.2 Efficiency and intracavity power as a function of cavity losses

The values of efficiency measured in this way are plotted as open circles in Figure 6.4 against the reciprocal of the square root of the cavity losses. The dotted line represents the 'effective' efficiency η (see section 6.2) and the solid line is the 'measurable' efficiency η' (see section 6.2) calculated using the parameters in Table 6-1. There is excellent agreement with the predicted values of measurable efficiency.

The peak intracavity power P_o has been calculated from the measured values of efficiency η and the measured optical pulse width τ using equation (6.2.8). The results are presented in Figure 6.5 which

shows in (a) $\eta \propto \alpha^{-1/2}$ and in (b) $P_o \propto \alpha^{-2}$ confirming the superradiant scaling laws (equations (6.2.9) and (6.2.10)) for these quantities with the cavity losses α.

Table 6-1 *The data presented Figure 6.4 were taken under the following conditions:*

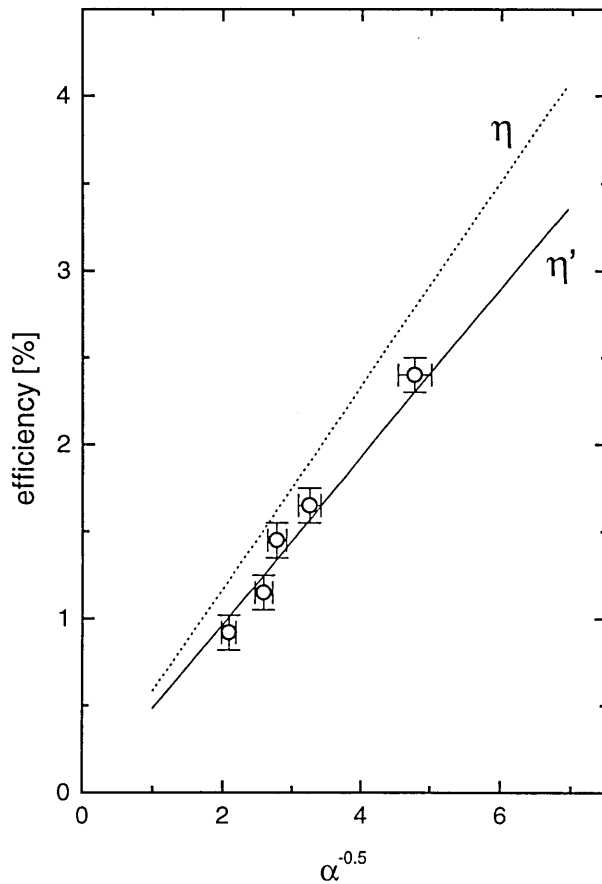|		
γ	Lorentz factor	80
α	Percentage cavity losses	4.4, 9.5, 13, 15,24
Q	Bunch charge	200 pC
z_R	Cavity Rayleigh length	1.2 m
λ	Optical wavelength	15.2 μm
N_u	Number of undulator periods	38
l_s	Slippage length	0.58 mm
l_b	Estimated bunch length	0.8 mm

Figure 6.4 *Measured values of efficiency are plotted as open circles against the reciprocal of the square root of the cavity losses. The dotted line represents the 'effective' efficiency η, and the solid line is the 'measurable' efficiency η' defined in section 6.2 and calculated using the parameters in Table 6-1.*
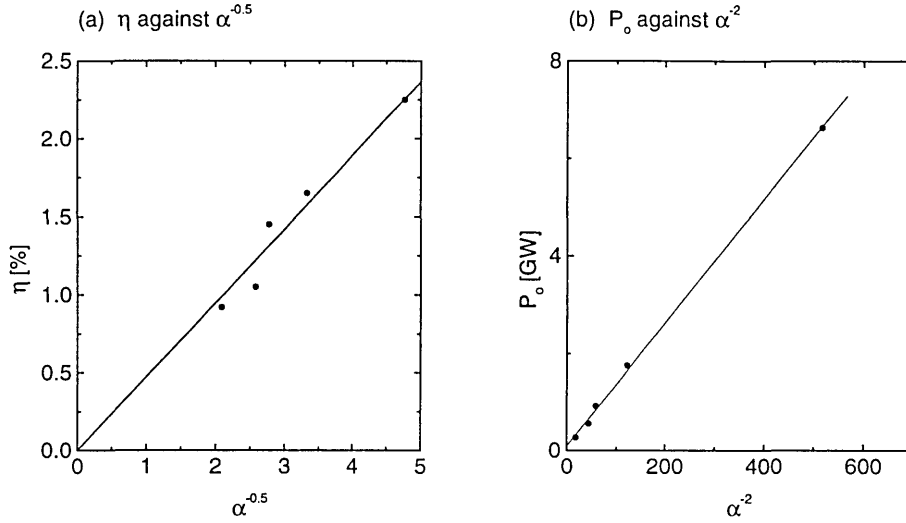
(a) η against $\alpha^{-0.5}$

(b) P_o against α^{-2}

Figure 6.5 *(a)* η *against* $\alpha^{-1/2}$ *and (b)* P_o *against* α^{-2} *at a wavelength of 15.2 µm , near zero desynchronisation, constant bunch charge and a beam energy of 40.6 MeV.*

6.4 Conclusions

It has been demonstrated that the superradiant regime can be reached in a free-electron laser oscillator and is not a phenomenon confined to the high gain FEL amplifier. A simple derivation of the superradiant scaling laws (equations (6.2.9) and (6.2.10)) for extraction efficiency and peak intracavity power has been presented. The derivation is based on the assumption that the electrons interact with the optical pulse for a period limited by the duration of the optical pulse, and the measurements of the optical pulse-width indicate that this is indeed the case. These ultra-short optical pulses have been shown to have a peak intensity that scales as the inverse square of the cavity losses and energy is extracted with an efficiency scaling as the inverse square root of the cavity losses. The results presented complement those in [7] where experimental data supporting the variation with bunch charge Q is presented.

Current work to improve our understanding of the phenomenon of superradiance in FELIX is proceeding by developing a technique which will probe the optical *micropulse* with unprecedented resolution: we already have results with better than 100 fs resolution and we hope soon to have 10 fs resolution [11]. The same probing technique, applied either to transition radiation from the electron beam or directly to the electric field intensity generated by the electron bunch itself, will provide, for the first time, longitudinal information about the electron bunch length and shape.

6.6 References

1. R. Dicke, *Phys Rev*, **93**, 99, (1954)

2. R. Bonifacio and F. Casagrande, "Classical and quantum treatment of amplifier and superradiant free-electron laser dynamics", *J. Opt. Soc. Am. B*, **2**, 250, (1985)

3. R. Bonifacio, B. W. J. McNeil, P. Pierini, "Superradiance in the high-gain free-electron laser", *Phys. Rev A*, **40**, 4467 (1989)

4. G. T. Moore and N. Piovella, "Superradiant short-pulse propagation in the free-electron laser-oscillator", *IEEE J. Quant. Elec.*, **27**, 2522 (1991)

5. N. Piovella, P. Chaix, G. Shvets and D. A. Jaroszynski, "Analytical theory of short-pulse free-electron laser oscillators", *Phys. Rev. E.*, **52**, 5470 (1995)

6. N. Piovella, "Transient regime and superradiance in a short-pulse free-electron-laser oscillator", *Phys. Rev. E*, **51**, 5147 (1995)

7. D. A. Jaroszynski, P. Chaix, N. Piovella D. Oepts, G. M. H. Knippels, A. F. G. van der Meer and H. H. Weits, "Superradiance in a short-pulse free-electron laser", *Phys. Rev. Lett.*, **78**, 1699 (1997).

8. W. B. Colson, "Classical Free electron theory", in *Laser Handbook Vol 6,* edited by W. B. Colson, C. Pellegrini and A .Renieri, North-Holland, Amsterdam, pp 115-194, 1990.

9. A. M. MacLeod, W. A. Gillespie, D. A. Jaroszynski and A. F. G. van der Meer, "Cavity losses and extraction efficiencies in a short-pulse free-electron laser", *Nucl. Inst. and Meth. in Phys. Res. A*, **407**, II-41 (1998)

10. R. Bonifacio et al. "Physics of the high-gain FEL and superradiance", *Il Nuovo Cimento*, **13**, No. 9 (1990).

11. G. .M. H. Knippels, A. F. G. van der Meer, M. J. van de Pol, X. Yan, A.M. MacLeod, W. A. Gillespie, C. W. Rella "FEL pulse shape measurements with 100 fs temporal resolution using a 10 fs Ti:Sapphire laser and differential optical gating", Proceedings of the 20th International free-electron laser conference, Williamsburg, VA. (1998) to be published in *Nucl. Inst. and Meth. in Phys.*

Chapter 7 Closing remarks

7.1 Achievements

The design, implementation and commissioning of a time-resolved electron energy spectrometer system have been discussed. Since its installation at the FELIX free-electron laser user facility in Nieuwegein, The Netherlands, the spectrometer system has been in regular use as a diagnostic and investigative tool. The system provides 0.2% energy resolution with 32 channels, and time resolution of 50 ns. The energy bite of the system is optically adjustable between 2% and 8%. The spectrometer is positioned immediately following the undulator of the free-electron laser (FEL) so that the gain medium—the relativistic electron beam—can be probed immediately following its interaction with the optical field in the laser cavity. Furthermore, by widening the undulator gap to make the on-axis magnetic field effectively zero, or by desynchronising the laser cavity, the raw, non-lasing, electron energy spectrum may also be obtained. The system permits real-time calculation and graphical display of key beam parameters as well as the archiving of raw data, and has been used to provide insight into the operation of an FEL in the high slippage, short pulse regime. In particular, direct measurement of the extraction efficiency is possible from macropulse to macropulse.

A systematic study of efficiency as a function of wavelength and cavity desynchronisation has been undertaken, the results of which agree well with the values expected from conventional theory at moderate values of cavity desynchronisation. At low values of cavity desynchronisation the efficiencies measured exceed the conventional $1/2N$ estimate by between 50% and 100% and these results are shown to be consistent with the formation of the ultrashort optical pulses—in the region of 6 optical cycles in length—which have been observed experimentally using a second-order autocorrelator. An investigation into the way in which the electron beam energy can be swept on a microsecond time scale has made it possible to produce given sweeps in wavelength—of up to 2%, limited only by the constraints of the electron beam transport system—which have been used by molecular spectroscopists to excite target molecules through an anharmonic ladder of states: the FEL is in effect made to operate as a voltage-controlled optical oscillator. Further evidence for the recent observation of superradiance in an FEL oscillator has been provided by an investigation which shows that the efficiency and intracavity power of the radiation scale respectively as the inverse square root and the inverse square of the cavity losses, verifying the superradiant scaling laws predicted by the supermode theory. Furthermore these scaling laws are shown to be a direct consequence of the short optical pulse lengths which have been observed.

7.2 Plans for future work

It is proposed to alter the characteristics of the electron beam that pumps the FEL in such a way that FELIX will be able to produce extremely intense single-cycle infrared pulses. The superradiant scaling laws established experimentally (see [1] and chapter 6 of this thesis) indicate that increasing the bunch

charge and reducing the cavity losses will allow the operating parameters to be improved from six cycle optical pulses with an energy of several tens of microjoules towards single cycle pulses with energies of the order of half a millijoule. These pulses would have peak powers of many gigawatts – corresponding to intracavity powers that approach the terawatt level. To achieve this, the cavity losses will have to be reduced by a factor of between 2 and 6, which may easily be done by changing the cavity mirrors to dielectric mirrors optimised for a specific wavelength range or by using metal mirrors with optimised out-coupling holes for different operating wavelengths, and the electron bunch charge will have to be increased by a factor of about 2.5. Since changing the cavity mirrors will affect the operation of the FEL for other users, the initial work will be towards increasing the charge per bunch and it is therefore necessary to develop a diagnostic for bunch length.

More generally, a diagnostic for short (sub picosecond) bunches is necessary for applications where high temporal resolution or high peak electron currents are important. For example, high peak current electron bunches are essential for the success of the next generation of FELs based on self-amplified spontaneous emission (SASE) within one bunch. The principles of SASE have been intensively studied theoretically, and tuneable X-ray lasers are being designed on the basis of SASE. The onset of SASE has recently been observed experimentally at longer infrared wavelengths, which is an important step forward, but progress is hindered because little experimental information is available on the detailed characteristics of the electron bunch length and shape. In addition, the methods used in the electron bunch diagnostic are directly applicable to the measurement of the optical pulses: indeed optical data have already been taken with a resolution better than 100 fs, and the aim is to reach 10 fs resolution.

7.2.1 Proposed method

Although a range of electron bunch diagnostics is available to measure the transverse spatial profile of a relativistic electron beam, few exist for measuring the longitudinal profile. The most common technique is based on spectral measurements of the coherent millimetre-wave transition radiation [2], but such methods suffer from the severe shortcoming of failing to account for low frequency spectral content. The proposed new method is a non-intercepting approach based on the electro-optic sampling of the half-cycle electric field generated by the electron beam when it passes close to a non-linear crystal such as ZnTe. This electric field will be probed via the Pockels effect by observing the polarisation rotation of a Ti:Sapphire laser beam passing through the crystal. The technique is particularly sensitive because (1) the Pockels effect is linear in the applied electric field, (2) the detection can be done in the visible, where excellent detectors and polarisers are available and (3) a configuration is possible in which the *intensity* of the transmitted electro-optic signal varies linearly with electric field. This method has been used elsewhere [3] to probe a half-cycle terahertz field with a naturally synchronised Ti:Sapphire pulse. Some synchronisation is necessary between FELIX and the Ti:Sapphire pulses in our experiment: this has already been achieved to within 400 fs rms [4], and higher resolution will be achieved using the differential optical gating (DOG) technique recently developed in collaboration with Stanford University ([5] and references therein).

7.2.2 Preliminary results

Measurement of the optical micropulse using DOG with resolution better than 100 fs has already been achieved and is reported in [5]. It should be noted that this technique allows the pulse shape to be accurately reconstructed, and features such as the exponential leading edge and the evolution of sub-pulses are clearly evident.
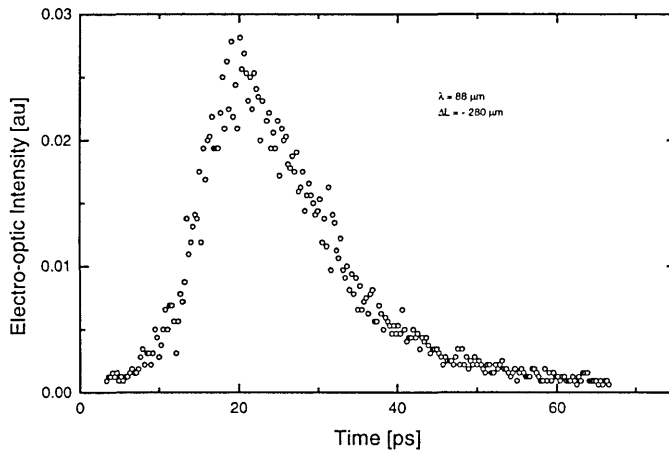

Figure 7.1 *Results obtained using electro-optic detection of the FEL radiation in ZnTe at a wavelength of 88 μm and a cavity desynchronisation of –280 μm. The data show clear evidence of an exponential tail arising from the leading edge of the micropulse losing contact with the electron bunch.*

The electro-optic detection method using a ZnTe crystal has recently been tested and used to characterise the micropulse length and shape of the new long-wavelength FEL-1. Optical pulses of 10-30 cycles in length were measured and shown to be transform limited with a time-bandwidth product of around 0.30. Figure 7.1 shows typical data for the electro-optic probing of 88 μm FEL radiation in ZnTe. The degree of accuracy shown was obtained without the use of DOG: using DOG will increase the resolution from a few 100 fs to 10 fs. Figure 7.2 shows that the time-bandwidth product for data taken at 88 μm is around 0.3.
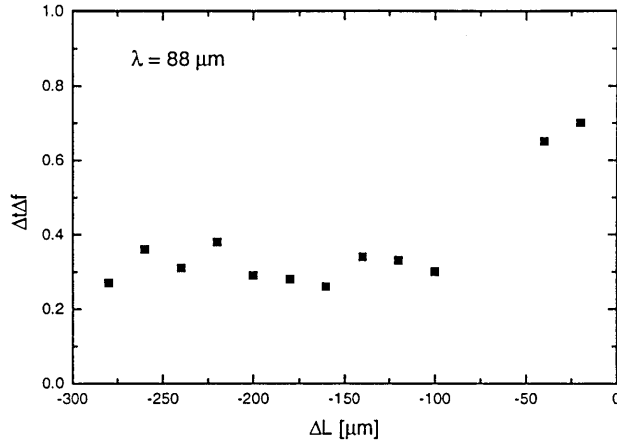
Figure 7.2 *The time-bandwidth product for data taken at* λ *= 88 μm and cavity desynchronisations of up to 280 μm indicating that the pulse is transform limited with a time-bandwidth product of ~ 0.3.*

Furthermore, a configuration has been found that is sensitive to the phase of the electric field of the FEL: Figure 7.3 shows clearly the variation in phase between the FEL electric field and the envelope of the Ti:Sapphire pulse and this phase variation shows the expected changes with cavity desynchronisation. For example, zero phase drift was obtained for $\Delta L = -38$ μm. At other desynchronisations the phase shifts by an amount $2\pi\dfrac{\Delta L'}{\lambda}$, where $\Delta L'$ is the deviation from the desynchronisation corresponding to zero phase drift, in the time taken for one round trip. The observed frequency of the oscillations is therefore expected to be $f = \dfrac{c}{2L_{cav}}\dfrac{\Delta L'}{\lambda}$, giving 5 MHz for the data in Figure 7.3. Although the data have not yet been fully analysed, this technique offers clearly offers exciting possibilities for optical measurements making it possible to investigate inter-pulse phase coherence and wavelength chirps within micropulses.
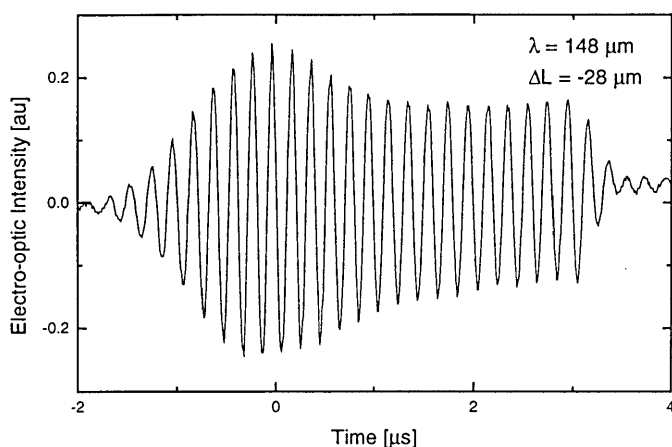
Figure 7.3 *Data illustrating that the electro-optic detection method is sensitive to the phase of the FEL electric field. The phase of the Ti:Sapphire sampling pulse advances relative the FEL micropulse due to the applied cavity desynchronisation. For these data, zero phase drift was obtained for $\Delta L = -38$ μm, so the expected oscillation frequency is 5 MHz.*

These results give confidence that the technique will also work with the desired temporal resolution when the FEL electric field is replaced by the coulomb field of the electron beam.

7.3   References

1.   D. A. Jaroszynski, P. Chaix, N. Piovella D. Oepts, G. M. H. Knippels, A. F. G. van der Meer and H. H. Weits, "Superradiance in a short-pulse free-electron laser", *Phys. Rev. Lett.*, **78**, 1699 (1997).

2.   R. Lai, U. Happek, A.J. Sievers, "Measurements of the longitudinal asymmetry of a charges particle bunch from the coherent synchrotron or transition radiation spectrum", *Phys. Rev. E* **50**, R4294 (1994).

3.   Q. Wu, X. C. Zhang "Free-space electro-optic sampling of mid-infrared pulses", *App. Phys. Lett.*, **71**, 1285-1286 (1997).

4.   G. M. H. Knippels, M. J. van de Pol and A. F. G. van der Meer "Sub-picosecond synchronisation of a 10 fs Ti:Sapphire laser to FELIX", Proceedings of the 20th International free-electron laser conference, Williamsburg, VA. (1998), to be published in *Nucl. Inst. and Meth. in Phys.*

5.   G.M. H. Knippels, A. F. G. van der Meer, M. J. van de Pol, X. Yan, A.M. MacLeod, W. A. Gillespie, C. W. Rella "FEL pulse shape measurements with 100 fs temporal resolution using a 10 fs Ti:Sapphire laser and differential optical gating", Proceedings of the 20th International free-electron laser conference, Williamsburg, VA. (1998) to be published in *Nucl. Inst. and Meth. in Phys.*